Studies on Ion Intercalation/Extraction Reaction at Solid-Liquid Interface and Solid in Prussian Blue Analogs

Yoshifumi Mizuno

Department of Applied Chemistry

Faculty of Science and Engineering

Chuo University

Tokyo, Japan

2013

Contents

Chapter1

Introduction 5

1.1. Background of this research 5

1.1.1. Li-ion batteries for advanced vehicles and grid-scale energy storage 5

1.1.2. Prussian blue analogs as a model electrode for the study on interfacial ion transfer 8

1.2. New functionalities using the electrochemical property of the Prussian blue analogs 12

1.2.1. Electrochemical Mg^{2+} storage in Prussian blue analogs 12

1.2.2. Electrochemical control of the magnetism in Prussian blue analogs 13

Chapter 2

Impedance Spectroscopic Study on Interfacial Ion Transfers in Cyanide-Bridged Coordination Polymer Electrode with Organic Electrolyte 20

2.1. Introduction 20

2.2. Experimental Methods 23

2.3. Results and Discussion 23

2.4. Conclusions 39

Chapter 3

Hydration Effect on Activation Energy for Electrode-Electrolyte Interfacial Charge Transfer 42

3.1. Introduction 42

3.2. Experimental Methods 43

3.3. Results and Discussion 44

3.4. Conclusions 58

Chapter 4

Magnesium Ion Intercalation in Cyanide-Coordinated Porous Polymer 61

4.1. Introduction 61

4.2. Experimental Methods 62

4.3. Results and Discussion 63

4.4. Conclusions 77

Chapter 5

Precise Electrochemical Control of Ferromagnetism in a Cyanide-Bridged Bimetallic Coordination Polymer 80

5.1. Introduction 80

5.2. Experimental Methods 83

5.3. Results and Discussion 83

5.4. Conclusions 100

Chapter 6

Electrospinning-Synthesis of Wire-Structured $LiCoO_2$ for Electrode Materials of High Power Li-Ion Batteries 104

6.1. Introduction 104

6.2. Experimental Methods 105

6.3. Results and Discussion 106

6.4. Conclusions 120

Chapter 7

Conclusions 124

Publication List 127

Acknowledgement..... 129

Chapter 1

Introduction

1.1. Background of this research

1.1.1. Li-ion batteries for advanced vehicles and grid-scale energy storage

Improvement of the efficiency for energy consumption is one of the effective ways to solve the recent energy and environmental problem. In particular, development of advanced vehicles such as hybrid vehicles (HEVs) and electric vehicles (EVs) have strongly been required for the transportation section. In addition, renewable energies such as solar and wind energy have attracted much attention from a viewpoint of diversification of an energy source. Therefore developments of the grid-scale energy storage systems which contribute to the stable supplies of the renewable energies have also been expected. In order to spread these techniques widely, development of high power, high energy, and durable rechargeable batteries are essential.

There are various types of rechargeable batteries such as a lead-acid battery, a nickel-cadmium battery, a Li-ion battery, a nickel hydride battery, and a sodium-sulfur battery, *etc*.[1,2] Among them, a Li-ion battery, which is applied for portable electric devises such as cellar phone and laptop, is promising to application for the advanced vehicles and the grid-scale energy storage systems because it shows high energy density.[3,4]

Li-ion battery consists of a cathode, an anode, and an electrolyte. In case of charge reaction, Li^+ and electron move to the cathode from the anode through the electrolyte, and transforms electrical energy into chemical energy, and stores in it. On the other hand, during discharge reaction, Li^+ and electron move to the anode from the cathode through the electrolyte, and the electrical energy is released. For the present Li-ion battery, transition metal oxides such as $LiCoO_2$,[5] $LiNiO_2$,[6] and $LiMn_2O_4$,[7] and carbon materials[8-10] have been commonly used to the cathode and the anode materials, respectively, and the organic solutions which dissolved Li salts have been commonly used to electrolytes.[11] Figure 1 shows

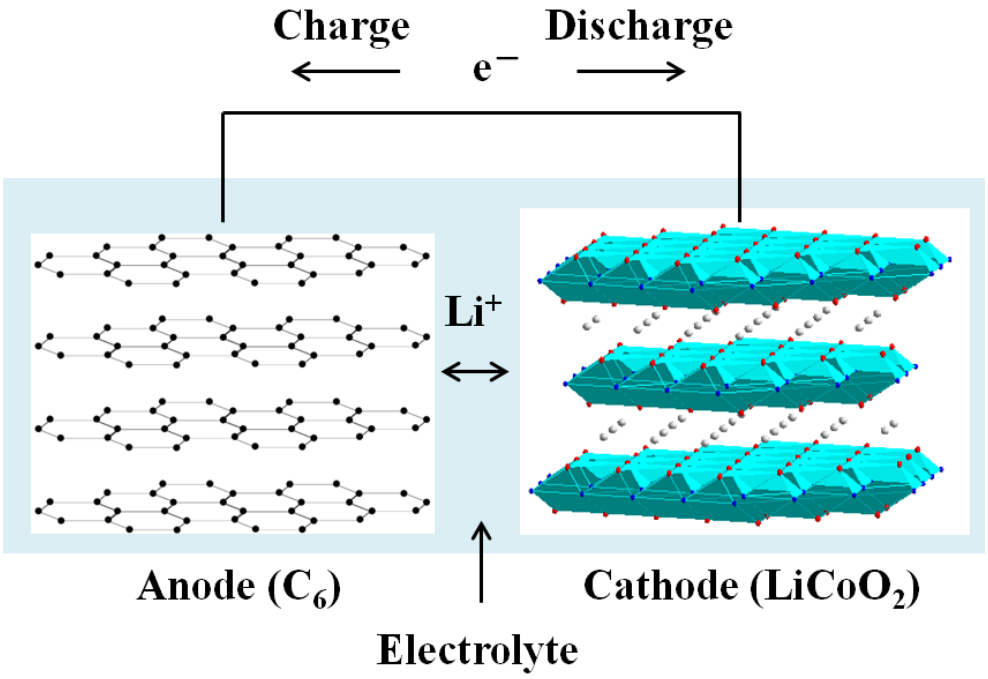

Figure 1. Schematic illustration of Li-ion battery which consists a $LiCoO_2$ as a cathode material and a graphite as an anode material.

the schematic illustration of Li-ion battery which consists a $LiCoO_2$ as a cathode and a graphite as an anode. Electrochemical ion insertion/extraction reactions in these materials during charge-discharge are

$$Li_{1-x}CoO_2 + xLi^+ + xe^- \leftrightarrow LiCoO_2, \text{ and}$$

$$Li_xC_6 \leftrightarrow C_6 + xLi^+ + xe^-.$$

There are various problems in Li-ion battery which should be solved to application to the advanced vehicles and the grid-scale energy storage system. The following are mentioned as problems.

1) Enhancement the energy density (enhancement the charge-discharge capacity).
2) Achievement of a higher power (Achievement of a faster charge-discharge reaction).
3) Reduction of cost.
4) Improvement of durability.

In particular, 1) and 2) are essential for application to the advanced vehicles. In order to achieve the higher charge-discharge capacity, it is essential to develop new families of electrode materials. For examples, elemental sulfur and sulfide materials have widely been investigated because they show very high theoretical capacity (1675 mAh/g, $S_8 + 16Li^+ + 16e^- \rightarrow 8Li_2S$).[12-14] It is essential to achieve the faster charge-discharge reaction in order to achieve a higher power. Using the nanostructured electrode materials is one of the effective ways to achieve the fast Li^+ transfer, because they possess the larger surface area and shorter Li^+ diffusion length.[15,16]

In addition, it is also important to analyze each charge transfer process for faster charge-discharge reaction. Generally speaking, there are three charge transfer processes when the Li-ion batteries are charged/discharged; Li^+ diffusion through the electrolyte solution, Li^+ transfer at the electrode-electrolyte interface and Li-ion diffusion within the electrode material. Among them, Li^+ transfer at the electrode-electrolyte interface has not been understood well, compared to the Li^+

diffusion in the electrolyte or electrode. Therefore, analysis of the interfacial charge transfer for various electrodes, ions or electrolytes is of particular importance for further comprehension.

According to the previous reports,[17,18] the Li^+ transfer at the electrode-electrolyte interface can be divided into two processes. One is the Li^+ transfer between the Outer Helmholtz Plane (OHP) and Inner Helmholtz Plane (IHP), including the solvation/desolvation process. The other is the Li^+ transfer between the IHP and electrode, including the ad-ion diffusion on the electrode surface. To observe two processes separately, electrochemical impedance spectroscopy (EIS) is a powerful technique. The Nyquist plot obtained by the EIS shows two semi-circle components corresponding to RC circuits (the interfacial charge transfer resistance in parallel with the interfacial double layer capacitance) between the OHP and IHP, and between the IHP and electrode, respectively.[19,20] Furthermore, by varying temperature, the temperature dependence of each resistance can provide the activation energy for each process, which sheds light on the microscopic understanding of the interfacial charge transfer.

On the other hand, 3) and 4) are necessary for application to the grid-scale energy storage system. The cost reduction is the most serious problem in a Li-ion battery because Li metal is expensive. Therefore, post Li-ion batteries which do not contain Li metal have been required.

1.1.2. Prussian blue analogs as a model electrode for the study on interfacial ion transfer

Prussian blue analogs (PBAs) are promising candidates for the new families of electrode materials because PBAs ($A_xM[M'(CN)_6]_{1-y}\cdot\square_y\cdot nH_2O$, A; alkali metal, M, M'; transition metal, □; $[M'(CN)_6]$ vacancy, hereafter denoted MM'-PBA) possess both the redox active sites and the mixed conductivity within the cyanide-bridged porous structure. Therefore, PBAs can intercalated various ions, such as Li^+, Na^+, K^+, and NH_4^+, in both organic[21-25] and aqueous electrolytes[26-31] by electrochemical methods (Figure 2).

The first application of PBAs for the electrode materials of Li-ion battery was reported by N. Imanishi *et al.*[21] FeFe-PBA showed the reversible charge-discharge capacity of 110 mAh/g at first charge-discharge cycle, while 30 % of the capacity faded after 10 charge-discharge cycles. The

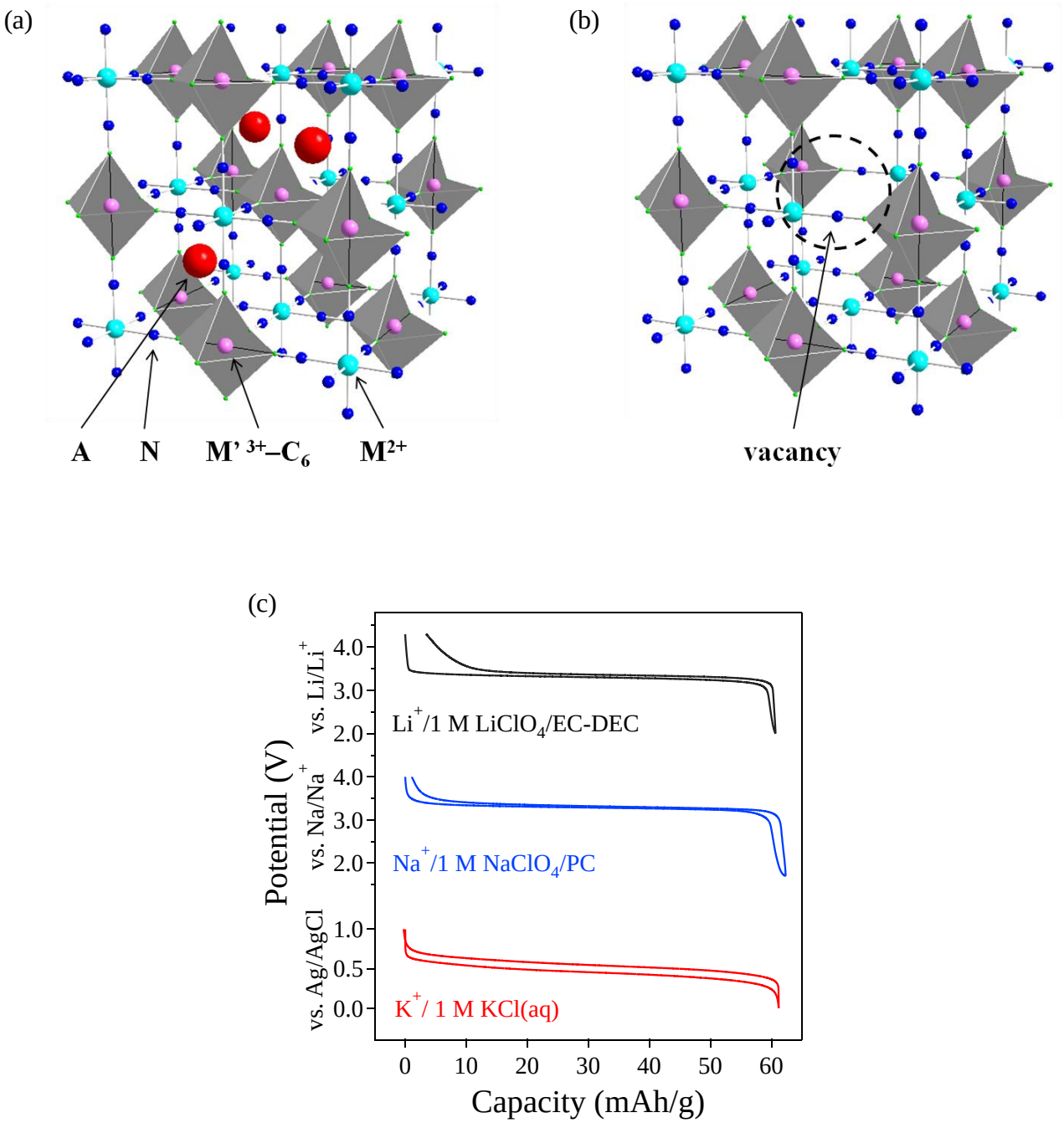

Figure 2. Crystalline structure of PBA (a) $AM[M'(CN)_6]$, and (b) $A_xM[M'(CN)_6]_{1-y}\cdot\square_y\cdot nH_2O$. (c) Charge-discharge curves of NiFe-PBA during various ion intercalation/extraction.

electrode performances of MFe-PBA (M = V, Mn, Co, Ni, and Cu) were also reported by same group, and the largest charge-discharge capacity was shown in CuFe-PBA (140 mAh/g at the first cycle). However, the cyclabilities of these PBAs were not declared.[32]

Recently, M. Okubo *et al*. reported that MnFe-PBA has robust structure for Li^+ intercalation/extraction and showed the excellent cyclability, although the charge-discharge capacity was lower (60 mAh/g) than those for conventional electrode materials.[22]

In order to enhance the charge-discharge capacity of PBAs, it is essential to eliminate the vacancies in PBAs (□). D. Asakura *et al*. focused on $K_2Mn_2(CN)_6$, which has few vacancies, and achieved the high charge-discharge capacity of 200 mAh/g after electrochemical K^+ extraction, while the cyclability was not good. However, the initial charge-discharge capacity of the PBA is comparable to those for transition metal oxides.[25]

Very recently, C. D. Wessells *et al.* reported application of PBAs to the electrode materials in the aqueous batterie, which pronounces the long cycle life, high power, good energy efficiency, safety and low cost of the aqueous batteries with the PBA electrodes.[28-31] For example, NiFe-PBA allowed 66 % retention of the initial capacity at an extremely high (41.7 C) rate with Na^+ aqueous electrolyte. The high-rate capability with aqueous electrolyte was much better than that with organic electrolyte.

The easy accessibility of various ions into PBAs provides a good model of the electrode-electrolyte interface. In chapter 2, the EIS study on the Li^+ transfer at the MnFe-PBA electrode-electrolyte interface was investigated. Furthermore, the Na^+ transfer at the MnFe-PBA electrode-electrolyte interface is also reported in comparison with the case of Li^+.

The composite electrode, which contains PBA, acetylene black (AB) as conducting additive, and poly(tetrafluoroethylene) as binder, was used for analysis of interfacial charge transfer described in chapter 2. However, there exist many interfaces in the composite electrode except PBA-electrolyte interface, such as current collector-AB, PBA-AB and PBA-PBA interfaces. Therefore, a thin film electrode of NiFe-PBA was employed for the EIS study in chapter 3, to avoid the complexities caused by various coexisting interfaces in the composite electrode. In chapter 3, the EIS study on the interfacial

Li^+ and Na^+ transfers with both organic and aqueous electrolyte was investigated. Furthermore, interfacial Mg^{2+} transfer is also reported.

1.1.3. Related work; nanostructured $LiCoO_2$ for high-power Li-ion batteries

As described above, using the nanostructured cathode materials is one of the effective ways for achieving the fast Li^+ transfer, because they possess the larger surface area and shorter Li^+ diffusion length. [3,33-39]

To obtain the nanostructured cathode materials, various techniques such as a post-templating method,[40] sol-gel methods,[41,42] a spray-drying method,[43] a coprecipitation method[44] and hydrothermal methods,[34-37,45-48] have been reported to date. For examples, sol-gel methods enable us to obtain various nano-sized materials from the precursor solutions containing various metal salts. The main advantage of this method is that the chemical composition could be controlled more easily and precisely than the solid-state sintering method due to the homogeneous mixing of the solutes in the liquid-phase. However, when the heat treatment is conducted at high temperature for a long duration, the particle size generally becomes large due to the crystal growth. In contrast, the wire-structure could suppress the crystal growth even under the heating condition at high temperature due to the nonwoven fabric morphology.[37] Thus we have fabricated the highly crystalline wire-structured electrode materials by the heat treatment of the wire-structured precursors, and succeeded in achieving the higher charge/discharge rate-capability. However, the hydrothermal method used for the synthesis of the wire-structured precursors in the previous studies is not scalable for the mass production from the viewpoint of the practical application. Therefore, another process for the fabrication of the wire-structured electrode materials has been strongly desired.

Chapter 6 described electrospinning-synthesis of the wire-structured materials. The electrospinning method has attracted much attention recently, since this method can easily fabricate the wire-structure only by applying the high-voltage to the precursor solution. By using this method, various wire-structured metal carbon composites, and electrode materials like $LiFePO_4$, have been synthesized

successfully.[38,49-51] It should be emphasized that the electrospinning method is highly scalable, which could be applied for the mass production process. As the electrode material for Li-ion batteries, $LiCoO_2$ was used in this study. $LiCoO_2$ is one of the commercially used cathode materials with the high energy density and excellent cyclability,[52] thus the fabrication of nanostructured $LiCoO_2$ by the scalable technique like the electrospinning method is of particular importance.

In chapter 6, the fabrication of wire-structured $LiCoO_2$ via the electrospinning method was investigated and clarified the electrode properties of wire-structured $LiCoO_2$.

1.2. New functionalities using the electrochemical property of the Prussian blue analogs

As described above, PBAs show unique electrochemical ion storage properties due to their cyanide-bridged porous structures, and these properties can offer us a good model of the study on the interfacial ion transfer. In chapter 4 and 5, the two new functionalities on PBAs by focusing on their electrochemical ion storage properties were reported.

1.2.1. Electrochemical Mg^{2+} storage in Prussian blue analogs

From a viewpoint of cost, post Li-ion batteries which do not contain Li metal have been required as described in 1.1.1. In particular, a Mg-ion battery has attracted much attention.[53] The Mg-ion battery is one of the promising post Li-ion batteries because Mg metal is inexpensive and has large reserve. Furthermore, Mg-ion battery can show potentially high charge-discharge capacity and high energy density because Mg^{2+} is a divalent cation. However, there are few electrode materials which can intercalate Mg^{2+}[54,55] because the Coulombic repulsion between Mg^{2+} and host material too large to intercalate.[56] In addition, Mg metal is potentially passivated in various polar organic electrolytes, which are commonly used for electrolytes of Li- and Na-ion batteries.[57] D. Aurbach *et al*. reported the best systems of Mg-ion battery, which consist of Chevrel compounds ($Mg_xMo_6T_8$ (T = S, Se)) as cathode materials,[58-60] THF solutions of Mg organohaloaluminate salts as electrolytes,[61-63] and Mg metal as anode, and these systems show excellent cyclabilities. However, new families of electrode material for Mg-ion batteries have been required because Mo in the Chevrel compounds is expensive, and the

charge-discharge potential of these compounds are very low (1.2 V (vs. Mg/Mg^{2+})). Furthermore, THF solutions of Mg organohaloaluminate salts are very dangerous to handle. Therefore, the new systems which are safe and inexpensive have been investigated.

In order to achieve Mg^{2+} intercalation, using aqueous electrolyte would be effective way because ion inserts into the host with hydrated state. Therefore, the hydrated shell around ion suppresses the large Coulombic repulsion, and enables Mg^{2+} insertion/extraction. EIS study described in chapter 3 provided the possibility of Mg^{2+} intercalation in PBA.

Chapter 4 described the detailed studies on Mg^{2+} intercalation in CuFe-PBA with aqueous electrolyte.

1.2.2. Electrochemical control of the magnetism in Prussian blue analogs

Multifunctionality is an important concept in recent chemistry, because existence of multiple functionalities in a single phase can produce novel cooperative phenomena such as multiferroics.[64] In particular, coordination polymers possess potentially controllable electronic and structural properties; thus, they could provide a rational strategy achieving the novel multifunctionalities.[65] For example, the magnetic coordination polymers have been reported to show a wide variety of magnetic properties (*e.g.*, room temperature ferrimagnetism,[66] spin-crossover,[67,68] Haldane gap[69]). In addition, other functionalities can also be introduced by designing the structure and electronic state. The coexistence of magnetism with another functionality frequently results in magnetism controllable by the external stimuli (*e.g.*, photo-irradiation,[70-73] guest insertion,[74,75] and electric field application[76]), which can be applied to electronic switch devices. Therefore, controllable magnetism of coordination polymers has been investigated intensively.

PBA is one of the best studied magnetic coordination polymers.[77] The cyanide-bridged perovskite-type structure of PBA possesses intriguing magnetism due to the strong σ and π donation/back-donation ability of the bridging cyanide ligand. Furthermore, the open porous structure of PBA permits the penetration of small guests, which could realize H_2 adsorption,[78] proton

conduction,[79] ion exchange,[80] and ion storage.[21-32]

Recently, the coexistence of magnetism and ion storage ability in PBA has been focused, and magnetism switching was achieved by electrochemical ion insertion/extraction. Bimetallic CuFe-PBA was switched reversibly between a ferromagnet and a paramagnet by galvanostatic solid state redox of the paramagnetic Fe^{3+}/diamagnetic Fe^{2+} couple.[23] Sato *et al*. also reported the electrochemical modification of magnetism of CrCr-,[81] FeFe-,[82] and NiFe-PBAs using a potentiostatic method.[83] However, these previous studies did not achieve precise control of the magnetism due to the difficulty in the quantitative ion/electron titration. To manipulate the electronic state and magnetism of PBA more quantitatively, an advanced electrochemical titration technique is required.

Chapter 5 described the precise electrochemical control of ferromagnetism of a bimetallic NiFe-PBA through use of a quantitative Li^+ titration technique, i.e., the galvanostatic intermittent titration technique (GITT).

References

(1-1) Dunn, B.; Kamath, H.; Tarascon, J. M. *Science* **2011**, *334*, 928-935.

(1-2) Yang, Z.; Zhang, J.; Kintner-Meyer, M. C. W.; Lu, X.; Choi, D.; Lemmon, J. P.; Liu, J. *Chem. Rev*. **2011**, *111*, 3577-3613.

(1-3) Tarascon, J. M.; Armand, M. *Nature* **2001**, *414*, 359-367.

(1-4) Armand, M.; Tarascon, J. M. *Nature* **2008**, *451*, 652-657.

(1-5) Mizushima, K.; Jones, P. C.; Wiseman, P. J.; Goodenough, J. B. *Mat. Res. Bull.* **1980**, *15*, 783-789.

(1-6) Dahn, J. R.; van Sacken, U.; Juzkow, M. W.; Al-Janaby, H. *J. Electrochem. Soc.* **1991**, *138*, 2207-2211.

(1-7) Thackaeray, M. M.; David, W. I. F.; Bruce, P. G.; Goodenough, J. B. *Mat. Res. Bull.* **1983**, *18*, 461-472.

(1-8) Aurbach, D.; Markovsky, B.; Weissman, I.; Levi, E.; Ein-Eli, Y. *Electrochim. Acta*, **1999**, *45*, 67-86.

(1-9) Frackowiak, E.; Béguin, F. *Carbon*, **2002**, *40*, 1775-1787.

(1-10) Yoo, E.; Kim, J. D.; Hosono, E.; Zhou, H. S.; Kudo, T.; Honma, I. *Nano Lett.* **2008**, *8*, 2277-2282.

(1-11) Xu, K. *Chem. Rev*. **2004**, *104*, 4303-4417.

(1-12) Wang, J.; Yang, J.; Wan, C.; Du, K.; Xie, J.; Xu, N. *Adv. Funct. Mater.* **2003**, *13*, 487-492.

(1-13) Ji, X.; Lee, K. T.; Nazar, L. F. *Nat. Mater.* **2009**, *8*, 500-506.

(1-14) Bruce, P. G.; Freunberger, S. A.; Hardwick, L. J.; Tarascon, J. M. *Nat. Mater.* **2012**, *11*, 19-29.

(1-15) Bruce, P. G.; Scrosati, B.; Tarascon, J. M. *Angew. Chem. Int. Ed*. **2008**, *47*, 2930-2946.

(1-16) Guo, Y.-G.; Hu, J.-S.; Wan, L.-J. *Adv. Mater*. **2008**, *20*, 2878-2887.

(1-17) Bruce, P. G.; Saidi, M. Y. *J. Electroanal. Chem.* **1992**, *322*, 93-105.

(1-18) Bruce, P. G.; Saidi, M. Y. *Solid State Ion*. **1992**, *51*, 187-190.

(1-19) Nakayama, M.; Ikuta, H.; Uchimoto, Y.; Wakihara, M. *J. Phys. Chem. B* **2003**, *107*,

10603-10607.

(1-20) Kobayashi, S.; Uchimoto, Y. *J. Phys. Chem. B*, **2005**, *109*, 13322-13326.

(1-21) Imanishi, N.; Morikawa, T.; Kondo, J.; Takeda, Y.; Yamamoto, O.; Kinugasa, N.; Yamagishi, T. *J. Power Sources* **1999**, *79*, 215-219.

(1-22) Okubo, M.; Asakura, D.; Mizuno, Y.; Kim, J.-D.; Mizokawa, T.; Kudo, T.; Honma, I.; *J. Phys. Chem. Lett.* **2010**, *1*, 2063-2071.

(1-23) Okubo, M.; Asakura, D.; Mizuno, Y.; Kudo, T.; Zhou, H.; Okazawa, A.; Kojima, N.; Ikedo, K.; Mizokawa, T.; Honma, I. *Angew. Chem. Int. Ed*. **2011**, *50*, 6269-6274.

(1-24) Mizuno, Y.; Okubo, M.; Asakura, D.; Saito, T.; Hosono, E.; Saito, Y.; Oh-ishi, K.; Kudo, T.; Zhou, H. *Electrochim. Acta* **2012**, *63*, 139-145.

(1-25) Asakura, D.; Okubo, M.; Mizuno, Y.; Kudo, T.; Zhou, H.; Ikedo, K.; Mizokawa, T.; Okazawa, A.; Kojima, N. *J. Phys. Chem. C* **2012**, *116*, 8364-8369.

(1-26) Itaya, K.; Ataka, T.; Toshima, S. *J. Am. Chem. Soc*. **1982**, *104*, 4767-4772.

(1-27) Itaya, K.; Uchida, I.; Neef, V. D. *Acc. Chem. Res.* **1986**, *19*, 162-168.

(1-28) Wessells, C. D.; Huggins, R. A.; Cui, Y. *Nat. Commun*. **2011**, *2*, 550.

(1-29) Wessells, C. D.; Peddada, S. V.; Huggins, R. A.; Cui, Y. *Nano Lett.* **2011**, *11*, 5421-5425.

(1-30) Wessells, C. D.; Peddada, S. V.; McDowell, M. T.; Huggins, R. A.; Cui, Y. *J. Electrochem. Soc.* **2012**, *159*, A98-A103.

(1-31) Wessells, C. D.; McDowell, M. T.; Peddada, S. V.; Pasta, M.; Huggins, R. A.; Cui, Y. *ACSnano* **2012**, *6*, 1688-1694.

(1-32) Imanishi N.; Morikawa T.; Kondo J.; Yamane R.; Takeda Y.; Yamamoto O.; Sakaebe H.; Tabuchi M.; *J. Power Sources* **1999**, *81-82*, 530-534.

(1-33) Wang, Y.; Cao, G. *Adv. Mater*. **2008**, *20*, 2251-2269.

(1-34) Okubo, M.; Hosono, E.; Kim, J.-D.; Enomoto, M.; Kojima, N.; Kudo, T.; Zhou, H.; Honma, I. *J. Am. Chem. Soc*. **2007**, *123*, 7444-7452.

(1-35) Okubo, M.; Mizuno, Y.; Yamada, H.; Kim, J.-D.; Hosono, E.; Zhou, H.; Kudo, T.; Honma, I.

ACSnano **2010**, *4*, 741-752.

(1-36) Okubo, M.; Kim, J.; Kudo, T.; Zhou H.; Honma, I. *J. Phys Chem. C* **2009**, *113*, 15337-15342.

(1-37) Hosono, E.; Kudo, T.; Honma, I.; Matsuda, H.; Zhou, H. *Nano Lett*. **2009**, *9*, 1045-1051.

(1-38) Hosono, E.; Wang, Y.; Kida, N.; Enomoto, M.; Kojima, N.; Okubo, M.; Matsuda, H.; Saito, Y.; Kudo, T.; Honma, I.; *et al*. *ACS Appl. Mater. Interfaces* **2010**, *1*, 212-218.

(1-39) Hu, Y.-S.; Kienle, L.; Guo, Y. G.; Maier, J. *Adv. Mater*. **2006**, *18*, 1421-1426.

(1-40) Jiao, F.; Shaju, K. M.; Bruce, P. G. *Angew. Chem. Int. Ed*. **2005**, *44*, 6550-6553.

(1-41) Peng, Z. S.; Wan, C. R.; Jiang, C. Y. *J. Power Sources* **1998**, *72*, 215-220.

(1-42) Yoon, W. S.; Kim, K. B. *J. Power Sources* **1999**, *81-82*, 517-523.

(1-43) Li, Y.; Wan, C.; Wu, Y.; Jiang, C.; Zhu, Y. *J. Power Sources* **2000**, *85*, 294-298.

(1-44) Chen, H.; Qiu, X.; Zhu, W.; Hagenmuller, P. *Electrochem. Commun*. **2002**, *4*, 488-491.

(1-45) Larcher, D.; Palacin, M. R.; Amatucci, G. G.; Tarascon, J. M. *J. Electrochem. Soc*. **1997**, *144*, 408-417.

(1-46) Tabuchi, M.; Ado, K.; Kobayashi, H.; Sakaebe, H.; Kageyama, H.; Masquelier, C.; Yoneyama, M.; Hirano, A.; Kanno, R. *J. Mater. Chem*. **1999**, *9*, 199-204.

(1-47) Kobayashi, H.; Shigemura, H.; Tabuchi, M.; Sakaebe, H.; Ado, K.; Kageyama, H.; Hirano, A.; Kanno, R.; Wakita, M.; Morimoto, S.; *et al*. *J. Electrochem. Soc*. **2000**, *147*, 960-969.

(1-48) Burukhin, A.; Brylev, O.; Hany, P.; Churagulov, B. R. *Solid State Ionics* **2002**, *151*, 259-263.

(1-49) Gu, Y.; Chen, D.; Jiao, X. *J. Phys. Chem. B* **2005**, *109*, 17901-17906.

(1-50) Sell, S. A.; Bowlin, G. L. *J. Mater. Chem.* **2008**, *18*, 260-263.

(1-51) Dong, Z.; Kennedy, S. J.; Wu, Y. *J. Power Sources* **2011**, *196*, 4886-4904.

(1-52) Mizushima, K.; Jones, P. C.; Wiseman, P. J.; Goodenough, J. B. *Mat. Res. Bull.* **1980**, *15*, 783-789.

(1-53) Novák, P.; Imhof, R.; Haas, O. *Electrochim. Acta* **1999**, *45*, 351-367.

(1-54) Tao, Z.-L.; Xu, L.-N.; Gou, X.-L.; Chen, J.; Yuan, H.-T. *Chem. Commun.* **2004**, 2080-2081.

(1-55) Imamura, D.; Miyayama, M.; Hibino, M.; Kudo, T. *J. Electrochem. Soc*. **2003**, *150*,

A753-A758.

(1-56) Levi, E.; Gofer, Y.; Aurbach, D. *Chem. Mater.* **2010**, *22*, 860-868.

(1-57) Lu, Z.; Schechter, A.; Moshkovich, M.; Aurbach, D. *J. Electroanal. Chem.* **1999**, *466*, 203-217.

(1-58) Aurbach, D.; Lu, Z.; Schechter, A.; Gofer, H.; Turgeman, R.; Cohen, Y.; Moshkovich, M.; Levi, E. *Nature* **2000**, *407*, 724-727.

(1-59) Levi, E.; Lancry, E.; Mitelman, A.; Aurbach, D.; Ceder, G.; Morgan, D.; Isnard, O. *Chem. Mater.* **2006**, *18*, 5492-5503.

(1-60) Suresh, G. S.; Levi, M. D.; Aurbach, D. *Electrochim. Acta* **2008**, *53*, 3889-3896.

(1-61) Aurbach, D.; Moshkovich, M.; Schechter, A.; Turgeman, R. *Electrochem. Solid State Letters* **2000**, *3*, 31-34.

(1-62) Aurbach, D.; Schechter, A.; Moshkovich, M.; Cohen, Y. *J. Electrochem. Soc.* **2001**, *148*, A1004-A1014.

(1-63) Mizrahi, O.; Amir, N.; Pollak, E.; Chusid, O.; Marks, V.; Gottlieb, H.; Larush, L.; Zinigrad, E.; Aurbach, D. *J. Electrochem. Soc*. **2008**, *155*, A103-A109.

(1-64) Hwang, H.Y.; Iwasa, Y.; Kawasaki, M.; Keimer, B.; Nagaosa, N.; Tokura, Y. *Nat. Mater.* **2012**, *11*, 103-113.

(1-65) Zhou, H.-C.; Long, J. R.; Yaghi, O. M. *Chem. Rev.* **2012**, *112*, 673-674.

(1-66) Ferlay, S.; Mallah, T.; Ouahes, R.; Veillet, P.; Verdaguer, M. *Nature* **1995**, *378*, 701-703.

(1-67) Kondo, A.; Kajiro, H.; Noguchi, H.; Carlucci, L.; Proserpio. D. M.; Ciami, G.; Kato, K.; Taketa, M.; Seki, H.; Sakamoto, M.; Hattori, Y.; Okino, F.; Maeda, K.; Ohba, T.; Kaneko, K.; Kanoh, H. *J. Am. Chem. Soc*. **2011**, *133*, 10512-10522.

(1-68) Bhar, K.; Khan, S.; Costa, J. S.; Ribas, J.; Roubeau, O.; Mitra, P.; Ghosh, B. K. *Angew. Chem. Int. Ed*. **2012**, *51*, 2142-2145.

(1-69) Renard, J. P.; Verdaguer, M.; Regnault, L. P.; Erkelens, W. A. C.; Rossatmignod, J.; Ribas, J.; Stirling, W. G.; Vettier, C. *J. Appl. Phys*. **1988**, *63*, 3538-3541.

(1-70) Sato, O.; Iyoda, T.; Fujishima, A.; Hashimoto, K. *Science* **1996**, *272*, 704-706.

(1-71) Neville, S. M.; Halder, G. J.; Chapman, K. W.; Duriska, M. B.; Southon, P. D.; Cashion, J. D.; Létard, J.-F.; Moubaraki, B.; Murray, K. S.; Kepert, C. J. *J. Am. Chem. Soc.* **2008**, *130*, 2869-2876.

(1-72) Kida, N.; Hikita, M.; Kashima, I.; Okubo, M.; Itoi, M.; Enomoto, M.; Kato, K.; Takara, M.; Kojima, N. *J. Am. Chem. Soc.* **2009**. *131*, 212-220.

(1-73) Ohkoshi, S.; Imoto, K.; Tsunobuchi, Y.; Takano, S.; Tokoro, H. *Nat. Chem*. **2011**, *3*, 564-569.

(1-74) Agustí, G.; Ohtani, R.; Yoneda, K.; Gaspar, A. B.; Ohba, M.; Sánchez-Royo, J. F.; Muñoz, M. C.; Kitagawa, S.; Real, J. A. *Angew. Chem. Int. Ed*. **2009**, *48*, 8944-8947.

(1-75) Ohtani, R.; Yoneda, K.; Furukawa, S.; Horike, N.; Kitagawa, S.; Gasper, A. B.; Muñoz, M. C.; Real, J. A.; Ohba, M. *J. Am. Chem. Soc.* **2011**. *138*, 8600-8605.

(1-76) Mahfoud, T.; Molnár, G.; Bonhommeau, S.; Cobo, S.; Salmon, L.; Demont, P.; Tokoro, H.; Ohkoshi, S.; Boukheddaden, K.; Bousseksou, A. *J. Am. Chem. Soc.* **2009**, *131*, 15049-15054.

(1-77) Miller, J. S.; Drillon, M.; *Molecules to Materials V Ed.*, Wiley-VCH Verlag GmbH & Co. **2005**.

(1-78) Kaye, S. S.; Long, J. R. *J. Am. Chem. Soc.* **2005**, *127*, 6506-6507.

(1-79) Ohkoshi, S.; Nakagawa, K.; Tomono, K.; Imoto, K.; Tsunobuchi, Y.; Tokoro, H. *J. Am. Chem. Soc*. **2010**, *132*, 6620-6621.

(1-80) Matsuda, T.; Kim, J.; Moritomo, Y. *J. Am. Chem. Soc*. **2010**, *132*, 12206-12207.

(1-81) Sato, O.; Iyoda, T.; Fujishima, A.; Hashimoto, K. *Science* **1996**, *271*, 49-51.

(1-82) Sato, O.; Hayami, S.; Einaga, Y.; Gu, Z.-Z. *Bull. Chem. Soc. Jpn*. **2003**, *76*, 443-470.

(1-83) Sato, O. *J. Solid State Electrochem.* **2007**, *11*, 773-779.

Chapter 2

Impedance Spectroscopic Study on Interfacial Ion Transfers in Cyanide-Bridged Coordination Polymer Electrode with Organic Electrolyte

2.1. Introduction

Higher power Li-ion batteries have attracted much attention for their use in advanced transportation systems, such as hybrid electric vehicles (HEVs) and electric vehicles (EVs), thus faster Li^+ transfer in the battery is essentially required.[1-4]

In order to achieve the faster charge transfer, it is important to analyze each charge transfer process. Generally speaking, there are three charge transfer processes when the Li-ion batteries are charged/discharged; Li^+ diffusion through the electrolyte solution, Li^+ transfer at the electrode-electrolyte interface and Li^+ diffusion within the electrode material. Among them, Li^+ transfer at the electrode-electrolyte interface has not been understood well, compared to the Li^+ diffusion in the electrolyte or electrode. Therefore, analysis of the interfacial charge transfer for various electrodes, ions or electrolytes is of particular importance for further comprehension.

Prussian blue analogues (PBAs) are promising candidates for the electrode materials.[5-7] PBAs have a cyanide-bridged perovskite-type framework with a generalized formula of $A_xM[M'(CN)_6]_{1-y}\cdot\square_y\cdot nH_2O$ (A: Alkali metal, M, M': transition metal), in which □ denotes the $[M'(CN)_6]$ vacancy. The electrochemical ion insertion/extraction in PBAs has been investigated intensively for decades, and PBAs have been revealed to accommodate various ions such as Li^+, Na^+, K^+ and NH_4^+.[8-10] In particular, PBA with M = Mn and M' = Fe (hereafter called MnFe-PBA) showed the highly stable Li^+ insertion/extraction reaction. The easy accessibility of various ions into PBAs offers us a good model of the electrode-electrolyte interface, because the contribution from the respective interfacial components can be evaluated by changing the ion and electrolyte. However, detailed analysis of the interfacial charge transfer between the PBA electrode and electrolyte has not been carried out to data.

Scheme 1 shows the schematic illustration of the Li^+ transfer at the PBA electrode-electrolyte interface. According to the previous reports,[11,12] the Li^+ transfer at the electrode-electrolyte interface can be divided into two processes. One is the Li^+ transfer between the Outer Helmholtz Plane (OHP) and Inner Helmholtz Plane (IHP), including the solvation/desolvation process. The other is the Li^+ transfer between the IHP and electrode, including the ad-ion diffusion on the electrode surface. To observe two processes separately, electrochemical impedance spectroscopy (EIS) is a powerful technique. The Nyquist plot obtained by the EIS shows two semi-circle components corresponding to RC circuits (the interfacial charge transfer resistance in parallel with the interfacial double layer capacitance) between the OHP and IHP, and between the IHP and electrode, respectively.[13,14] Furthermore, by varying temperature, the temperature dependence of each resistance can provide the activation energy for each process, which sheds light on the microscopic understanding of the interfacial charge transfer.

Here, the EIS study on the Li^+ transfer at the MnFe-PBA electrode-electrolyte interface was reported. Furthermore, the Na^+ transfer at the MnFe-PBA electrode-electrolyte interface is also reported in comparison with the case of Li^+.

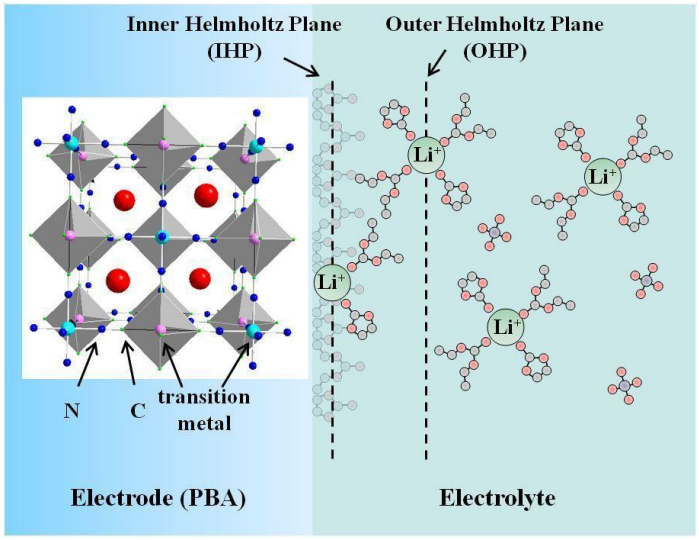

Scheme 1. Schematic illustration of the Li^+ transfer at the PBA electrode-electrolyte interface.

2.2. Experimental Methods

MnFe-PBA was prepared by a precipitation method. An aqueous solution of 0.15 M $MnCl_2 \cdot 4H_2O$ was added dropwise to an aqueous solution of 0.1 M $K_3Fe(CN)_6$. The composition was determined by the standard micro-analytical method for C, H and N elements. Calcd. for $K_{0.1}Mn[Fe(CN)_6]_{0.7} \cdot 3.6H_2O$: C, 18.54; H, 2.67; and N, 21.62. Found: C, 18.43; H, 2.56; and N, 21.19.

Powder X-ray diffraction (XRD) measurement was carried out on a Bruker D8 Advance using Cu $K\alpha$ radiation in steps of 0.01˚ over the 2θ range of 5 – 80˚. The unit cell parameters were calculated by the least square fitting with peak top values. SEM measurement was carried out on a LEO GEMINISUPRA 35.

For the electrochemical measurements, three electrode glass cells were used. MnFe-PBA was ground with 20 wt % acetylene black and 5 wt % poly(tetrafluoroethylene) into a paste and used as working electrode. For the counter and reference electrode, Li or Na metal was used. For the electrolyte, 1 M $LiClO_4$/ethylene carbonate-diethyl carbonate (EC-DEC, 1:1 V/V %), 1 M $LiClO_4$/propylene carbonate (PC) (Lithium battery grade, Kishida Chemical) or 1 M $NaClO_4$/PC (Magnesium battery grade, Kishida Chemical) was used. For the alkali-ion insertion/extraction, a galvanostat (SD-8, Hokuto Denko) was used, and the cut-off voltages were 2.0 V and 4.3 V (vs. Li/Li^+) for Li^+ insertion/extraction, and 1.7 V and 4.0 V (vs. Na/Na^+). The open-circuit voltages (OCVs) were measured by repeats of flowing galvanostatic current (current density; 18 mA/g) for 10 minutes and the potential relaxation for 30 minutes under an open-circuit state. The electrochemical impedance spectra were recorded with a frequency response analyzer (SI 1250, Solatron) at the frequency ranging from 5 mHz to 50 kHz with an amplitude of 10 mV.

2.3. Results and Discussion

The PBA electrode material, MnFe-PBA, was synthesized by a precipitation method. The powder XRD pattern showed formation of a cubic PBA framework (a = 10.4996 Å, V = 1157.4 $Å^3$) without impurity (Figure 1). The calculated unit cell parameters are consistent to the previously reported values

(a = 10.489 Å, V = 1154.1 Å^3).[5,9] SEM images showed a mean particle size of about 1.8 μm (inset in Figure 1).

Before starting the EIS analysis, the open-circuit voltage (OCV) was measured as a function of the amount of alkali-ion in MnFe-PBA. Figure 2(a) shows the OCVs during the Li^+ insertion/extraction using 1 M $LiClO_4$/PC, and during Na^+ insertion/extraction using 1 M $NaClO_4$/PC. The electrochemical reaction is described as,

$$xA^+ + xe^- + \text{MnFe-PBA} \Leftrightarrow A_x\text{MnFe-PBA (A = Li, Na)}.$$

As for Li^+ insertion/extraction, almost one Li^+ per formula was inserted/extracted reversibly ($0 < x < 0.7$, Li_x(MnFe-PBA)) at around 3.2 V (vs. Li/Li^+) corresponding to Fe^{2+}/Fe^{3+} redox couple. The same result was obtained for Li^+ insertion/extraction using 1 M $LiClO_4$/EC-DEC.[5]

As for Na^+ insertion/extraction, almost 0.8 Na^+ per formula was inserted, then 0.86 Na^+ per formula was extracted. These values exceed the amount of redox-active Fe site. Thus, in addition to Na^+ insertion/extraction, another contribution should be taken into account. When we started charging the cell to 4.0 V (vs. Na/Na^+) before the initial discharge process, MnFe-PBA showed a small charge capacity maybe due to the K^+ extraction accompanied by the Mn redox. The extra capacity due to the Mn redox can explain the excess amount of Na^+ insertion/extraction. The K^+ extraction may also cause the formation of insoluble $KClO_4$ at the electrode surface, which could behave as the insulating layer against the charge transfer. However, the amount of K^+ in MnFe-PBA was small, thus the effect of K^+ will be ignored in the following discussion for simplicity.

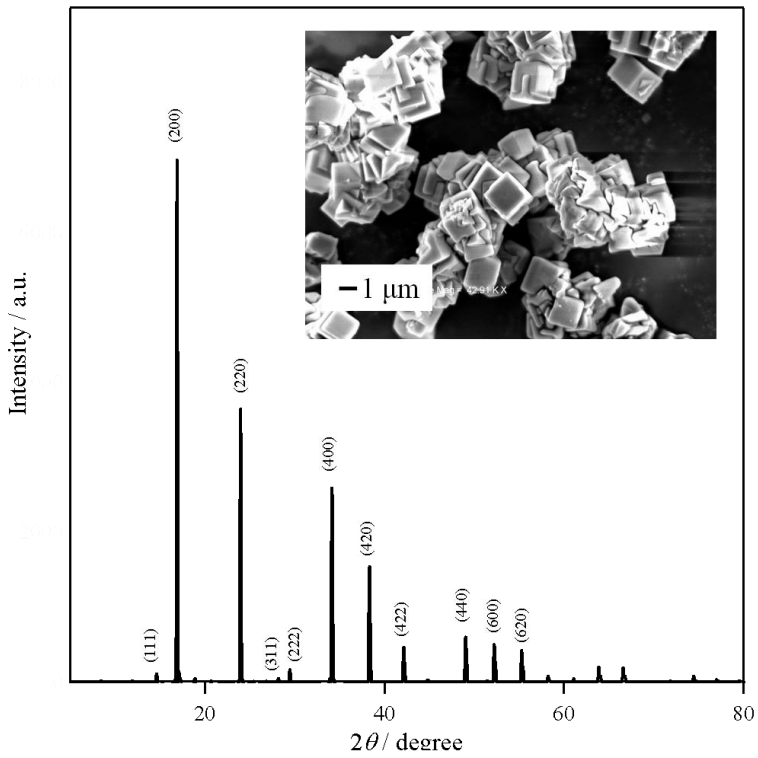

Figure 1. XRD pattern of MnFe-PBA. Inset: SEM image of MnFe-PBA. The scale bar is 1 μm.

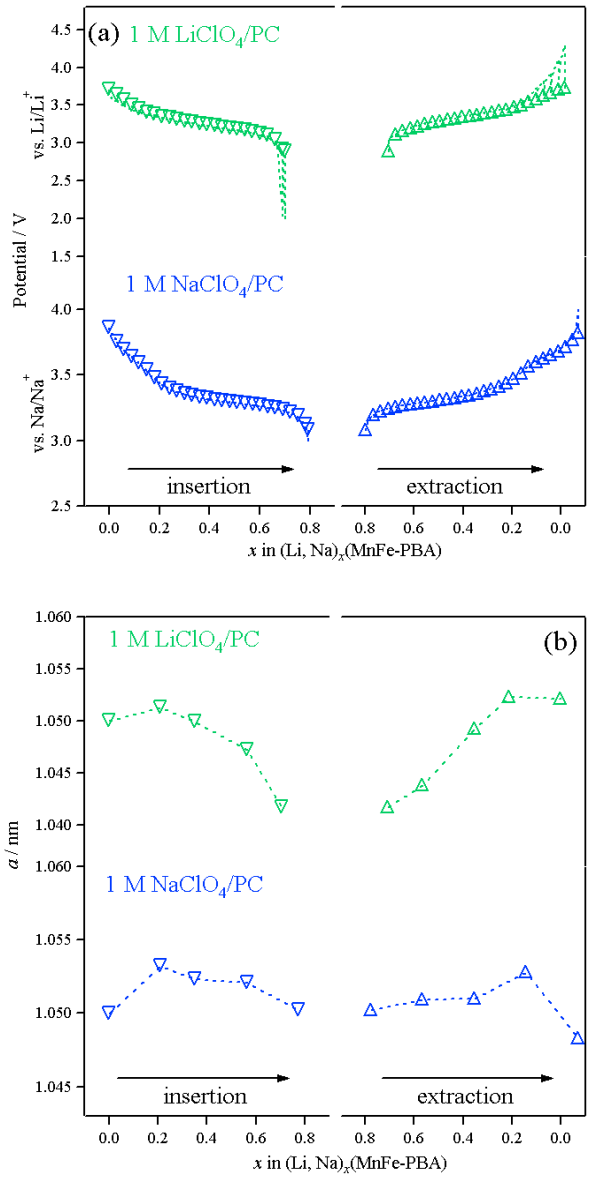

Figure 2. (a) Open-circuit voltages for MnFe-PBA during Li^+ insertion/extraction in 1 M $LiClO_4$/PC (green triangles) and Na^+ insertion/extraction in 1 M $NaClO_4$/PC (blue triangles). (b) Lattice constant change of MnFe-PBA during Li^+ (green triangles) and Na^+ (blue triangles) insertion/extraction.

Figure 2(b) shows the change in the lattice constant during the Li^+ or Na^+ insertion/extraction with the PC electrolyte. Both electrochemical reactions proceeded via solid solution state. Li^+ insertion into the PBA framework resulted in a slight shrinkage of the lattice constant from 10.4496 Å to 10.417 Å. In contrast, the lattice constant was almost constant during the Na^+ insertion/extraction. This could be explained by the difference in the ionic radius of Li^+ and Na^+. The large Na^+ (1.16 Å) penetration into the framework may prevent the lattice shrinkage. It should also be emphasized that, according to the previous reports,[15] the electrochemical Na^+ insertion/extraction in the $Fe^{3+}_4[Fe^{2+}(CN)_6]_3$ film electrode do not occur reversibly in an aqueous electrolyte (0.1 M NaCl), because Na^+ in aqueous electrolyte is strongly hydrated, and too large (= 1.83 Å) to be inserted in the host framework.[10] On the other hand, in the organic electrolyte, the solvated Na^+ can easily be desolvated, thus Na^+ insertion/extraction in MnFe-PBA could occur.

To investigate Li^+ or Na^+ insertion/extraction mechanism at the electrode-electrolyte interface, the EIS measurements at various compositions of A_x(MnFe-PBA) (A = Li or Na, x = 0.1, 0.3, 0.4 and 0.6) were carried out. x in A_x(MnFe-PBA) was varied by galvanic intermittent titration technique (GITT), and the electrochemical cell was rested for 3 h to reach the equilibrium state before each measurement.

Figure 3(a) shows a typical Nyquist plot for Li_x(MnFe-PBA) (x = 0.1, 1 M $LiClO_4$/PC, 298 K). Two semicircles corresponding to RC circuits (the interfacial charge transfer resistance in parallel with the interfacial double layer capacitance) were observed in high (from 1 Hz to 6 kHz) and low (from 10 mHz to 1 Hz) frequency ranges, respectively.

To evaluate each resistance quantitatively, nonlinear least-squares fitting was carried out. The equivalent circuit for the two-step ion insertion/extraction process (inset in Figure 3(a)) was used to analyze the spectra.[11,12] The model was established as simple as possible to minimize the number of parameters. In the equivalent circuit, R_s, R_1 and R_2 are the series resistance, interfacial charge transfer resistance at high frequency range and interfacial charge transfer resistance at low frequency range, respectively. CPE_1 and CPE_2 represent the constant phase element (CPE, $Z_{CPE} = \{T_{CPE}(j\omega)^{\alpha}\}^{-1}$, T_{CPE}, α: empirical parameters, ω: angular frequency) at high and low frequencies, respectively. The CPE is

commonly used to describe the depressed semicircle due to roughness of the electrode surface.[16] In this equivalent circuit, CPEs were used instead of capacitors because the composite electrode used in our study has a rough surface to show some porous-electrode features, as shown in the SEM image (Inset in Figure 1). In fact, the equivalent circuit with the capacitors (red broken line in Figure 3(a)) could hardly reproduce the experimental result. For the Warburg impedance, the MnFe-PBA electrode (pasted film) was regarded as the thin film electrode for simplicity, and Z_w was used corresponding to the ionic bulk diffusion in a thin film electrode material with an impermeable boundary condition and distributed relaxation time ($Z_W = \{R_W\coth(iT_W\omega)^{\beta}\}(iT_W\omega)^{-\beta}$, R_W: diffusion resistance, T_W: characteristic diffusion time, β: an empirical parameter).[17] The result of the curve-fitting is also shown in Figure 3(a), and fits well with the experimental data. The used parameters were R_s = 10.92 Ω, R_1 = 838.2 Ω, T_{CPE1} = 17.5 μF, α_{CPE1} = 0.909, R_2 = 607 Ω, T_{CPE2} = 1.79 mF, α_{CPE2} = 0.653, R_W = 5.41 μΩ, $T_W = 2.211\times10^{-11}$ s, β = 0.31118. This result suggests that the electrochemical system is well represented by the used equivalent circuit.

As mentioned in the introduction and Scheme 1, Bruce *et al*. proposed that the ad-ion model could describe the Li^+ insertion mechanism of Li_xTiS_2, in which two semicircles appear in the impedance spectra.[11,12] The equivalent circuit based on this model (an exactly same circuit shown in the inset of Figure 3(a)) has been also employed for $Li_xLa_{1/3}NbO_3$ and $LiMn_2O_4$ electrodes by Nakayama *et al*. and Kobayashi *et al*., respectively, and well explained the experimental results.[13,14] A straightforward adaptation of this model to the MnFe-PBA electrode provides the interpretation where R_1 at the low frequency is attributed to the charge-transfer process between OHP and IHP including the solvation/desolvation process, while R_2 at the high frequency is attributed to that between IHP and MnFe-PBA including the ad-ion diffusion on the electrode surface. However, there exist other interfaces in the PBA electrode, namely between the current collector – conducting carbon additive (acetylene black, AB), PBA – AB, PBA – PBA. Thus, in order to clarify the dependence of R_1 and R_2 on the Li^+ concentration in the electrolyte was measured.

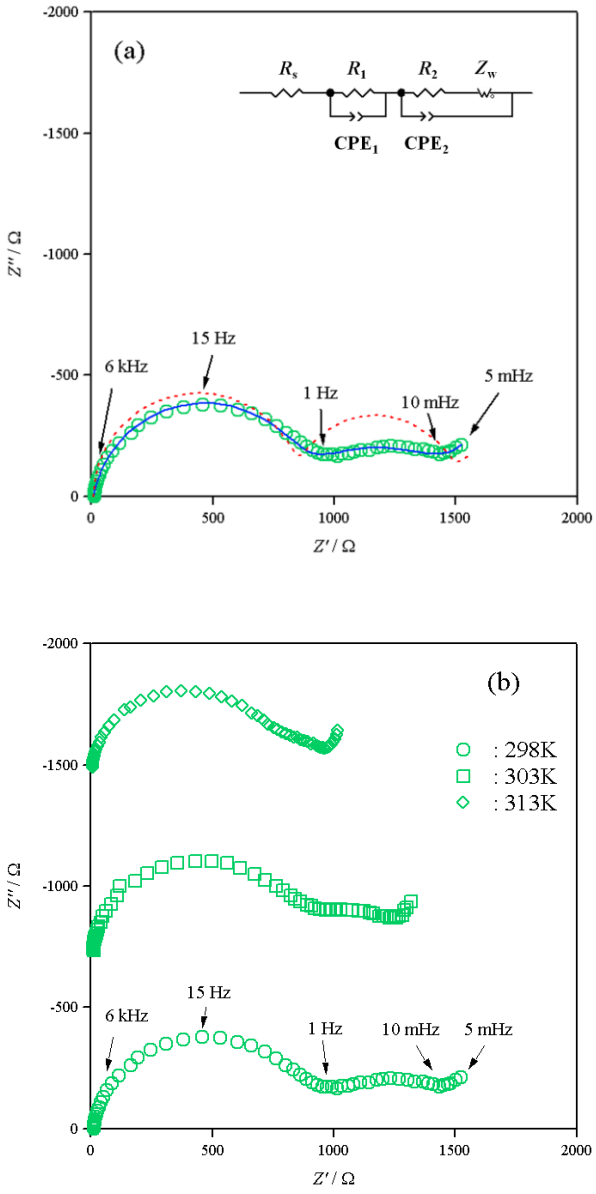

Figure 3. (a) Typical Nyquist plot (open circles) and fitted curve for Li_x(MnFe-PBA) (x = 0.1, 1 M $LiClO_4$/PC, 298 K, blue solid line: fitted curve using CPEs, red broken line: fitted curve using Capacitors instead of CPEs). Inset: equivalent circuit used in the fitting. R_s: series resistance, R_1, R_2: charge transfer resistance, CPE_1, CPE_2: constant phase element, Z_W: Warburg impedance (see text), (b) Nyquist plots for Li_x(MnFe-PBA) (x = 0.14, 1 M $LiClO_4$/PC) at 298 K, 303 K and 313 K.

Figure 4 shows R_1^{-1} and R_2^{-1} against the Li^+ concentration in the electrolyte, c [mol/L]. In this measurement, $LiClO_4$ concentration in PC was varied from 0.1 to 1 M. With increasing c, R_1^{-1} increases drastically while R_2^{-1} increases quite slightly. As shown in Scheme 1, the Li^+ transfer process at the outer electric double layer should be most sensitive to c, thus R_1 may be attributed to the Li^+ transfer resistance between OHP and IHP ($R_{CT}^{OHP/IHP}$). On the other hand, concerning R_2, a possibility of the fast interfacial electron transfer processes (*i.e.* PBA – AB) could be excluded, because the semicircle for R_2 is observed at the lower frequency region than the semicircle for R_1. Thus, the possible interfacial Li^+ transfer resistances are those between PBA – PBA involving grain boundary diffusion, and IHP – PBA involving surface diffusion. However, Figure 4 showed the slight dependence of R_2 on c. Therefore, it may be more appropriate to regard R_2 as the interfacial Li^+ transfer resistance between IHP and PBA ($R_{CT}^{IHP/PBA}$) rather than the solid-solid interfacial Li^+ transfer between PBA – PBA.

In order to clarify the mechanism in each interfacial charge transfer, the EIS spectra for A_x(MnFe-PBA) were measured at various temperatures. Figure 3(b) shows the Nyquist plots for Li_x(MnFe-PBA) (x = 0.1, 1 M $LiClO_4$/PC) at 298 K, 303 K and 313 K. By using the nonlinear least squares fitting, R_1 and R_2 were obtained at each temperature. Figure 5(a) and (b) show the temperature dependence of R_1 and R_2 for A_x(MnFe-PBA) (A = Li or Na, x = 0.3) in the temperature range from 293 K to 313 K.

With increasing temperature, both R_1 and R_2 decrease for all electrolytes. Furthermore, the plots of $\ln R_1^{-1}$ and $\ln R_2^{-1}$ against $1000/T$ showed linear relationship obeying the Arrhenius equation. This result suggests that R_1 and R_2 can be described as the thermal activation processes with the activation energies E_1 and E_2, respectively (Figure 5). Please note that the absolute values of R_1 and R_2 depend on the various factors in each cell such as the sample weight of the PBA composite electrode, thus only the activation energy has a physical meaning.

As discussed above, R_1 and R_2 can be attributed to the charge transfer resistance between the OHP and IHP, and between the IHP and electrode, respectively. Therefore, E_1 should be the activation

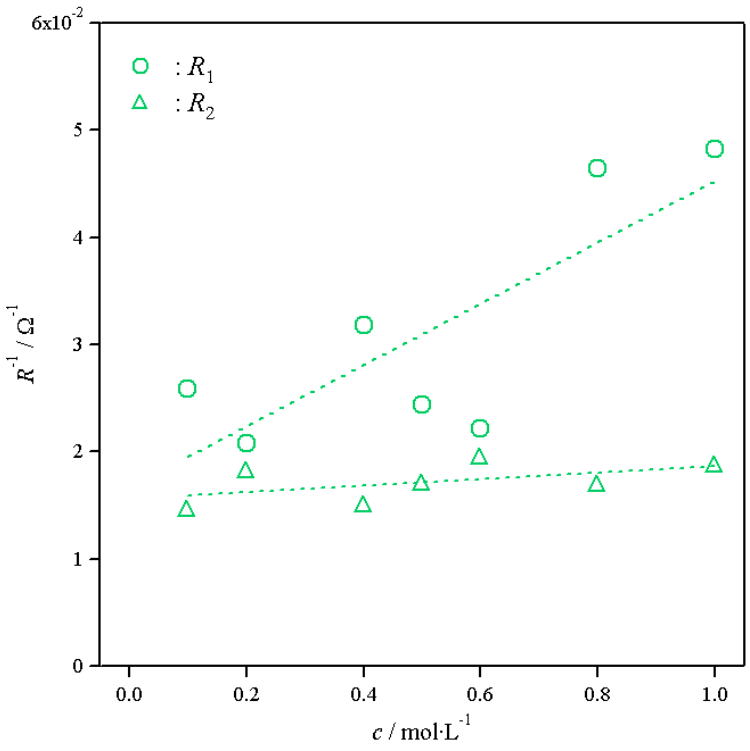

Figure 4. R_1 (open circles) and R_2 (open triangles) at the variation of the Li^+ concentration in the electrolyte; 0.1, 0.2, 0.4, 0.5, 0.6, 0.8 and 1 M $LiClO_4$/PC.

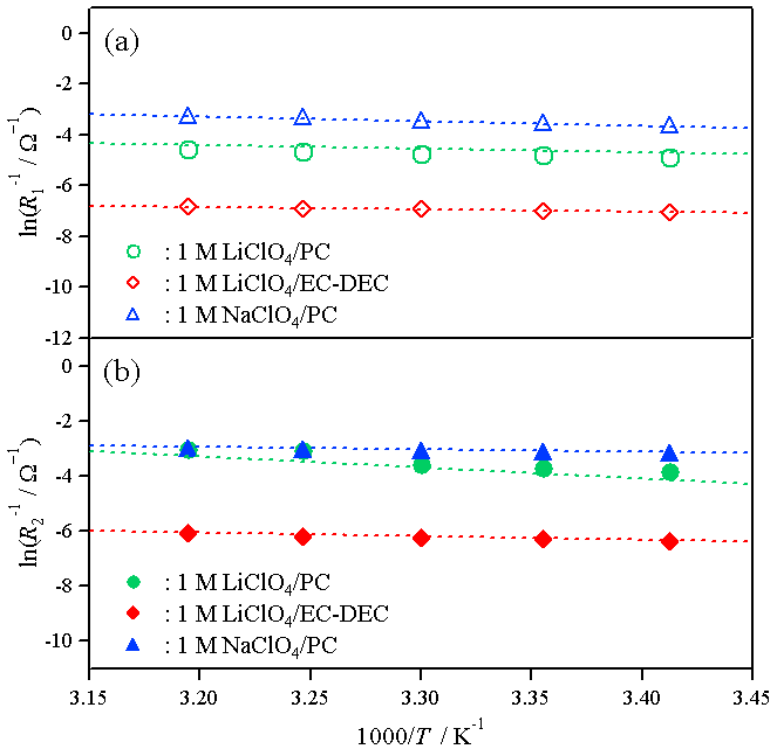

Figure 5. (a) Plots of $\ln R_1^{-1}$ against $1000/T$ for A_x(MnFe-PBA) (A = Li or Na, x = 0.3, green open circles: 1 M $LiClO_4$/PC, red open circles: 1 M $LiClO_4$/EC-DEC and blue open circles: 1 M $NaClO_4$/PC). (b) Plots of $\ln R_2^{-1}$ against $1000/T$ for A_x(MnFe-PBA) (A = Li or Na, x = 0.3, green closed triangles: 1 M $LiClO_4$/PC, red closed triangles: 1 M $LiClO_4$/EC-DEC and blue closed triangles: 1 M $NaClO_4$/PC).

energy for Li^+ migration between the OHP and IHP, including the solvation/desolvation processes. On the other hand, E_2 should be the activation energy for ad-ion diffusion on the electrode surface.

Figure 6(a) show the E_1 and E_2 as a function of x for Li_x(MnFe-PBA) in 1 M $LiClO_4$/PC. To confirm the reproducibility of the experiments, the results for two electrochemical cells were plotted. Two cells provided the comparable values for both E_1 and E_2, which clearly validates our results. As shown in the figure, E_1 was almost constant (6 ~ 10 kJ/mol) regardless of x. This result indicates that the charge transfer process between the OHP and IHP is not largely affected by x. On the other hand, E_2 showed a strong dependency on x. With increasing x from 0.1 to 0.4, E_2 decreases from 60 to 20 kJ/mol. Then, further increase in x results in the increase in E_2. This result suggests that, as deduced above, R_2 and E_2 correlate with ad-ion diffusion process on MnFe-PBA.

Figure 6(b) shows E_1 and E_2 as a function of x for Li_x(MnFe-PBA) in 1 M $LiClO_4$/EC-DEC. E_1 shows the almost constant value regardless of x. The averaged value of E_1 for ECDEC (8 kJ/mol) is almost same as that for PC (9 kJ/mol). Since E_1 includes the solvation/desolvation process, this result indicates that solvation energy with EC-DEC molecules is comparable to that by PC molecules. This result does not agree with the previous study on the liquid electrolyte/graphite interface, where the PC molecules solvate more strongly to Li^+ than the EC-DEC molecules.[18] However, according to the previous density functional theory (DFT) calculation,[19] EC molecule has a dipole moment (5.34 D) similar to that of PC (5.52 D), which results in the comparable binding energy (EC: 0.29 eV, PC: 0.31 eV). This DFT calculation supports the similar E_1 observed in our experiments.

Regarding E_2 for EC-DEC, it varies with x largely. E_2 decreases from 50 to 10 kJ/mol as x increases from 0.1 to 0.4, then increases to 35 kJ/mol (x = 0.6). The averaged value for EC-DEC (26 kJ/mol) is slightly lower than that for PC (31 kJ/mol), but comparable within an experimental error. Since E_2 corresponds to the ad-ion diffusion process, the solvent molecules may not affect E_2, resulting in similar E_2 for both EC-DEC and PC. These results are schematically summarized in Figure 7(a).

Figure 6(c) shows E_1 and E_2 as a function of x for Na_x(MnFe-PBA) in 1 M $NaClO_4$/PC. E_1 shows the almost constant value except for x = 0.6. The origin for the deviation at x = 0.6 is unclear. But if the

exceptionally high value at $x = 0.6$ is ignored, the averaged value of E_1 for Na^+ (5 kJ/mol) is smaller than that for Li^+ (9 kJ/mol). This indicates that the solvation/desolvation of Na^+ occurs more easily than that of Li^+. It is well known that less-polarizing Na^+ can solvate/desolvate more easily than more-polarizing Li^+. In fact, the lower E_1 for Na^+ was reported previously,[20] which well agrees with our results.

In contrast to E_2 for Li^+, E_2 for Na^+ does not depend largely on x. E_2 for Na^+ increases from 10 to 20 kJ/mol as x increases. The averaged value of E_2 for Na^+ (15 kJ/mol) is much smaller than that for Li^+ (31 kJ/mol). As mentioned above, E_2 includes the ad-ion diffusion on the electrode surface. Therefore, less-polarizing Na^+ may diffuse on the PBA surface more easily than more-polarizing Li^+. This is consistent with the fact that Na^+ in the bulk solid diffuses much faster than Li^+.[21-23] These results are schematically summarized in Figure 7(b).

Compared to the typical cathode materials, MnFe-PBA showed smaller activation energies for the interfacial charge transfer processes. For example, the activation energy in 1M $LiClO_4$/PC was reported as 46 kJ/mol for *c*-axis-oriented $LiCoO_2$ thin film,[24] and 47 kJ/mol for MgO-modified $LiCoO_2$ thin film.[25] Although these values were obtained from the equivalent circuit with a single RC circuit, they are generally higher than E_1 and E_2 for the MnFe-PBA electrode. Furthermore, both E_1 and E_2 for $LiMn_2O_4$ in 1 M $LiClO_4$/PC (E_1 = 19kJ/mol and E_2 = 54 kJ/mol based on the same equivalent circuit in our study) were higher than those for MnFe-PBA in 1 M $LiClO_4$/PC.[14] The faster charge transfer kinetic at the interface could contribute to the higher power application.

The activation energy for Na^+ transfer at the electrode-electrolyte interface for other electrode materials has not been reported. However, the activation energy (obtained from the equivalent circuit with a single RC circuit) at the solid electrolyte-liquid electrolyte interfaces was determined as 35 kJ/mol between $Na_3Zr_{1.88}Y_{0.12}Si_2PO_{12}$ (NASICON) and 0.05 M $NaCF_3SO_3$/PC, and 52 kJ/mol between Na-β''-alumina and 0.05 M $NaCF_3SO_3$/PC.[26,27] These values are higher than E_1 and E_2 for MnFe-PBA. Therefore, it is speculated that the interfacial Na^+ transfer processes for MnFe-PBA has lower potential barrier than that on the solid electrolyte surface.

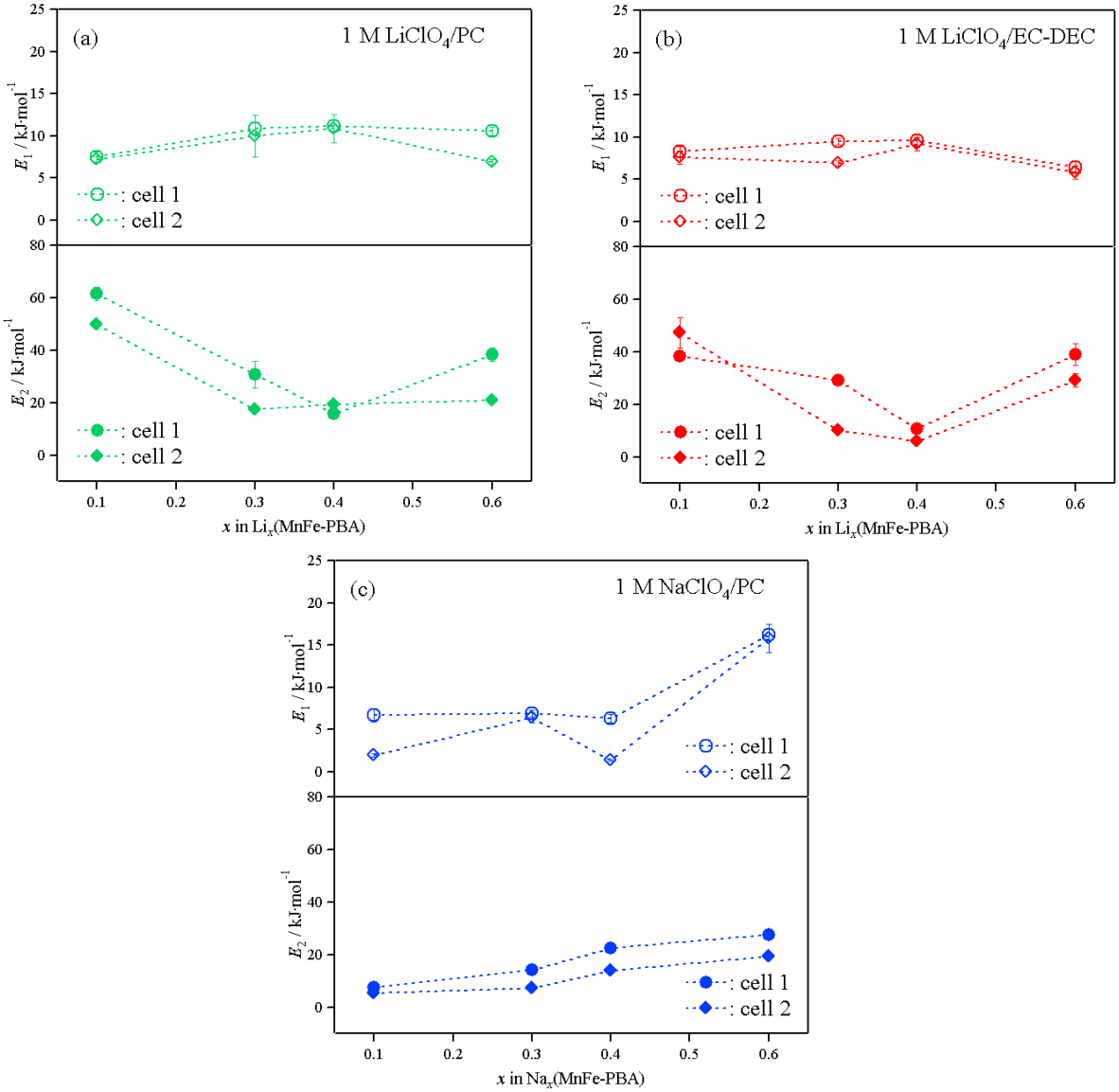

Figure 6. (a) Plots of E_1 and E_2 as a function of x for Li_x(MnFe-PBA) (x = 0.1, 0.3, 0.4 and 0.6, 1 M $LiClO_4$/PC) in cell 1 and cell 2, (b) Plots of E_1 and E_2 as a function of x for Li_x(MnFe-PBA) (x = 0.1, 0.3, 0.4 and 0.6, 1 M $LiClO_4$/EC-DEC) in cell 1 and cell 2 and (c) Plots of E_1 and E_2 as a function of x for Na_x(MnFe-PBA) (x = 0.1, 0.3, 0.4 and 0.6, 1 M $NaClO_4$/PC) in cell 1 and cell 2.

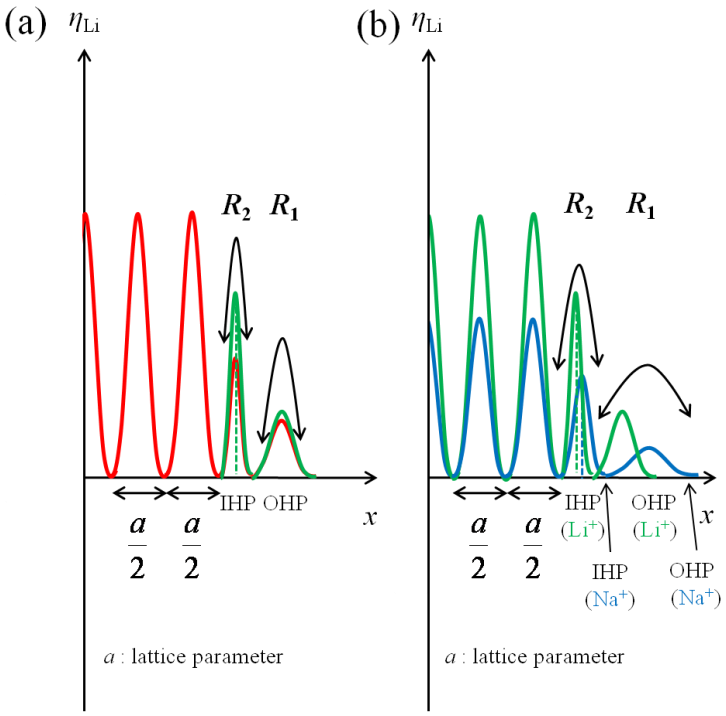

Figure 7. Schematic diagram of electrochemical potential for (a) Li^+ in 1 M $LiClO_4$/PC (green) and 1 M $LiClO_4$/EC-DEC (red), (b) Li^+ in 1 M $LiClO_4$/PC (green) and Na^+ in 1 M $NaClO_4$/PC (blue).

Finally, the effect of the interfacial charge transfer resistance on the high-rate charge/discharge capability was investigated. To compare the rate capability, charge-discharge measurements were carried out at the various current densities from 50 mA/g to 1 A/g. In general, the rate performance is influenced not only by the interfacial charge transfer and Li^+ diffusion in the electrode, but also by various other factors such as the electrode surface area, ionic activity, ionic conductivity of the electrolyte, electronic conductivity of the electrode, *etc*. Nevertheless, in the following discussion, the influence of E_1 and E_2 on the rate capability was considered. Figure 8(a) shows the charge-discharge curves at various current densities. In case of Li^+ insertion/extraction, the charge-discharge capacity with 1 M $LiClO_4$/EC-DEC showed a decrease from 62 mAh/g at 50 mA/g to 42 mAh/g at 1 A/g (31 % decrease), while that with 1 M $LiClO_4$/PC showed a decrease from 63 mAh/g at 50 mA/g to 36 mAh/g at 1 A/g (42 % decrease). The rate capability as a function of current density for each electrolyte in Figure 8(b) clearly shows that the rate capability for EC-DEC electrolyte is better than that for the PC electrolyte. The Li^+ bulk diffusion in the MnFe-PBA electrode must be same for both electrolytes. Furthermore, as discussed in the above section, both PC and EC-DEC electrolytes showed comparable E_1 and E_2 values. Therefore, the better rate capability for EC-DEC may be ascribed to the higher Li^+ conductivity in EC-DEC (Li-ion conductivity in 1 M $LiClO_4$/EC-DEC: 6.4×10^{-3} S/cm,[28] PC: 6.0×10^{-3} S/cm[29]).

In case of Na^+, the charge/discharge capacity showed a decrease from 80 mAh/g at 50 mA/g to 63 mAh/g at 1 A/g (21 % decrease) (Figure 8(a)). The rate capability for Na^+ in Figure 8(b) is considerably better than that for Li^+. It is well known that the Na^+ diffusion in the bulk solid is much faster than the Li^+. Therefore, the better rate capability for Na^+ could be explained by the faster bulk diffusion in the solid. However, Na^+ showed lower E_1 and E_2 than Li^+. Thus, the lower potential barrier at the IHP/PBA interface may also contribute to the faster Na^+ transfer, and the better rate capability.

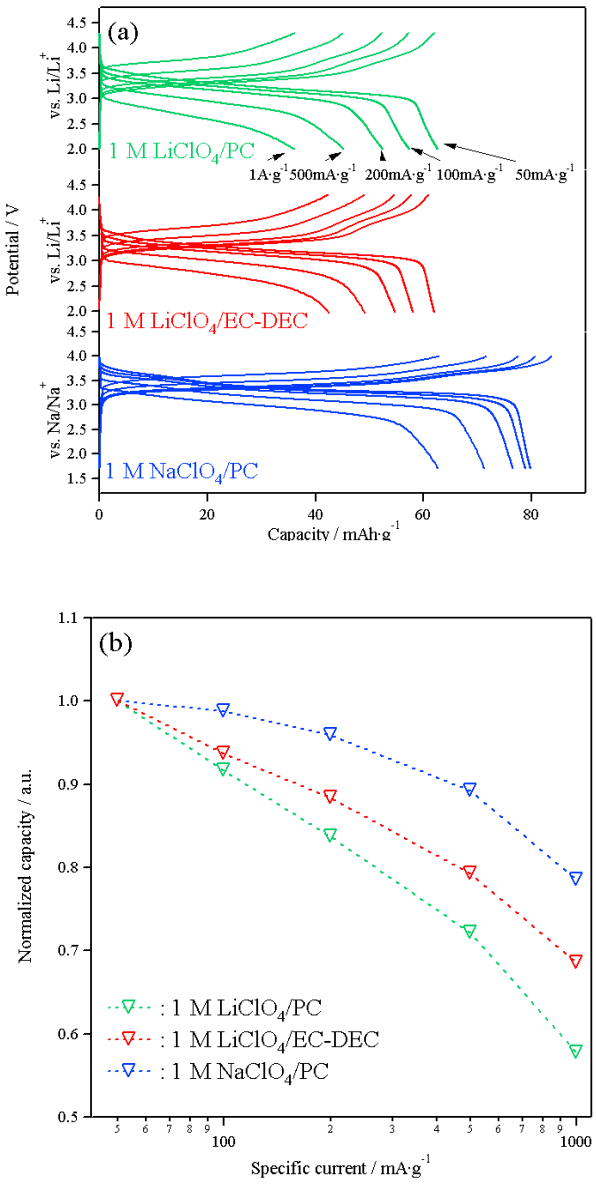

Figure 8. (a) Rate capabilities of MnFe-PBA (green lines: 1 M $LiClO_4$/PC, red lines: 1 M $LiClO_4$/EC-DEC and blue lines: 1 M $NaClO_4$/PC), (b) normalized discharge capacity (green open triangles: 1M $LiClO_4$/PC, red open triangles: 1M $LiClO_4$/EC-DEC and blue open triangles: 1 M $NaClO_4$/PC) at various current densities; 50 m, 100 m, 200 m, 500 m and 1 A/g.

2.4. Conclusions

Alkali-ion (Li^+ or Na^+) transfer at the MnFe-PBA electrode-electrolyte interface was investigated by EIS. Alkali-ion transfer at the MnFe-PBA electrode-electrolyte interface was suggested to involve two processes. It was interpreted that one was ion transfer between the OHP and IHP, including the solvation/desolvation process, the other was ion transfer between the IHP and electrode, including the ad-ion diffusion on the electrode surface. In case of Li^+ transfer in the PC electrolyte, E_1 was almost constant within the whole composition range of $0.1 < x < 0.6$ in Li_xMnFe-PBA, while E_2 depended largely on x regardless of the electrolyte. Both E_1 and E_2 in 1 M $LiClO_4$/PC were comparable to those in 1 M $LiClO_4$/EC-DEC, which is consistent to the DFT calculation in the previous report.

In contrast to Li^+ transfer, the significant dependence of E_2 on x was not observed for Na^+ transfer. However, the averaged value of E_2 for Na^+ was much lower than that for Li^+. This may be one of the origins for the excellent rate capability of Na^+. The high charge/discharge rate experiments for the MnFe-PBA clearly demonstrated the effect of the charge transfer processes.

References

(2-1) Armand, M.; Tarascon, J. M. *Nature* **2008**, *451*, 652-657.

(2-2) Wang, Y.; Cao, G.; *Adv. Mater*. **2008**, *20*, 2251-2269.

(2-3) Okubo, M.; Hosono, E.; Kim, J.-D.; Enomoto, M.; Kojima, N.; Kudo, T.; Zhou, H.; Honma, I. *J. Am. Chem. Soc*. **2007**, *123*, 7444-7452.

(2-4) Okubo, M.; Mizuno, Y.; Yamada, H.; Kim, J.-D.; Hosono, E.; Zhou, H.; Kudo, T.; Honma, I. *ACSnano* **2010**, *4*, 741-752.

(2-5) Okubo, M.; Asakura, D.; Mizuno, Y.; Kim, J.-D.; Mizokawa, T.; Kudo, T.; Honma, I.; *J. Phys. Chem. Lett.* **2010**, *1*, 2063-2071.

(2-6) Okubo, M.; Asakura, D.; Mizuno, Y.; Kudo, T.; Zhou, H.; Okazawa, A.; Kojima, N.; Ikedo, K.; Mizokawa, T.; Honma, I. *Angew. Chem. Int. Ed*. **2011**, *50*, 6269-6274.

(2-7) Asakura, D.; Okubo, M.; Mizuno, Y.; Kudo, T.; Zhou, H.; Amemiya, K.; de Groot, F. M. F.; Chen, J.-L.; Wang, W.-C.; Glans, P.-A.; Chang, C.; Guo, J.; Honma, I. *Phys. Rev. B* **2011**, *84*, 045117.

(2-8) Imanishi, N.; Morikawa, T.; Kondo, J.; Takeda, Y.; Yamamoto, O.; Kinugasa, N.; Yamagishi, T. *J. Power Sources* **1999**, *79*, 215-219.

(2-9) Imanishi, N.; Morikawa, T.; Kondo, J.; Yamane, R.; Takeda, Y.; Yamamoto, O.; Sakaebe, H.; Tabuchi, M.; *J. Power Sources* **1999**, *81-82*, 530-534.

(2-10) R. Vittal, K.-J. Kim, H. Gomathi, V. Yegnaraman, J. Phys. Chem. B 112 (2008) 1149.

(2-11) Bruce, P. G.; Saidi, M. Y. *J. Electroanal. Chem.* **1992**, *322*, 93-105.

(2-12) Bruce, P. G.; Saidi, M. Y. *Solid State Ion*. **1992**, *51*, 187-190.

(2-13) Nakayama, M.; Ikuta, H.; Uchimoto, Y.; Wakihara, M. *J. Phys. Chem. B* **2003**, *107*, 10603-10607.

(2-14) Kobayashi, S.; Uchimoto, Y. *J. Phys. Chem. B*, **2005**, *109*, 13322-13326.

(2-15) Itaya, K.; Ataka, T.; Toshima, S. *J. Am. Chem. Soc*. **1982**, *104*, 4767-4772.

(2-16) Barsoukov, E.; Macdonald, J.R.; Impedance spectroscopy, John Wiley & Sons, Inc., Hoboken, New Jersey, 2005.

(2-17) Ho, C.; Raistrick, I. D.; Huggins, R. A. *J. Electrochem. Soc.*, **1980**, *127*, 343-350.

(2-18) Doi, T.; Iriyama Y.; Abe, T.; Ogumi, Z. *J. Electrochem. Soc*. **2005**, *152*, A1521-A1525.

(2-19) Park, M. H.; Lee, Y. S.; Lee, H.; Han, Y.-K. *J. Power Sources* **2011**, *196*, 5109-5114.

(2-20) Frolov, A. I.; Rozhin, A. G.; Fedorov, M. V. *ChemPhysChem* **2010**, *11*, 2612-2616.

(2-21) Gao, Z.; Bobacka, J.; Ivaska, A. *Electrochim. Acta* **1993**, *38*, 379-385.

(2-22) Malev, V.; Kurdakova, V.; Kondratiev, V.; Zigel, V. *Solid State Ion.* **2004**, *169*, 95-104.

(2-23) Malik, M. A.; Kulesza, P. J.; Marassi, R.; Nobili, F.; Miecznikowsli, K.; Zamponi, S. *Electrochim. Acta* **2004**, *49*, 4253-4258.

(2-24) Yamada, I.; Iriyama, Y.; Abe, T.; Ogumi, Z. *J. Power Sources* **2007**, *172*, 933-937.

(2-25) Iriyama, Y.; Kurita, H.; Yamada, I.; Abe, T.; Ogumi, Z. *J. Power Sources* **2004**, *134*, 111-116.

(2-26) Sagane, F.; Abe, T.; Iriyama, Y.; Ogumi, Z. *J. Power Sources* **2005**, *146*, 749-752.

(2-27) Sagane, F.; T. Abe, T.; Ogumi, Z. *J. Power Sources* **2010,** *195*, 7466-7470.

(2-28) Morita, M.; Yamada, O.; Ishikawa, M. *J. Appl. Electrochem*. **1998**, *28*, 209-213.

(2-29) Tobishima, S.-I.; Yamaki, J.-E.; Okada, T. *Electrochim. Acta* **1984**, *29*, 1471-1476.

Chapter 3

Hydration Effect on Activation Energy for Electrode-Electrolyte Interfacial Charge Transfer

3.1. Introduction

High power, durable and low cost batteries have attracted much attention because of strong industrial demands for their application to grid-scale energy storage.[1,2] Although a Li-ion rechargeable battery powers most consumer electronics, the used non-aqueous electrolyte is too expensive. In contrast, aqueous batteries such as an aqueous Li-ion battery or aqueous Na-ion battery are promising, because the aqueous electrolyte is inexpensive and some intercalation electrodes can show both durability and high power with the aqueous electrolytes.

It is well known that Li^+ and Na^+ in both organic[3-7] and aqueous electrolytes[8,9] can be electrochemically intercalated into Prussian blue analogs (PBAs), because PBAs ($A_xM[M'(CN)_6]_{1-y}\cdot\square_y\cdot nH_2O$, A; alkali metal, M, M'; transition metal, □; $[M'(CN)_6]$ vacancy, hereafter denoted MM'-PBA) possess both the redox active sites and the mixed conductivity within the cyanide-bridged porous structure. Very recently, Wessells *et al.* reported application of PBAs to the electrode materials in the aqueous batteries,[10-13] which pronounces the long cycle life, high power, good energy efficiency, safety and low cost of the aqueous batteries with the PBA electrodes. For example, NiFe-PBA allowed 66 % retention of the initial capacity at an extremely high (41.7 C) rate with Na^+ aqueous electrolyte. The high-rate capability with aqueous electrolyte was much better than that with organic electrolyte.[6] However, the origin for the high power of the PBA electrodes with aqueous electrolyte has not been clarified to date.

The electrode-electrolyte interfacial charge transfer is a fundamental step in the charge/discharge process, and higher power output requires faster interfacial charge transfer with lower activation energy.[6] In this study, the activation energy for the interfacial charge transfer was estimated for the PBA electrode with both organic and aqueous electrolytes by the electrochemical impedance

spectroscopy (EIS). The temperature dependence of the interfacial charge transfer resistance could provide the activation energy, which sheds light on the microscopic understanding of the interfacial charge transfer, and furthermore clarifies the origin for the high power of the aqueous batteries with the PBA electrodes.

3.2. Experimental Methods

NiFe-PBA thin film was fabricated on an Indium Tin oxide (ITO) substrate (hereafter denoted NiFe-PBA/ITO) by using a sequential deposition method.[14] Typically, an ITO substrate was immersed for 1 min. in an aqueous solution of 12 mM $NiCl_2 \cdot 6H_2O$, and then rinsed with distilled water. The rinsed ITO substrate was immersed for 1 min. in an aqueous solution of 8 mM $K_3Fe(CN)_6$, and rinsed with distilled water. After repeating 40 cycles of these processes, the ITO substrate was dried in vacuo for 12 h. For comparison, a powder sample of NiFe-PBA was synthesized by a precipitation method, in which an aqueous solution of 0.15 M $NiCl_2 \cdot 6H_2O$ was added dropwise to an aqueous solution of 0.1 M $K_3Fe(CN)_6$. The precipitate was centrifuged, washed with distilled water, and then dried in vacuo for 24 h.

Powder X-ray diffraction (XRD) measurement was carried out on a Bruker D8 Advance using Cu $K\alpha$ radiation in steps of 0.01˚ over the 2θ range of 10 – 60˚. SEM measurement was carried out on a Carl Zeiss Supra 35.

For the electrochemical measurements, three-electrode glass cell was used. NiFe-PBA/ITO was used for the working electrode. For Li^+ or Na^+ intercalation/extraction in organic electrolytes, Li or Na metal was used for the counter and reference electrodes, and 1 M $LiClO_4$/propylene carbonate (PC) or 1 M $NaClO_4$/PC was used for the electrolyte. Mg metal is potentially passivated in polar organic electrolyte. Therefore, for Mg^{2+} intercalation/extraction in organic electrolyte, the reference electrode was an Ag wire immersed in 0.01 M $AgClO_4$ and 0.1 M tetrabutylammonium perchlorate (TBAP)/PC, while the counter electrode was a Pt mesh. For the electrolyte, 1 M $Mg(ClO_4)_2$/PC was used. The reference electrode was calibrated in 1 M $Mg(ClO_4)_2$/PC containing 1 M ferrocene and 0.1 M TBAP.

For Li^+, Na^+ and Mg^{2+} intercalation/extraction in an aqueous electrolyte, an Ag/AgCl in 3 M NaCl was used for the reference electrode. An excess amount of the discharged NiFe-PBA electrode was used as a counter electrode according to the literature.[10] An aqueous solution of 1 M $LiNO_3$, 1 M $NaNO_3$ or 1 M $Mg(NO_3)_2$ was used as an aqueous electrolyte. The cut-off voltages were 2.0 V and 4.3 V (vs. Li/Li^+) for Li^+ intercalation/extraction in 1 M $LiClO_4$/PC, 2.0 V and 4.0 V (vs. Na/Na^+) for Na^+ intercalation/extraction in 1 M $NaClO_4$/PC and 0 V and 1 V (vs. Ag/AgCl) for Li^+, Na^+ or Mg^{2+} intercalation/extraction in the aqueous solutions. The electrochemical impedance spectra were recorded with a frequency analyzer (SI 1250, Solatron) at the frequency ranging from 5 mHz to 50 kHz with an amplitude of 10 mV.

3.3. Results and Discussion

A thin film electrode of NiFe-PBA (NiFe-PBA/ITO) was employed for the EIS study, rather than the composite electrode, to avoid the complexities caused by various coexisting interfaces in the composite electrode. NiFe-PBA/ITO was fabricated by a sequential deposition method.[14] Figure 1 shows the X-ray diffraction (XRD) pattern for NiFe-PBA/ITO. The weak peak at 2θ = 17.3º corresponds to the (200) reflection of NiFe-PBA by comparison with that for the NiFe-PBA powder. Therefore, NiFe-PBA thin film was successfully deposited on the ITO substrate. The cross-section SEM image confirmed the deposited NiFe-PBA thin film on the ITO substrate, and revealed the mean thickness of about 200 nm (Figure 2).

Before the EIS measurements, electrochemical ion intercalation/extraction for NiFe-PBA/ITO was examined with both organic and aqueous electrolytes. Figure 3(a) shows the cyclic voltammetry (CV) for NiFe-PBA/ITO with 1 M $LiClO_4$/PC (black solid line), 1 M $NaClO_4$/PC (blue solid line) and 1 M $Mg(ClO_4)_2$/PC (red solid line) at the scan rate of 1 mV/s. Although Li/Li^+, Na/Na^+, and Ag/Ag^+ were respectively used as the reference electrode for the Li^+, Na^+ and Mg^{2+} organic electrolytes, the potential in Figure 3(a) is normalized to the value against normal hydrogen electrode (NHE) for clarity (Li/Li^+ = -3.0 V vs. NHE, Na/Na^+ = -2.7 V vs. NHE, and Ag/Ag^+ = +1.0 V vs. NHE). In the Li^+ organic

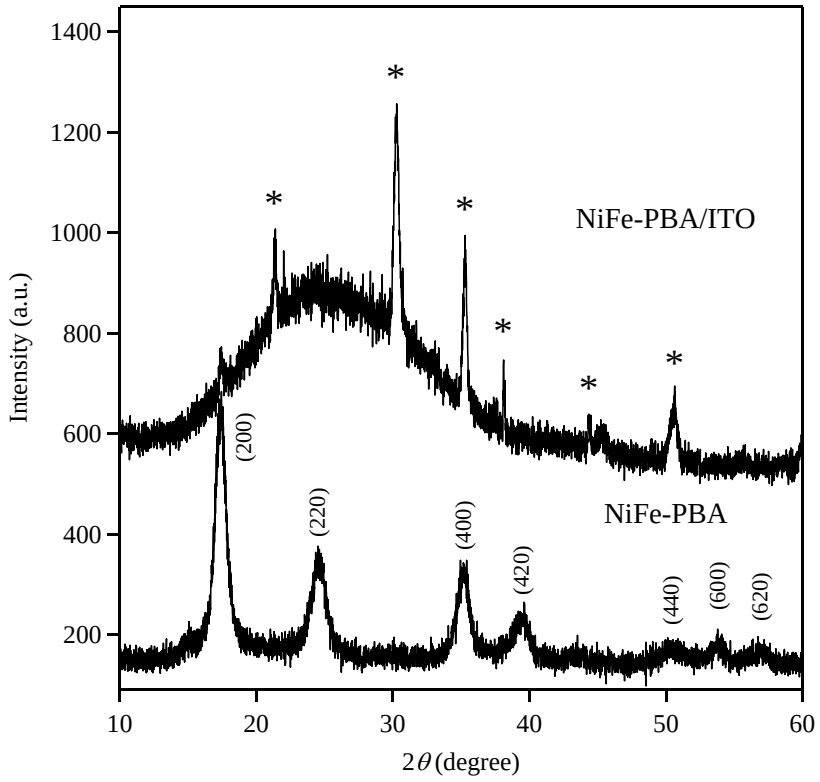

Figure 1. XRD patterns for power sample of NiFe-PBA and NiFe-PBA/ITO. *: Bragg peaks of ITO.

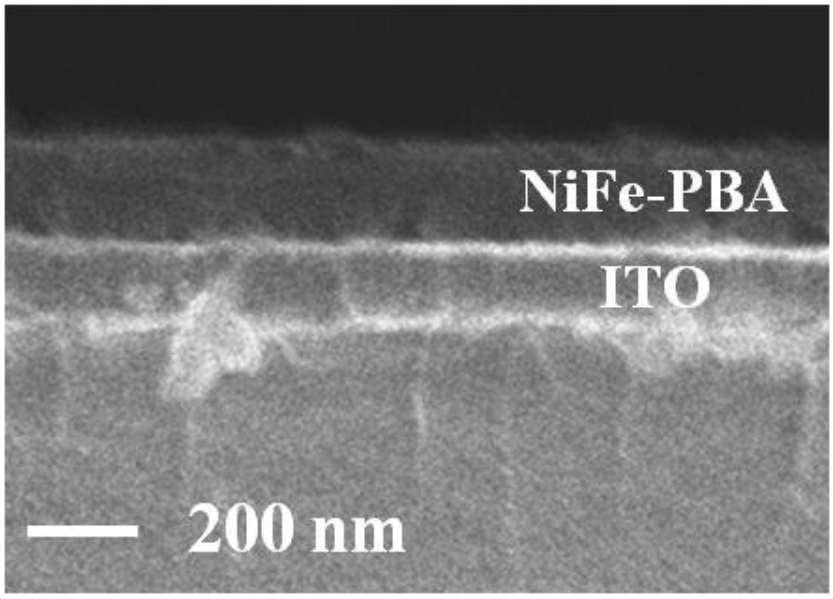

Figure 2. Cross-section SEM image for NiFe-PBA/ITO.

electrolyte, NiFe-PBA/ITO showed a cathodic peak at 0.13 V vs. NHE and an anodic peak at 0.27 V vs. NHE, while that in the Na^+ organic electrolyte showed a cathodic peak at 0.49 V vs. NHE and an anodic peak at 0.57 V vs. NHE. These peaks should be ascribed to the Li^+ or Na^+ intercalation/extraction reaction, which agrees with the previous reports.[3-7] The peak separation ΔE_p of 140 mV for Li^+ is larger than that for Na^+ (80 mV). Since ΔE_p depends on the diffusion coefficient in the bulk PBA and the rate constant at PBA-electrolyte interface, large ΔE_p for Li^+ suggests that Li^+ diffusion or interfacial Li^+ transfer is slower than that of Na^+. In contrast, NiFe-PBA/ITO showed no peak in the Mg^{2+} organic electrolyte, which suggests that Mg^{2+} in PC can hardly be inserted into NiFe-PBA.

Figure 3(b) shows the CVs for NiFe-PBA/ITO in aqueous solutions of 1 M $LiNO_3$ (black solid line), 1 M $NaNO_3$ (blue solid line) and 1 M $Mg(NO_3)_2$ (red solid line), respectively. Although Ag/Ag^+ was used as the reference electrode for all the aqueous electrolytes, the potential in Figure 3(b) is normalized to the value against NHE for clarity (Ag/Ag^+ = +0.2 V vs. NHE). With the Li^+ aqueous electrolyte, NiFe-PBA/ITO showed a cathodic peak at 0.36 V vs. NHE and an anodic peak at 0.44 V vs. NHE, while that with the Na^+ aqueous electrolyte showed a cathodic peak at 0.56 V vs. NHE and an anodic peak at 0.56 V vs. NHE. Furthermore, NiFe-PBA/ITO showed a cathodic peak at 0.52 V vs. NHE and an anodic peak at 0.62 V vs. NHE in the Mg^{2+} aqueous electrolyte. According to the previous reports, these peaks should also be ascribed to the Li^+, Na^+ or Mg^{2+} intercalation/extraction in NiFe-PBA/ITO.[8-13,15-17] ΔE_p for Li^+ is 80 mV, which is smaller than that for Li^+ in PC (140 mV). This result suggests that the aqueous electrolyte accelerates the Li^+ diffusion or interfacial Li^+ transfer. The acceleration of reaction kinetics is also observed for Na^+, in which ΔE_p decreases from 80 mV (PC) to 0 mV (the aqueous electrolyte). ΔE_p of 0 mV is explained by the uniform Na^+ concentration within the PBA film (fast Na^+ diffusion) and reversible interfacial reaction (fast interfacial Na^+ transfer), and is frequently observed for the thin film electrode with fast kinetics. This result also supports the acceleration effect of the aqueous electrolyte.

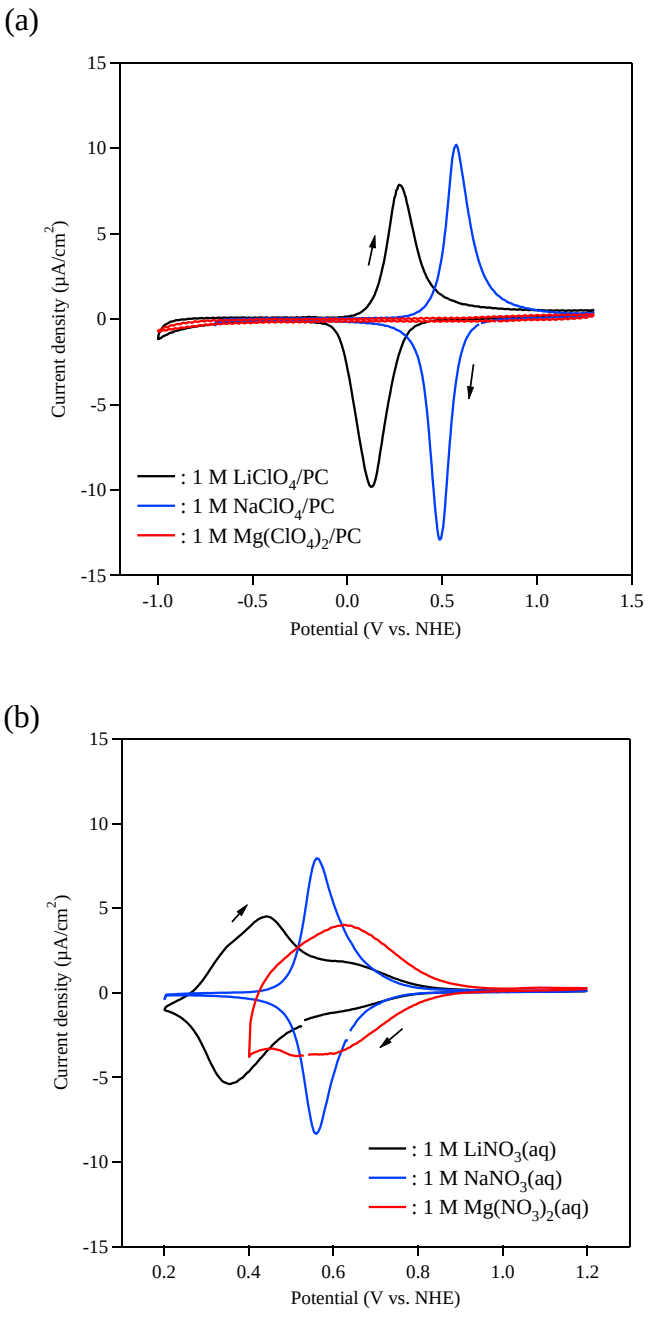

Figure 3. (a) Cyclic voltammograms for NiFe-PBA/ITO in 1 M $LiClO_4$/PC (black solid line), 1 M $NaClO_4$/PC (blue solid line) and 1 M $Mg(ClO_4)_2$/PC (red solid line). The potential is normalized to the value vs. NHE (Li/Li^+ = -3.0 V vs. NHE, Na/Na^+ = -2.7 V vs. NHE and $Ag/AgClO_4$ = +1.0 V vs. NHE). The scan rate is 1 mV/s. (b) Cyclic voltammograms for NiFe-PBA/ITO in aqueous solutions of 1 M $LiNO_3$ (black solid line), 1 M $NaNO_3$ (blue solid line) and 1 M $Mg(NO_3)_2$ (red solid line). The potential is normalized to the value vs. NHE (Ag/AgCl = +0.2 V vs. NHE).The scan rate is 1 mV/s.

To investigate the interfacial charge transfer more quantitatively, the EIS measurements were carried out. Before the EIS measurement, the electrochemical cell was held at a certain potential (E_i) for 2h to reach the equilibrium state. Figure 4 shows the typical Nyquist plot for NiFe-PBA/ITO with an aqueous solution of 1 M $LiNO_3$ (E_i = 0.5 V vs. NHE, 293 K). One semicircle corresponding to a RC circuit (the interfacial charge transfer resistance in parallel with the interfacial double layer capacitance) was observed in the frequency range from 15 Hz to 50 kHz. To evaluate the Nyquist plot quantitatively, nonlinear least-squares fitting was carried out. The equivalent circuit for the typical ion intercalation/extraction process (inset in Figure 4) was used to analyze the spectra. In the equivalent circuit, R_s and R_{CT} are the series resistance and interfacial charge transfer resistance, respectively. CPE represents the constant phase element (CPE, $Z_{CPE} = \{T_{CPE}(j\omega)^{\alpha}\}^{-1}$, T_{CPE}, α: empirical parameters, ω: angular frequency). The CPE is commonly used to describe the depressed semicircle due to roughness of the electrode surface.[18] In this equivalent circuit, CPE was used instead of capacitor because the NiFe-PBA thin film in our study has a rough surface as shown in the SEM image for the surface of NiFe-PBA/ITO (Figure 5). For the Warburg impedance, Z_W was used corresponding to the ionic bulk diffusion in a thin film electrode material with an impermeable boundary condition and distributed relaxation time ($Z_W = \{R_W \coth(iT_W\omega)^{\beta}\}(iT_W\omega)^{-\beta}$, R_W: diffusion resistance, T_W: characteristic diffusion time, β: an empirical parameter).[19] The result of curve-fitting is also shown in Figure 4, and fits well with the experimental data. The used parameters were R_s = 70.82 Ω, R_{CT} = 69.49 Ω, T_{CPE} = 12.7 μF, α_{CPE} = 0.939, R_W = 1.51 Ω, T_W = 8.12 × 10^{-4} s and β = 0.349. The good fit suggests that the electrochemical system is well represented by the used equivalent circuit.

In order to clarify the mechanism in interfacial charge transfer, the EIS spectra for NiFe-PBA/ITO were measured at various temperatures. Figure 4(a), (b) and (c) shows the typical Nyquist plots for NiFe-PBA/ITO with various electrolytes (1 M $LiClO_4$/PC, aqueous solution of 1 M $LiNO_3$ and aqueous solution of 1 M $Mg(NO_3)_2$). The temperature dependent EIS spectra for the other systems are shown in Figure 6(d) and (e). As shown in the figures, the radius of the semicircle decreases with increasing the temperature for all systems. R_{CT} at each temperature was estimated from the nonlinear least squares

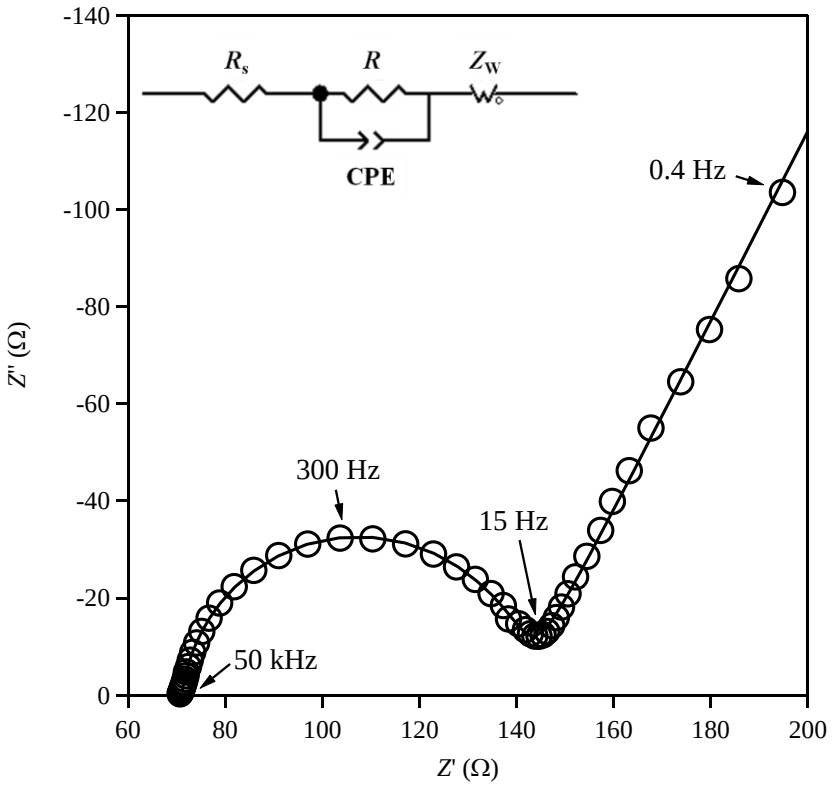

Figure 4. Typical Nyquist plot (opened circles) and fitted curve (solid line) for NiFe-PBA/ITO with aqueous solution of 1 M $LiNO_3$ (E_i = 0.5 V vs. NHE). Inset: equivalent circuit used in the fitting. R_s: series resistance, R: charge transfer resistance, CPE: constant phase element, Z_W: Warburg impedance.

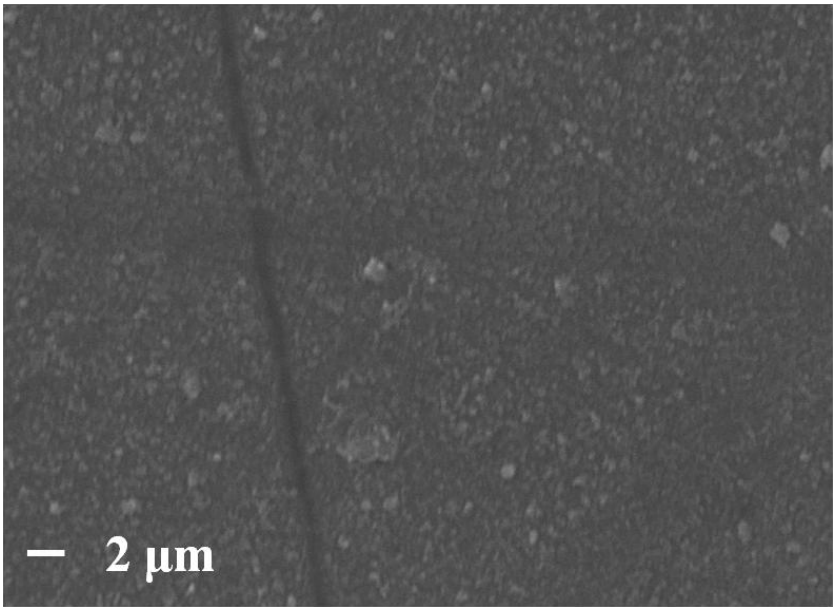

Figure 5. SEM image for the surface of NiFe-PBA/ITO.

fitting.

Figure 7 shows the temperature dependence of R_{CT} for NiFe-PBA/ITO in 1 M $LiClO_4$/PC (E_i = 0.2 V vs. NHE, black opened circles), 1 M $NaClO_4$/PC (E_i = 0.4 V vs. NHE, blue opened circles), aqueous solution of 1 M $LiNO_3$ (E_i = 0.5 V vs. NHE, black closed circles), 1 M $NaNO_3$ (E_i = 0.6 V vs. NHE, blue closed circles) and 1 M $Mg(NO_3)_2$ (E_i = 0.5 V vs. NHE, red closed circles) in the temperature range from 293 to 313 K. With increasing temperature, R_{CT} decreased for all systems. The plot of $\ln R_{CT}^{-1}$ vs. $1000/T$ showed linear relationship obeying the Arrhenius equation. This result suggests that R_{CT} can be described as the thermal activation process with the activation energy E_a for interfacial charge transfer. Table 1 summarizes E_a for various electrolytes.

As shown in Table 1, E_a for Li^+ (60.8 kJ/mol) is larger than that for Na^+ (43 kJ/mol) in PC. Because the intercell bottleneck radius in the hard sphere model of PBA is about 1.6 Å, PC molecule is too large to be co-intercalated in PBA. Thus, all the solvated PC should be desolvated completely during the interfacial charge transfer, and bare Na^+ or Li^+ is inserted/extracted in PBA. Most likely, less-polarizing bare Na^+ can be transferred at the interface more easily than more-polarizing Li^+, which results in larger E_a for Li^+.[16,20,21] Faster interfacial Na^+ transfer agrees with the smaller ΔE_p in the CV. Nevertheless, both E_a values for the Li^+ and Na^+ organic electrolytes are considerably high.

In contrast, E_a for the Li^+ aqueous electrolyte (25.7 kJ/mol) is much smaller than that for the Li^+ organic electrolyte (60.8 kJ/mol). Since the PBA electrode with the aqueous electrolyte is well known to show intercalation/extraction of hydrated ions,[22] the significant change in E_a suggests that bare Li^+ is not the mobile ion with the aqueous electrolyte. Hydrated Li^+ (2.37 Å) is too large to be intercalated, thus it is presumed that partial dehydration occurs during the interfacial charge transfer in order to decrease the radius of the mobile charge, and then the partially hydrated Li^+ may be inserted into PBA. The Coulombic repulsion during the interfacial charge transfer should be reduced largely by the screening effect of the hydration, which explains small E_a well.

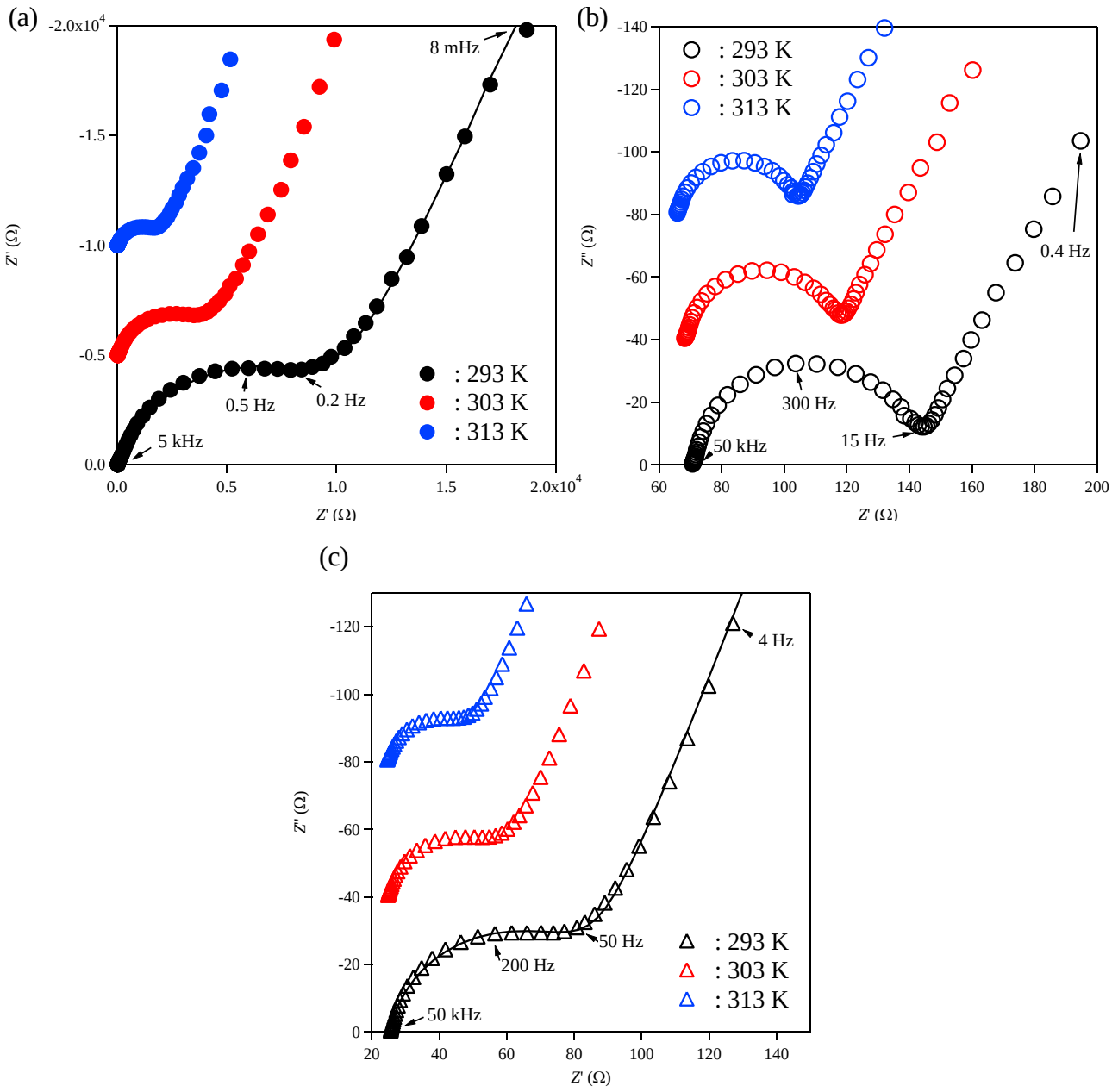

Figure 6. (a) Nyquist plots for NiFe-PBA/ITO with 1 M $LiClO_4$/PC. (b) Nyquist plots for NiFe-PBA/ITO with aqueous solution of 1 M $LiNO_3$. (c) Nyquist plots for NiFe-PBA/ITO with aqueous solution of 1 M $Mg(NO_3)_2$.

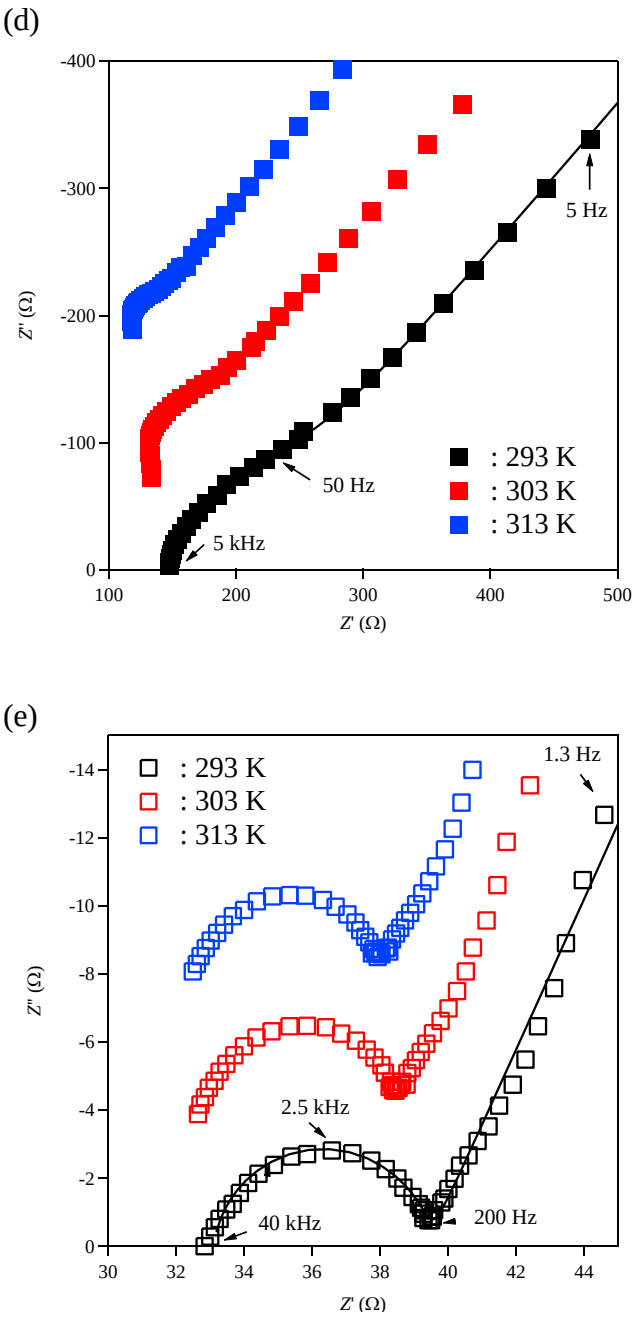

Figure 6. (d) Nyquist plots for NiFe-PBA/ITO with 1 M $NaClO_4$/PC. (e) Nyquist plots for NiFe-PBA/ITO with aqueous solution of 1 M $NaNO_3$.

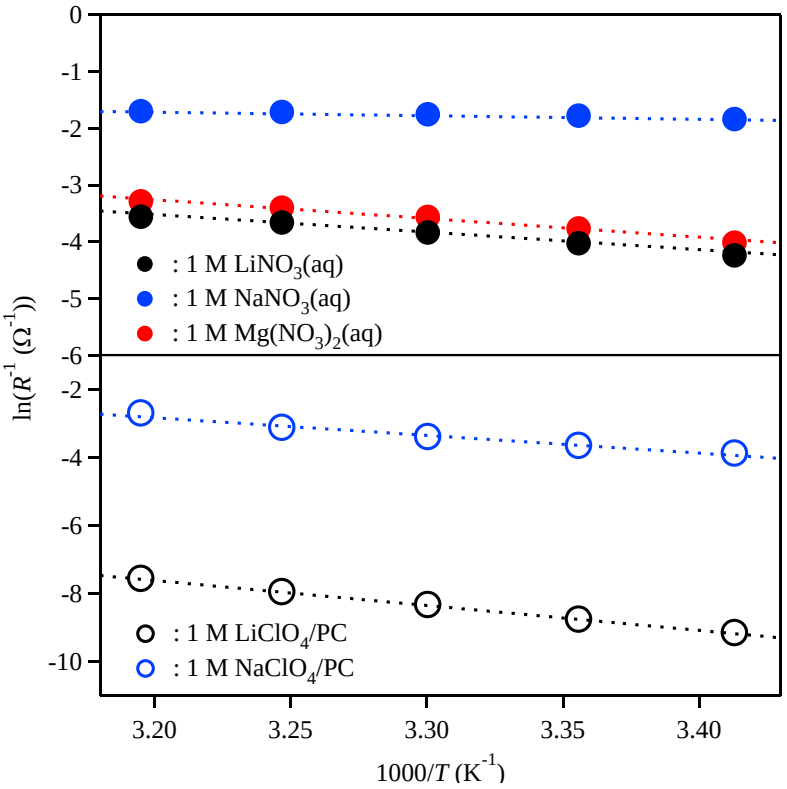

Figure 7. Plots of $\ln R^{-1}$ against $1000/T$ for NiFe-PBA/ITO. Black opened circles: 1 M $LiClO_4$/PC, E_i = 0.2 V vs. NHE, blue opened circles: 1 M $NaClO_4$/PC, E_i = 0.4 V vs. NHE, black closed circles: aqueous solution of 1 M $LiNO_3$, E_i = 0.1 V vs. NHE, blue closed circles: aqueous solution of 1 M $NaNO_3$, E_i = 0.6 V vs. NHE and red closed circles: aqueous solution of 1 M $Mg(NO_3)_2$, E_i = 0.5 V vs. NHE.

Table 1. Activation energy E_a for interfacial charge transfer between NiFe-PBA/ITO and various electrolytes.

electrolyte		E_a (kJ/mol)
organic	1 M $LiClO_4$/PC	60.8(4)
	1 M $NaClO_4$/PC	43(3)
	1 M $Mg(ClO_4)_2$/PC	No charge transfer
aqueous	1 M $LiNO_3$(aq)	25.7(8)
	1 M $NaNO_3$(aq)	5.2(5)
	1 M $Mg(NO_3)_2$(aq)	27(1)

The hydration effect on the interfacial charge transfer is more significant for Na^+. E_a for the Na^+ aqueous electrolyte (5.2 kJ/mol) is negligibly small compared to that for the Na^+ organic electrolyte (43 kJ/mol). The radius of hydrated Na^+ (1.83 Å) is almost same as the intercell bottleneck radius of PBA. Therefore, the interfacial charge transfer may not involve the dehydration process, and almost fully hydrated Na^+ may be transferred. The full hydration of Na^+ should largely suppress the Coulombic repulsion, thus E_a for the interfacial charge transfer. The negligibly small E_a at the electrode-electrolyte interface can contribute to the fast interfacial Na^+ transfer. Furthermore, the hydration of Na^+ can also suppress the Coulombic repulsion during bulk diffusion within the PBA framework, which results in fast Na^+ diffusion. The fast reaction kinetics due to the hydration well explains ΔE_p of 0 mV in the CV. Therefore, although various other factors such as ionic conductivity of the electrolyte or electronic conductivity of the composite electrode affect the rate capability of the batteries, fast Na^+ diffusion/interfacial transfer with the aqueous electrolytes should be one of the origins for the high power output of the aqueous batteries with the PBA electrodes.

The hydration effect is also observed for Mg^{2+}. PBA/ITO with the Mg^{2+} organic electrolyte was a blocking electrode. As discussed above, PC molecule is too large to be co-intercalated in PBA, thus all the solvated PC should be desolvated completely during the interfacial charge transfer. However, bare Mg^{2+} should have large Coulombic repulsion at the interface, which results in the blocking behavior. On the other hand, PBA/ITO with the Mg^{2+} aqueous electrolyte showed clear intercalation/extraction of Mg^{2+}. E_a for the Mg^{2+} aqueous electrolyte (27 kJ/mol) is comparable to that for the Li^+ electrolyte. Hydrated Mg^{2+} (2.1 Å) may be dehydrated partially during the interfacial charge transfer. The Coulombic repulsion at the interface should be decreased by the partial hydration of Mg^{2+}, which enables the intercalation in PBA.

3.4. Conclusions

The hydration effect on the activation energy for the NiFe-PBA thin film electrode-electrolyte interfacial charge transfer was clarified by the temperature dependent EIS. E_a for the interfacial Li^+ transfer is decreased from 60.8 kJ/mol (PC) to 25.7 kJ/mol (H_2O), because the screening effect of hydration may suppress the Coulombic repulsion at the interface. The hydration effect was more significant for Na^+. E_a for the interfacial Na^+ transfer was largely decreased from 43 kJ/mol (PC) to 5.2 kJ/mol (H_2O). The negligibly small E_a with the aqueous Na^+ electrolyte should be one of the origins for the high power output of the aqueous batteries with the PBA electrodes. Furthermore, the hydration effect enabled the Mg^{2+} intercalation in PBA.

References

(3-1) Dunn, B.; Kamath, H.; Tarascon, J. M. *Science* **2011**, *334*, 928-935.

(3-2) Yang, Z.; Zhang, J.; Kintner-Meyer, M. C. W.; Lu, X.; Choi, D.; Lemmon, J. P.; Liu, J. *Chem. Rev*. **2011**, *111*, 3577-3613.

(3-3) Imanishi, N.; Morikawa, T.; Kondo, J.; Takeda, Y.; Yamamoto, O.; Kinugasa, N.; Yamagishi, T. *J. Power Sources* **1999**, *79*, 215-219.

(3-4) Okubo, M.; Asakura, D.; Mizuno, Y.; Kim, J.-D.; Mizokawa, T.; Kudo, T.; Honma, I.; *J. Phys. Chem. Lett.* **2010**, *1*, 2063-2071.

(3-5) Okubo, M.; Asakura, D.; Mizuno, Y.; Kudo, T.; Zhou, H.; Okazawa, A.; Kojima, N.; Ikedo, K.; Mizokawa, T.; Honma, I. *Angew. Chem. Int. Ed*. **2011**, *50*, 6269-6274.

(3-6) Mizuno, Y.; Okubo, M.; Asakura, D.; Saito, T.; Hosono, E.; Saito, Y.; Oh-ishi, K.; Kudo, T.; Zhou, H. *Electrochim. Acta* **2012**, *63*, 139-145.

(3-7) Asakura, D.; Okubo, M.; Mizuno, Y.; Kudo, T.; Zhou, H.; Ikedo, K.; Mizokawa, T.; Okazawa, A.; Kojima, N. *J. Phys. Chem. C* **2012**, *116*, 8364-8369.

(3-8) Itaya, K.; Ataka, T.; Toshima, S. *J. Am. Chem. Soc*. **1982**, *104*, 4767-4772.

(3-9) Itaya, K.; Uchida, I.; Neef, V. D. *Acc. Chem. Res.* **1986**, *19*, 162-168.

(3-10) Wessells, C. D.; Huggins, R. A.; Cui, Y. *Nat. Commun*. **2011**, *2*, 550.

(3-11) Wessells, C. D.; Peddada, S. V.; Huggins, R. A.; Cui, Y. *Nano Lett.* **2011**, *11*, 5421-5425.

(3-12) Wessells, C. D.; Peddada, S. V.; McDowell, M. T.; Huggins, R. A.; Cui, Y. *J. Electrochem. Soc.* **2012**, *159*, A98-A103.

(3-13) Wessells, C. D.; McDowell, M. T.; Peddada, S. V.; Pasta, M.; Huggins, R. A.; Cui, Y. *ACSnano* **2012**, *6*, 1688-1694.

(3-14) Pajerowski, D. M.; Gardner, J. E.; Frye, F. A.; Andrus, M. J.; Dumont, M. F.; Knowles, E. S.; Meisel, M. W.; Talham, D. R. *Chem. Mater.* **2011**, *23*, 3045-3053.

(3-15) Kulesza, P. J.; Doblhofer, K. *J. Electroanal. Chem.* **1989**, *274*, 95-105.

(3-16) Gao, Z.; Bobacka, J.; Ivaska, A. *Electrochim. Acta* **1993**, *38*, 379-385.

(3-17) Chen, S.-M.; Chan, C.-M. *J. Electroanal. Chem.* **2003**, *543*, 161-173.

(3-18) Barsoukov, E.; Macdonald, J. R. *Impedance Spectroscopy*; John Wiley & Sons, Inc.: Hoboken, New Jersey, 2005.

(3-19) Ho, C.; Raistrick, I. D.; Huggins, R. A. *J. Electrochem. Soc*. **1980**, *127*, 343-350.

(3-20) Malev, V.; Kurdakova, V.; Kondratiev, V.; Zigel, V. *Solid State Ionics* **2004**, *169*, 95-104.

(3-21) Malik, M. A.; Kulesza, P. J.; Marassi, R.; Nobili, F.; Miecznikowsli, K.; Zamponi, S. *Electrochim. Acta* **2004**, *49*, 4253-4258.

(3-22) García-Jareño, J. J.; Sanmatías, A.; Vicente, F.; Gabrielli, C.; Keddam, M.; Perrot, H. *Electrochem. Acta* **2000**, *45*, 3765-3776.

Chapter 4

Magnesium Ion Intercalation in Cyanide-Coordinated Porous Polymer

4.1. Introduction

Rechargeable batteries have been focused on their contribution to the energy saving because they can be applied to portable electric devises, advanced vehicles, and grid-scale energy storage.[1-3] In order to realize the rechargeable batteries, the ion intercalation reactions in the insertion compounds are the fundamental issues because they enable the compounds to apply to electrode materials for rechargeable batteries. In particular, Li^+ intercalation in the compound has been investigated widely for application to Li-ion battery because it shows high energy density.[4-7]

On the other hand, alternative rechargeable batteries which can substitute the Li-ion battery have been required according to reserve exhaustion and high cost of lithium. Among them, Mg-ion battery is the one of most promising batteries because magnesium has larger reserves and lower cost than lithium.[8-11] In addition, the ionic radius of Mg^{2+} (0.65 Å) is similar to that of Li^+ (0.60 Å), thus Mg^{2+} intercalation in the insertion compound could be able to achieve. However, the Mg^{2+} intercalation has hardly been reported because Mg^{2+} is a divalent ion, thus the large repulsion between Mg^{2+} and the compound suffer the Mg^{2+} intercalation. Therefore, it is necessary to suppress the large repulsion for achieving the Mg^{2+} intercalation.

In order to achieve Mg^{2+} intercalation, using aqueous electrolyte would be effective way because ion intercalates into the compound with hydrated state. Therefore, the hydrated shell around ion suppresses the repulsion, and enables Mg^{2+} insertion/extraction.

Prussian blue analog, $A_xM[M'(CN)_6]_{1-y}\cdot\square_y\cdot nH_2O$ (A: alkali metal, M, M': transition metal, □: $[M'(CN)_6]$ defect, hereafter denoted MM'-PBA), has both electronic- and ionic-conductivities due to cyanide-bridged porous structure, and transition metal redox-active site. Therefore PBA can be inserted/extracted various ions such as alkali-metal ions with both organic and aqueous electrolyte.[12-23] In particular, PBA shows faster ionic diffusion with aqueous electrolyte than that with organic

electrolyte due to the hydrated structure. Therefore, Mg^{2+} could insert/extract into PBA with aqueous electrolyte. In this report, the Mg^{2+} intercalation in PBA was investigated with aqueous electrolyte.

4.2. Experimental Methods

CuFe-PBA was prepared by a precipitation method. An aqueous solution of 0.15 M $CuSO_4 \cdot 5H_2O$ was added dropwise to an aqueous solution of 0.1 M $K_3Fe(CN)_6$. The precipitate was centrifuged, washed with distilled water, and then dried in vacuo for 24 h. The obtained product was stored under an inert atmosphere in the dark at 5 ºC to prevent decomposition.

The composition was determined by the standard micro-analytical method for C, H and N elements and the coupled plasma mass spectroscopy for K, Fe and Ni elements. Calcd. for $K_{0.1}Cu[Fe(CN)_6]_{0.7} \cdot 3.6H_2O$: K, 1.39; Cu, 22.6; Fe, 13.9; C, 17.97; N, 20.96 and H, 2.59. Found: K, 1.48; Cu, 21.9; Fe, 13.4; C, 18.20; N, 19.86 and H, 2.62.

Powder X-ray diffraction (XRD) measurement was carried out on a Bruker D8 Advance using Cu $K\alpha$ radiation in steps of 0.01˚ over the 2θ range of 5 – 80˚. The unit cell parameters were calculated by the least square fitting with peak top values. SEM measurement was carried out on a Carl Zeiss Supra 35.

For the electrochemical measurements, three electrode glass cells were used. CuFe-PBA was mixed homogeneously with 20 wt % acetylene black and 10 wt % polyvinylidene fluoride (PVdF) in *N*-methyl-2-pyrrolidone (NMP) by using a sono-horn. The resulting slurry was cast on a carbon paper and dried in vacuo for 12 h. For the reference electrode, an Ag/AgCl in 3 M NaCl was used. For the electrolyte, aqueous solutions of 1 M $Mg(NO_3)_2$ were used. For the counter electrode, the pretreated CuFe-PBA electrode was used. First, in order to extract the small amount of K ion, the PBA electrode was charged to the 1.0 V by galvanostatic intermittent titration technique (GITT), and then the electrode was discharged to the half-discharge potential by GITT to insert small amount of Mg ion in flesh cell. For the Mg-ion insertion/extraction, we used a galvanostat (SD-8, Hokuto Denko), and the cut-off voltages were 0.1 V and 1.0 V (vs. Ag/AgCl). The cyclic voltammogram was recorded on VersaSTAT. The open-circuit voltages (OCVs) were measured by repeats of flowing galvanostatic current (current

density; 18 mA/g) for 10 minutes and the potential relaxation for 30 minutes under an open-circuit state.

4.3. Results and Discussion

CuFe-PBA was synthesized by a precipitation method. Figure 1 shows the powder X-ray diffraction pattern for CuFe-PBA. The XRD pattern indicated a single cubic phase without crystalline impurity. The estimated unit cell parameters were a = 10.1274(5) Å and V = 1038.7(1) Å^3. These values are well consistent to the previous reported values. The mean particle size for CuFe-PBA estimated from SEM image was about 50 nm (figure 1(b)).

Electrochemical Mg^{2+} intercalation reaction was carried out for CuFe-PBA in the aqueous solution of 1 M $Mg(NO_3)_2$. An Ag/AgCl electrode was used as the reference electrode, and the CuFe-PBA containing small amount of Mg^{2+} was used as the counter electrode. Figure 2(a) shows the cyclic voltammogram (CV) at the scan rate of 5 mV·s^{-1} (solid line). CuFe-PBA showed a strong cathodic at 0.57 V and an anodic peaks at 0.65 V. According to the previous reports, these peaks could be ascribed to the solid-state redox of $[Fe^{3+}(CN)_6]/[Fe^{2+}(CN)_6]$ couple in CuFe-PBA.[24] In addition, two weak redox peaks were observed at around 0.25 V and 0.85 V. It was reported that the further one would correspond to the Cu^{2+}/Cu^{+} redox couple in CuFe-PBA.[24] However, the nature of the later one has not been understood yet. The CV measurement for the electrode which did not contain CuFe-PBA (only contained AB and PVdF) was also carried out, and that did not show any faradaic reaction (dotted line). Therefore, the later one might correspond to some kind of side reaction of CuFe-PBA.

Figure 2(b) shows the open-circuit voltages (OCVs) for CuFe-PBA. CuFe-PBA showed the reversible discharge-charge capacities of 60 mAh/g at the potential ranging from 0.9 and 0.2 V. The observed potential well agreed with the redox peaks recorded in the CV.

(a)

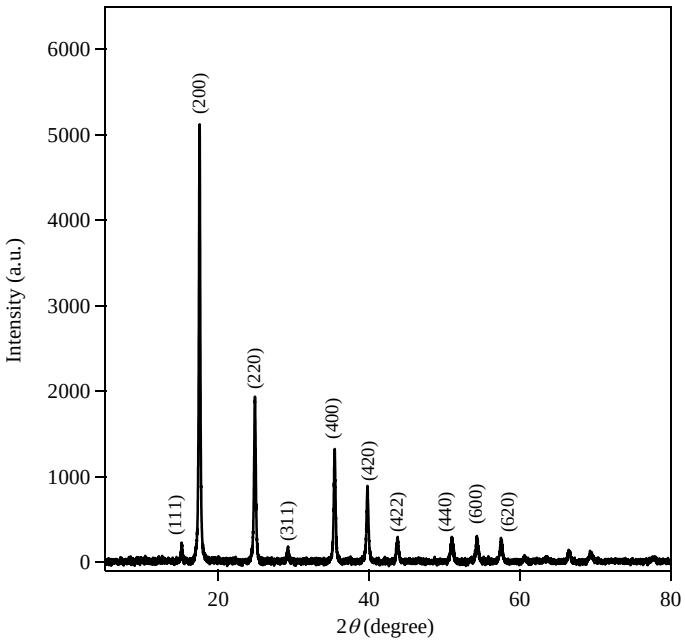

(b)

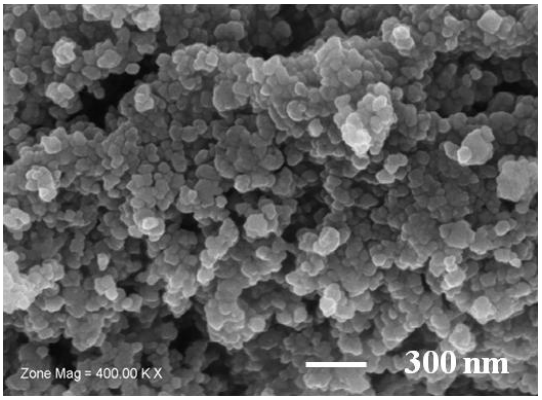

Figure 1. (a) Powder XRD pattern for CuFe-PBA. (b) SEM image for CuFe-PBA.

(a)

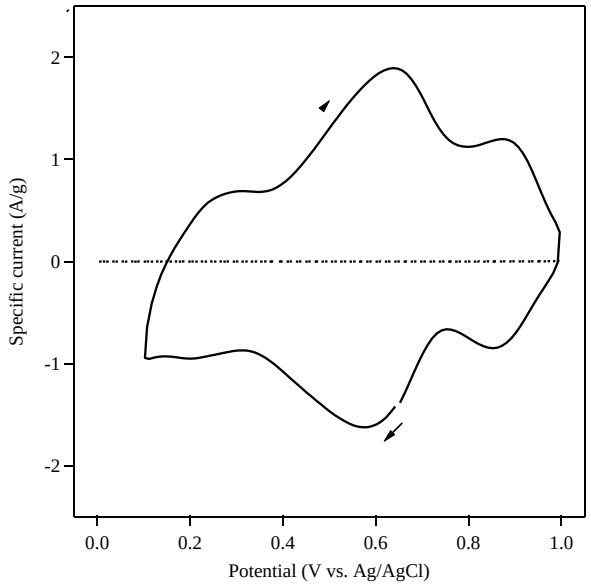

(b)

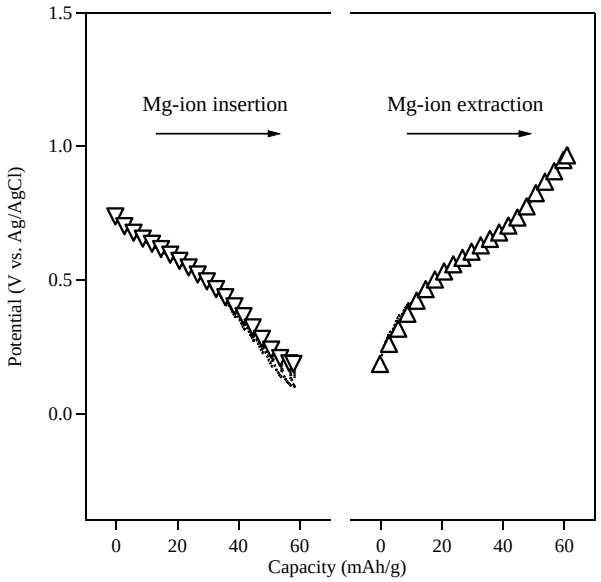

Figure 2. (a) Cyclic voltammograms for CuFe-PBA (solid line) and AB + PTFE (dashed line). The scan rate is 5 mV/s. (b) Open-circuit voltages (OCVs) for Mg_x(CuFe-PBA) during Mg-ion insertion/extraction.

In order to confirm the structural change during charge-discharge reaction, the ex-situ XRD measurement for CuFe-PBA was carried out (Figure 3). During charge-discharge, all of the peaks shifted gradually without emergence of an additional peak, suggesting that the Mg^{2+} intercalation/extraction proceeded *via* a solid solution process. The change in the lattice constant during charge-discharge reaction is plotted in Figure 6 (closed triangles). CuFe-PBA framework resulted in a slight shrinkage of the lattice constant from 10.104 Å (as-prepared) to 9.998 Å (full-discharged state) during discharge reaction and a slight expansion of that from 9.998 Å (full-discharged state) to 10.077 Å (full-charged state) during charge reaction.

The reversible charge-discharge capacities and the slight shrinkage/expansion of CuFe-PBA during charge-discharge reaction indicate that CuFe-PBA would intercalate/extract Mg^{2+}. In order to confirm whether Mg^{2+} was intercalated/extracted into CuFe-PBA, the inductively coupled plasma mass spectroscopy (ICP-MS) for Mg was carried out during charge-discharge reaction. Closed circles in Figure 6 show the amount of intercalated/extracted Mg^{2+} *x*. CuFe-PBA can intercalate 0.21 Mg^{2+} and extract 0.25 Mg^{2+}. These results indicated that the CuFe-PBA can intercalated/extracted Mg^{2+}.

In order to clarify the change in the electronic structure, ^{57}Fe Mössbauer spectra were recorded for CuFe-PBA during Mg^{2+} intercalation/extraction (Figure 4). The black dots in Figure 3b are experimental data and broken lines are fitted curves. All of the spectra could be fitted successfully using a combination of a low-spin Fe^{3+} doublet and a low-spin Fe^{2+} singlet (Figure 4 and Table 1). Before discharge reaction, all of Fe in CuFe-PBA could be characterized as the low-spin Fe^{3+}. At the full-discharged state, 69 % of Fe^{3+} was reduced to Fe^{2+}, while Fe^{2+} was completely oxidized to Fe^{3+} at the full-charged state. The change in the Fe^{3+} fraction for CuFe-PBA during charge-discharge reaction is also plotted in Figure 6 (opened circles).

In addition, the Cu *K*-edge XANES spectra during Mg^{2+} intercalation/extraction (Figure 5) was carried out. After discharge reaction, a small peak at around 8982 eV appeared in the spectrum at the full-discharged state. On the other hand, this peak completely disappeared in the spectrum at the full-charged state. According to the literature, this peak is characteristic for Cu^{+}, thus Cu^{2+} in CuFe-PBA

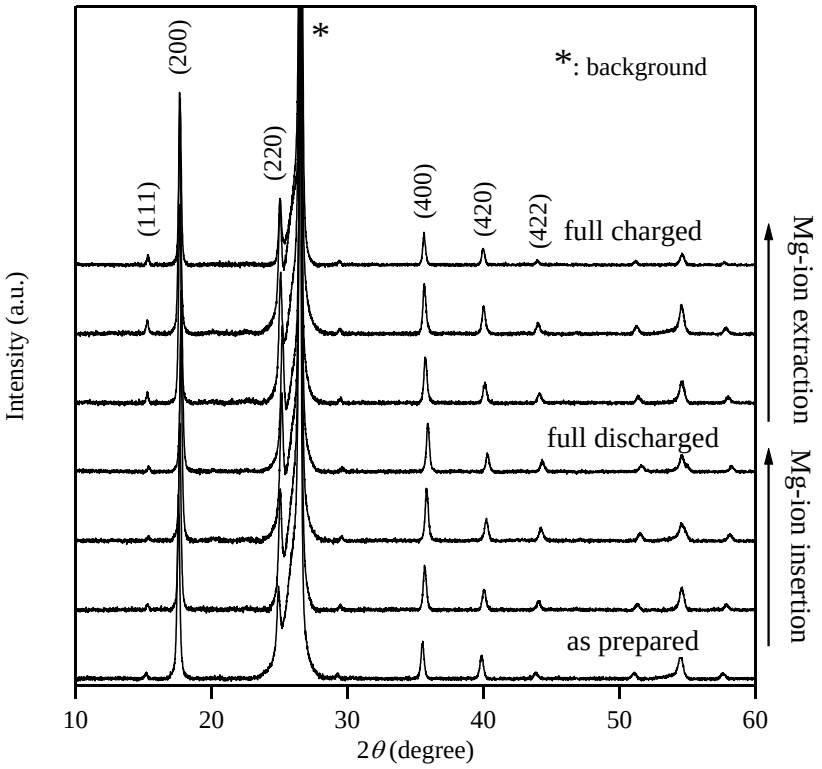

Figure 3. Ex-situ XRD patterns for CuFe-PBA during Mg-ion insertion/extraction.

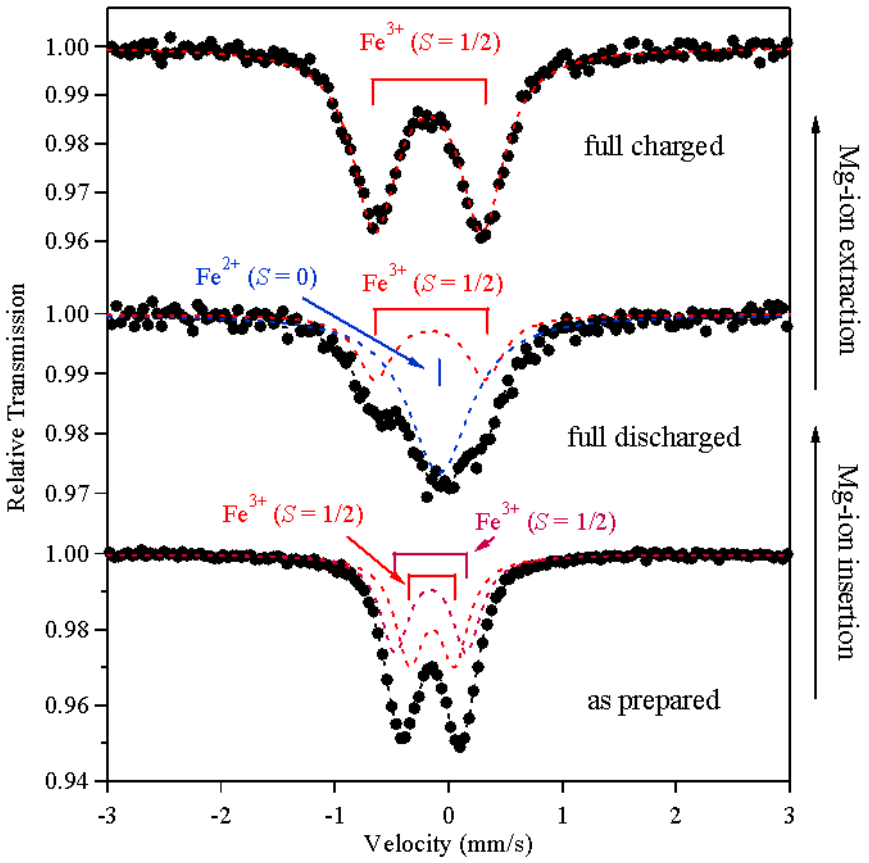

Figure 3. (b) ^{57}Fe Mössbauer spectra for CuFe-PBA during Mg-ion insertion/extraction.

Table 1. ^{57}Fe Mössbauer parameters for CuFe-PBA during Mg-ion insertion/extraction.

sample	state	IS (mm/s)	QS (mm/s)	Fraction(%)
as prepared	Fe^{3+} (S = 1/2)	-0.15	0.39	52
	Fe^{3+} (S = 1/2)	-0.16	0.63	48
full discharged	Fe^{2+} (S = 0)	-0.06	0	69
	Fe^{3+} (S = 1/2)	-0.17	0.97	31
full charged	Fe^{3+} (S = 1/2)	-0.18	0.94	100

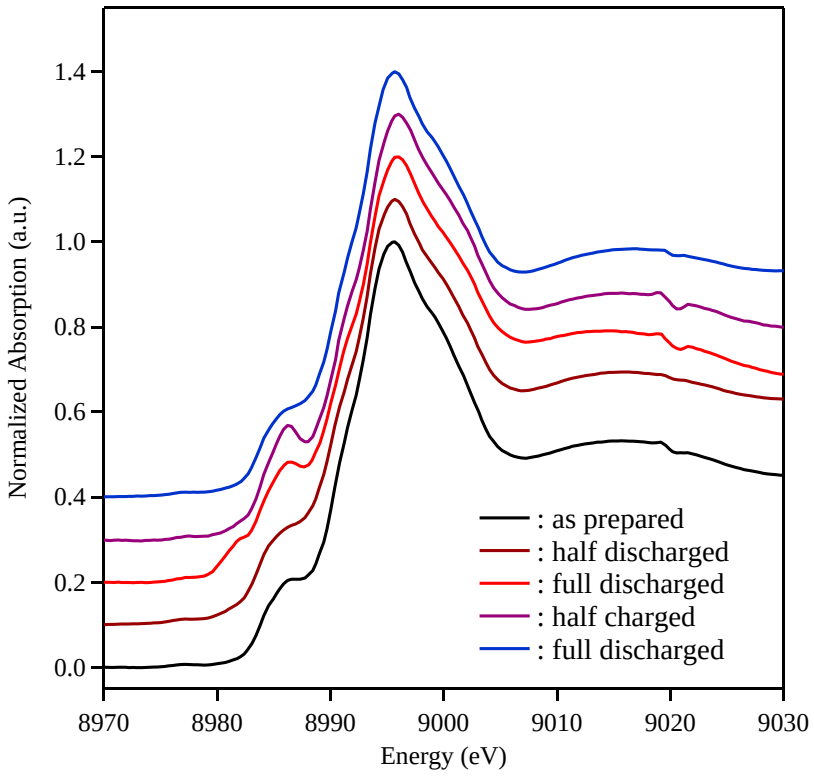

Figure 5. Cu *K*-edge XANES spectra for CuFe-PBA during Mg-ion insertion/extraction.

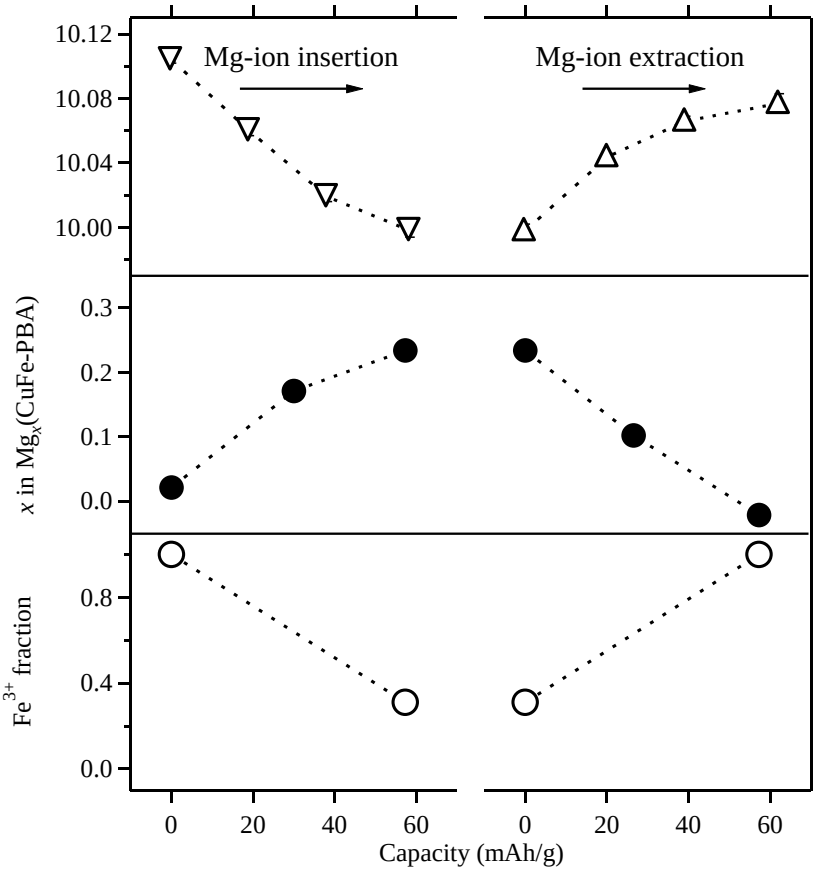

Figure 6. Lattice constant (closed triangles), Fe^{3+} fraction (opened circles) and x in Mg_x(CuFe-PBA) (closed circles) against charge-discharge capacity.

may be reduced to Cu^{+} during discharge reaction, and Cu^{+} may be oxidized to Cu^{2+} during charge reaction.[25] These spectral changes agree well with the redox peak of Cu^{2+}/Cu^{+} in the CV (Figure 2(a)).The electrode property of CuFe-PBA was tested at the constant current densities of 50 and 200 mA/g, respectively. Figure 7(a) shows the charge-discharge curves at 1st cycle. CuFe-PBA shows reversible charge-discharge capacities at both current densities of 50 (66 mAh/g) and 200 mAh/g (64 mAh/g).

Figure 7(b) shows the cyclabilities for CuFe-PBA at the current densities of 50 (black opened triangles) and 200 (red opened triangles) mAh/g. After 100 charge/discharge cycles, the discharge capacity decreases from 66 to 33 mAh/g (50 % loss) at 50 mA/g, while that decreases from 64 to 38 mAh/g (41 % loss) at 200 mA/g.

To confirm the capacity fading, the ex-situ XRD patterns before and after 100 charge/discharge cycles (Figure. 7). After 100 charge/discharge cycles, the cubic phase maintains, and there is no other Bragg reflections indexed as other phase. Therefore, cyanide-bridged structure of CuFe-PBA does not broken during Mg^{2+} intercalation/extraction. However, after the charge-discharge measurement, the electrolyte turns yellow during repeating Mg^{2+} intercalation/extraction. Similar behavior reported in case of Li^{+} intercalation/extraction into CuFe-PBA and NiFe-PBA with the aqueous solutions. This result would indicate that the Mg^{2+} intercalated CuFe-PBA dissolute into the electrolyte.

Figure 8 showed the charge-discharge curves for CuFe-PBA at the various current densities from 50 mA/g (0.75 C rate) to 5 A/g (75 C rate) (solid lines). The discharge capacity decreases from 59 mAh/g at 50 mA/g to 29 mAh/g at 5 A/g (51 % loss) (opened triangles). On the other hand, it was reported that the discharge capacity decreases from 60 mAh/g at 50 mA/g to 40 mAh/g at 5 A/g (33 % loss) in case of Li^{+} intercalation/extraction and that from 61 mAh/g at 50 mA/g to 50 mAh/g at 5 A/g (18 % loss) in case of Na^{+} intercalation/extraction, thus the rate-capabilities of these ions are better than that of Mg^{2+}. Although various other factors such as ionic diffusion in the bulk electrode, ionic conductivity of the electrolyte or electronic conductivity of the composite electrode affect the rate capability of the batteries, small activation energy for interfacial ion transfer E_a should be one of the origins for the high

rate-capabilities. In chapter 3, interfacial ion transfer between NiFe-PBA thin film electrode and aqueous electrolytes was investigated, and reported that E_a for Mg^{2+} (27 kJ/mol) transfer is higher than these for Li^+ (25.7 kJ/mol) and Na^+ (5.2 kJ/mol).[9] Therefore, the lower rate-capabilities for Mg^{2+} would correspond to higher E_a.

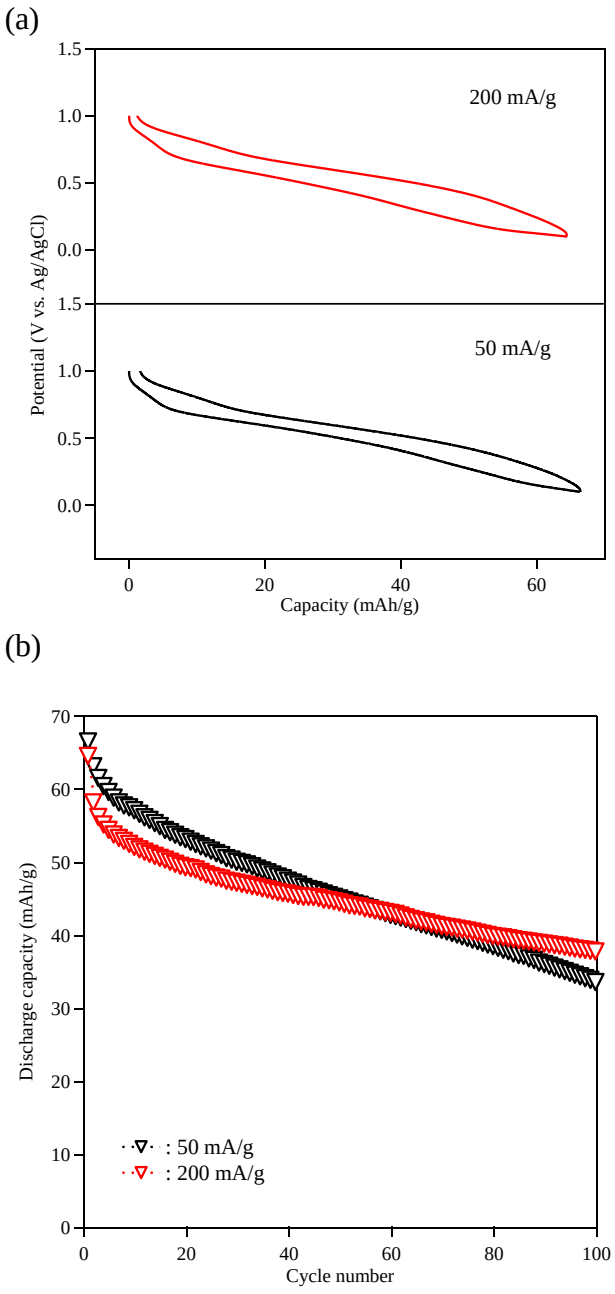

Figure 6. (a) Charge-discharge curves for CuFe-PBA at 1st cycle. The current densities are 50 and 200 mA/g. (b) Cyclability for CuFe-PBA. The current densities are 50 (black opened circles) and 200 mA/g (red opened circles).

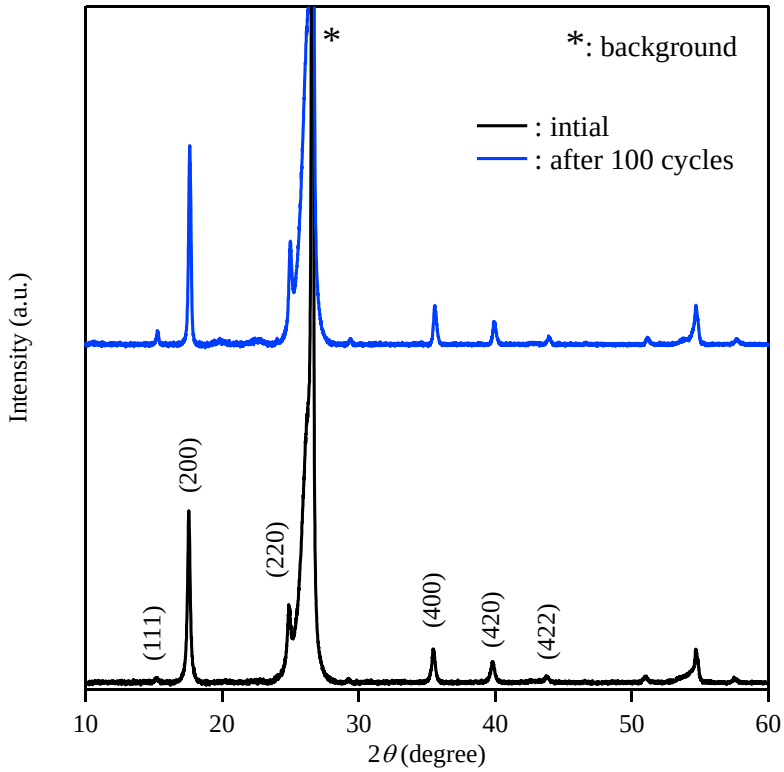

Figure 7. Ex-situ XRD patterns for CuFe-PBA before and after 100 cycles.

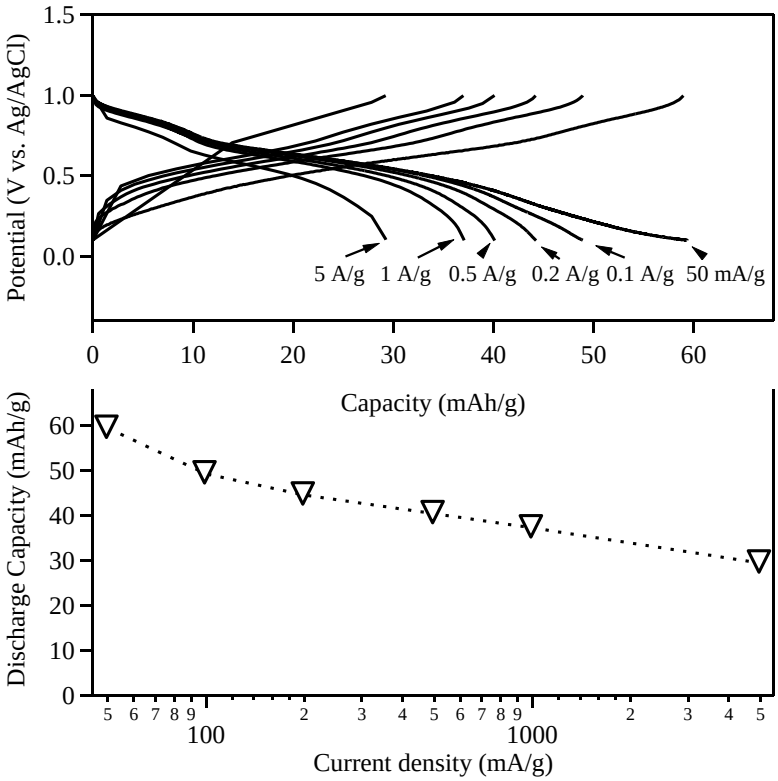

Figure 8. Charge-discharge curves and rate-capability for CuFe-PBA. The current densities are 50 mA/g, 0.1 A/g, 0.2 A/g, 0.5 A/g, 1 A/g and 5 A/g.

4.4. Conclusions

Mg^{2+} intercalation/extraction reaction of CuFe-PBA was investigated with aqueous electrolyte. CuFe-PBA showed reversible charge-discharge capacities and slight shrinkage/expansion correspond to Mg^{2+} intercalation/extraction reaction. The ^{57}Fe Mössbauer and Cu *K*-edge XANES spectra showed reversible solid state redox of $[Fe^{3+}(CN)_6]^{3-}/[Fe^{2+}(CN)_6]^{4-}$ and Cu^{2+}/Cu^{+} reduction/oxidation during Mg^{2+} intercalation/extraction. In charge-discharge measurement, CuFe-PBA showed capacity fading during long cycle due to the dissolution. The rate-capability for Mg^{2+} was lower than these for Li^{+} and Na^{+} due to large E_a.

References

(4-1) Armand, M.; Tarascon, J. M. *Nature* **2008**, *451*, 652-567.

(4-2) Dunn, B.; Kamath, H.; Tarascon, J. M. *Science* **2011**, *334*, 928-935.

(4-3) Yang, Z.; Zhang, J.; Kintner-Meyer, M. C. W.; Lu, X.; Choi, D.; Lemmona, J. P.; Liu, J. *Chem. Rev*. **2011**, *111*, 3577-3613.

(4-4) Winter, M.; Besenhard, J. O.; Spahr, M. E.; Novák, P. *Adv. Mater.* **1998**, *10*, 725-763.

(4-5) Tarascon, J. M.; Armand, M. *Nature* **2001**, *414*, 359-367.

(4-6) Whittingham, M. S. *Chem. Rev.* **2004**, 104, 4271-4301.

(4-7) Bruce, P. G.; Scrosati, B.; Tarascon, J. M. *Angew. Chem. Int. Ed.* **2008**, 47, 2930-2646.

(4-8) Aurbach, D.; Lu, Z.; Schechter, A.; Gofer, H.; Turgeman, R.; Cohen, Y.; Moshkovich, M.; Levi, E. *Nature* **2000**, *407*, 724-727.

(4-9) Aurbach, D.; Suresh, G. S.; Levi, E.; Mitelman, A.; Mizrahi, O.; Chusid, O.; Brunelli, M. *Adv. Mater*. **2007**, *19*, 4260-.

(4-10) Mizrahi, O.; Amir, N.; Pollak, E.; Chusid, O.; Marks, V.; Gottlieb, H.; Larush, L.; Zinigrad, E.; Aurbach, D. *J. Electrochem. Soc*. **2008**, *155*, A103-A109.

(4-11) Levi, E.; Gofer, Y.; Aurbach, D. *Chem. Mater*. **2010**, *22*, 860-868.

(4-12) Imanishi, N.; Morikawa, T.; Kondo, J.; Takeda, Y.; Yamamoto, O.; Kinugasa, N.; Yamagishi, T. *J. Power Sources* **1999**, *79*, 215-219.

(4-13) Okubo, M.; Asakura, D.; Mizuno, Y.; Kim, J.-D.; Mizokawa, T.; Kudo, T.; Honma, I.; *J. Phys. Chem. Lett.* **2010**, *1*, 2063-2071.

(4-14) Okubo, M.; Asakura, D.; Mizuno, Y.; Kudo, T.; Zhou, H.; Okazawa, A.; Kojima, N.; Ikedo, K.; Mizokawa, T.; Honma, I. *Angew. Chem. Int. Ed*. **2011**, *50*, 6269-6274.

(4-15) Asakura, D.; Okubo, M.; Mizuno, Y.; Kudo, T.; Zhou, H.; Amemiya, K.; de Groot, F. M. F.; Chen, J.-L.; Wang, W.-C.; Glans, P.-A.; Chang, C.; Guo, J.; Honma, I. *Phys. Rev. B* **2011**, *84*, 045117.

(4-16) Mizuno, Y.; Okubo, M.; Asakura, D.; Saito, T.; Hosono, E.; Saito, Y.; Oh-ishi, K.; Kudo, T.; Zhou, H. *Electrochim. Acta* **2012**, *63*, 139-145.

(4-17) Mizuno, Y.; Okubo, M.; Kagesawa, K.; Asakura, D.; Kudo, T.; Zhou, H.; Oh-ishi, K.; Okazawa, A.; Kojima, N. *Inorg. Chem.* **2012**, *51*, 10311-10316.

(4-18) Itaya, K.; Ataka, T.; Toshima, S. *J. Am. Chem. Soc*. **1982**, *104*, 4767-4772.

(4-19) Itaya, K.; Uchida, I.; Neef, V. D. *Acc. Chem. Res.* **1986**, *19*, 162-168.

(4-20) Wessells, C. D.; Huggins, R. A.; Cui, Y. *Nat. Commun*. **2011**, *2*, 550.

(4-21) Wessells, C. D.; Peddada, S. V.; Huggins, R. A.; Cui, Y. *Nano Lett.* **2011**, *11*, 5421-5425.

(4-22) Wessells, C. D.; Peddada, S. V.; McDowell, M. T.; Huggins, R. A.; Cui, Y. *J. Electrochem. Soc*.**2012**, *159*, A98-A103.

(4-23) Wessells, C. D.; McDowell, M. T.; Peddada, S. V.; Pasta, M.; Huggins, R. A.; Cui, Y. *ACSnano* **2012**, *6*, 1688-1694.

(4-24) Giorgetti, M.; Guadagnini, L.; Tonelli, D.; Minicucci, M.; Aquilanti, G. *Phys. Chem. Chem. Phys*. **2012**, *14*, 5527-5537.

(4-25) Ma, X.-D.; Yokoyama, T.; Hozumi, T.; Hashimoto, K.; Ohkoshi, S. *Phys. Rev. B* **2005**, *72*, 094107.

Chapter 5

Precise Electrochemical Control of Ferromagnetism in a Cyanide-Bridged Bimetallic Coordination Polymer

5.1. Introduction

Multifunctionality is an important concept in recent chemistry, because existence of multiple functionalities in a single phase can produce novel cooperative phenomena such as multiferroics.[1] In particular, coordination polymers possess potentially controllable electronic and structural properties; thus, they could provide a rational strategy achieving the novel multifunctionalities.[2] For example, the magnetic coordination polymers have been reported to show a wide variety of magnetic properties (*e.g.*, room temperature ferrimagnetism,[3] spin-crossover,[4,5] Haldane gap[6]). In addition, other functionalities can also be introduced by designing the structure and electronic state. The coexistence of magnetism with another functionality frequently results in magnetism controllable by the external stimuli (*e.g.*, photo-irradiation,[7-10] guest insertion,[11,12] and electric field application[13]), which can be applied to electronic switch devices. Therefore, controllable magnetism of coordination polymers has been investigated intensively.

Prussian blue analog (PBA) is one of the best studied magnetic coordination polymers.[14] The cyanide-bridged perovskite-type structure of PBA, generally is formulated as $A_{1-x}M[M'(CN)_6]_{1-y}\cdot\square_y\cdot nH_2O$ (A: alkali metal, M, M': transition metal, □: $[M'(CN)_6]$ vacancy, hereafter denoted as MM'-PBA), and possesses intriguing magnetism due to the strong σ and π donation/back-donation ability of the bridging cyanide ligand. Furthermore, the open porous structure of PBA permits the penetration of small guests, which could realize H_2 adsorption,[15] proton conduction,[16] ion exchange,[17] and ion storage.[18-23]

Recently, I and my co-workers have focused on the coexistence of magnetism and ion storage ability in PBA, and magnetism switching was achieved by electrochemical ion insertion/extraction. Bimetallic CuFe-PBA was switched reversibly between a ferromagnet and a paramagnet by galvanostatic solid

state redox of the paramagnetic Fe^{3+}/diamagnetic Fe^{2+} couple.[24] Sato *et al*. also reported the electrochemical modification of magnetism of CrCr-,[25] FeFe-,[26] and NiFe-PBAs using a potentiostatic method.[27] However, these previous studies did not achieve precise control of the magnetism due to the difficulty in the quantitative ion/electron titration. To manipulate the electronic state and magnetism of PBA more quantitatively, an advanced electrochemical titration technique is required.

Here, the precise electrochemical control of ferromagnetism of a bimetallic NiFe-PBA was investigated through use of a quantitative Li^+ titration technique, i.e., the galvanostatic intermittent titration technique (GITT). (Scheme 1)

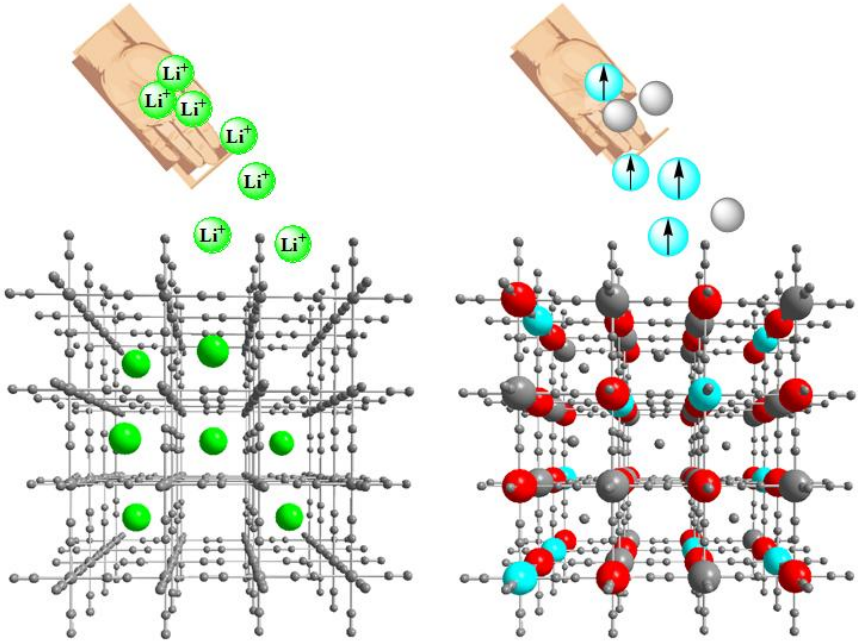

Scheme 1. Schematic illustration of Li^+/spin distributions in the coordination polymer. The Li^+ (green balls) are distributed in the porous space of the framework, while the magnetic low-spin Fe^{3+} (cyan balls) and diamagnetic low-spin Fe^{2+} (gray balls) are distributed on the host framework with the fixed magnetic Ni^{2+} (red balls).

5.2. Experimental Methods

NiFe-PBA was synthesized by a precipitation method. An aqueous solution of 0.15 M $NiCl_2 \cdot 6H_2O$ was added dropwise to an aqueous solution of 0.1 M $K_3Fe(CN)_6$. The precipitate was centrifuged, washed with distilled water, and then dried in vacuo for 24 h. The obtained products were stored under an inert atmosphere in the dark at 5 ºC to prevent decomposition.

The composition was determined by the standard micro-analytical method for C, H and N elements and the coupled plasma mass spectroscopy for K, Fe and Ni elements. Calcd. for $K_{0.2}Ni[Fe(CN)_6]_{0.7} \cdot 4.7H_2O$: K, 2.61; Ni, 19.6; Fe, 13.1; C, 16.84; N, 19.64 and H, 3.16. Found: K, 2.16; Ni, 20.1; Fe, 13.3; C, 16.60; N, 18.96 and H, 3.04.

Powder X-ray diffraction (XRD) measurement was carried out on a Bruker D8 Advance using Cu $K\alpha$ radiation in steps of 0.01° over the 2θ range of $5 - 80^\circ$. The unit cell parameters were calculated by the least square fitting with peak top values.

For the electrochemical Li^+ insertion/extraction, three electrode glass cells were used. NiFe-PBA was ground with 20 wt % acetylene black and 5 wt % poly(tetrafluoroethylene) into a paste and used as the working electrode. For the counter and reference electrode, Li metal was used. For the electrolyte, 1 M $LiClO_4$/ethylene carbonate-diethyl carbonate (EC-DEC, 1:1 V/V %) was used. The cut-off voltages were 2.0 V and 4.3 V (vs. Li/Li^+).

The direct current (DC) magnetic susceptibility was measured on a Quantum Design MPMS5S SQUID susceptometer. The magnetic susceptibility was corrected for core diamagnetism estimated from the Pascal's constants and Pauli paramagnetism because of the used acetylene black and icosane. For ^{57}Fe Mössbauer spectroscopy, ^{57}Co in Rh was used as Mössbauer source. The spectra were calibrated by using six lines of α-Fe, the center of which was taken as zero isomer shifts.

5.3. Results and Discussion

NiFe-PBA was synthesized by a precipitation method. Figure 1 shows the powder X-ray diffraction pattern for NiFe-PBA. The XRD pattern indicated a single cubic phase without crystalline impurity.

The estimated unit cell parameters were a = 10.204(3) Å and V = 1062(1) Å^3. These values are well consistent to the previous reported values (a = 10.229(5) Å).[28] The precise composition was determined as $K_{0.2}Ni[Fe^{2+}(CN)_6]_{0.1}[Fe^{3+}(CN)_6]_{0.6}\cdot\square_{0.3}\cdot 4.7H_2O$ based on the standard micro-analytical method (C, H, and N), and the coupled plasma mass spectroscopy (K, Fe, and Ni). The existence of $[Fe^{2+}(CN)_6]$ in NiFe-PBA was clearly suggested by the ^{57}Fe Mössbauer spectrum, and the amount of $[Fe^{2+}(CN)_6]$ was confirmed from the amount of electrochemically inserted Li^+ (see below).

Electrochemical Li^+ insertion/extraction reaction was conducted for NiFe-PBA. Figure 2 shows the cyclic voltammogram (CV) at a scan rate of 0.1 mV·s^{-1}. A cathodic peak was observed at 3.22 V, while an anodic peak was observed at 3.43 V. According to previous reports, these peaks could be ascribed to the Li^+ insertion and extraction, respectively, accompanied by the solid-state redox of $[Fe^{3+}(CN)_6]/[Fe^{2+}(CN)_6]$ couple in NiFe-PBA.[18-23] The electrochemical reaction of NiFe-PBA can be described as:

$$x\mathrm{Li}^+ + x\mathrm{e}^- + \mathrm{NiFe}^{3+}\text{-PBA} \leftrightarrow \mathrm{Li}_x(\mathrm{NiFe}^{2+}{}_x\mathrm{Fe}^{3+}{}_{1-x}\text{-PBA})$$

However, controlled potential methods such as CV could not determine the true equilibrium potential of the material, and performing the quantitative Li^+ titration into NiFe-PBA was also difficult. Therefore, an advanced electrochemical characterization, *i.e.*, the galvanostatic intermittent titration technique (GITT),[29] was performed. In the GITT experiment, a low-density constant current (current density; 18 mA/g) was repeatedly applied for 10 minutes, followed by interruption for 30 minutes to obtain the open circuit voltage (OCV) at each equilibrium state (Figure 3a). The open triangles in Figure 3b show the OCVs as a function of x in Li_x(NiFe-PBA). The amount of inserted/extracted Li^+ x was calculated based on Faraday's law.[30] The OCVs showed that 0.6 Li ion could be inserted/extracted reversibly ($0 < x < 0.6$ for Li_x(NiFe-PBA)) at the potential range between 3.4 and 3.2 V vs. Li/Li^+. The observed potential plateaus agreed well with the redox peaks recorded in the CV.

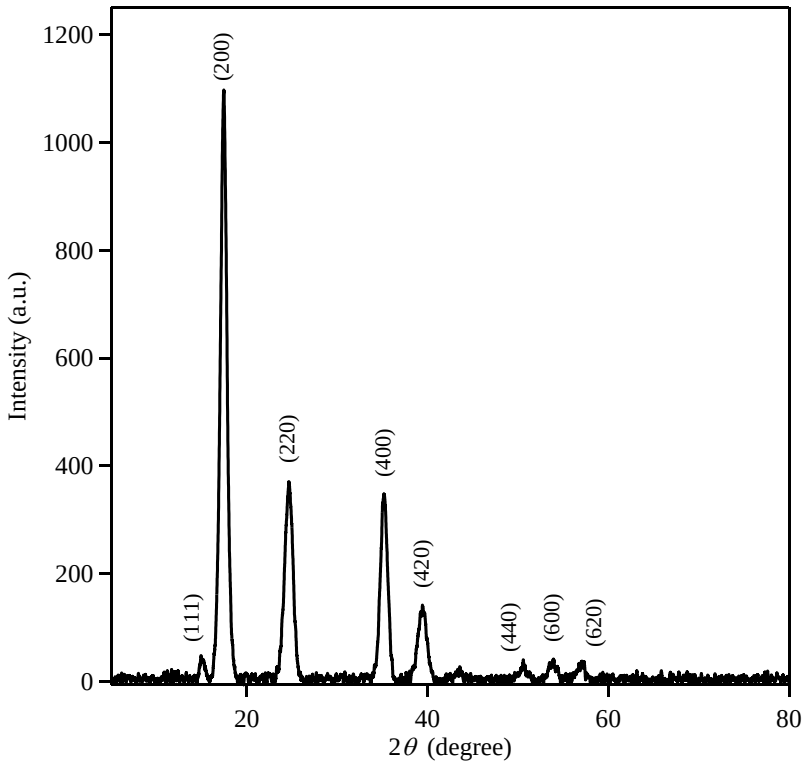

Figure 1. Powder X-ray diffraction pattern for NiFe-PBA.

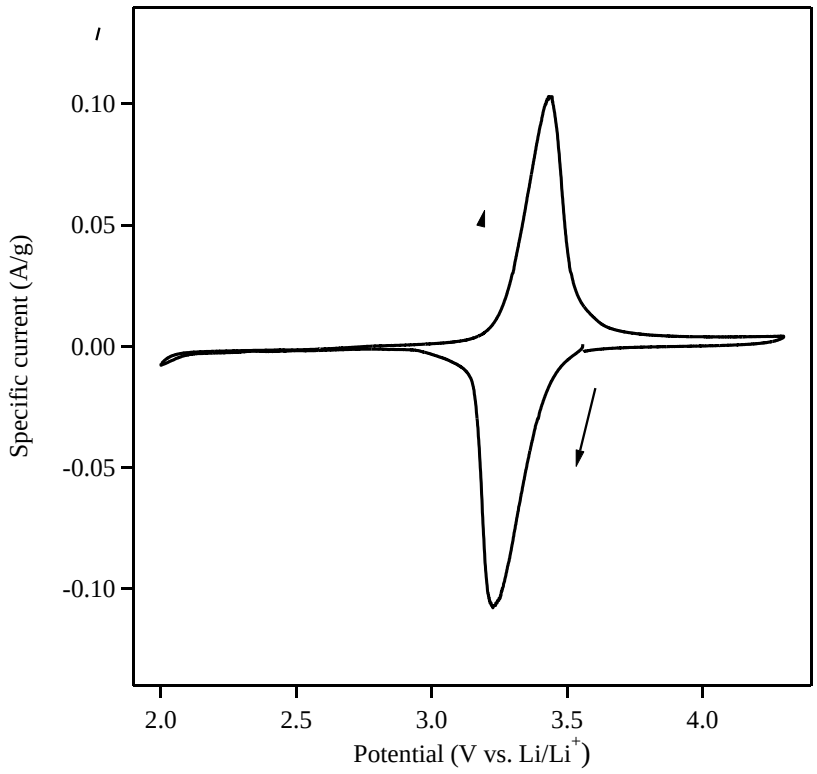

Figure 2. Cyclic voltammogram for NiFe-PBA in 1 M $LiClO_4$/EC-DEC electrolyte. Scan rate was 0.1 mV/s.

(a)

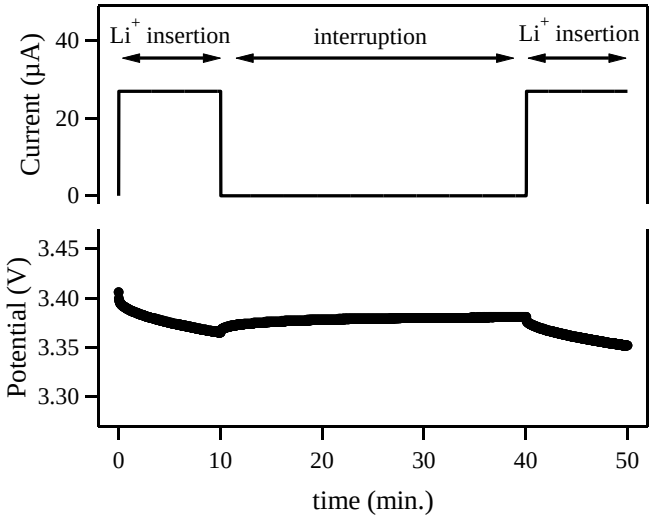

(b)

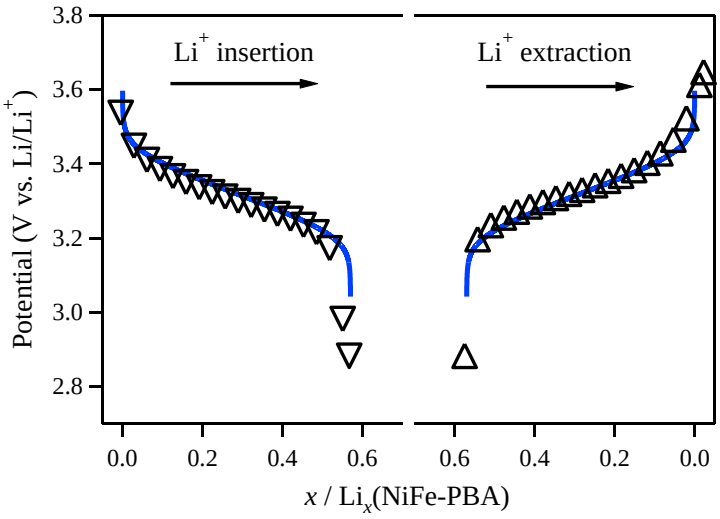

Figure 3. (a) Time dependence of potential and current during the GITT. (b) Open circuit voltage (open triangles) for Li_x(NiFe-PBA) during Li^+ insertion/extraction. Blue lines are theoretical curves based on the mean-field approximation.

The *ex-situ* XRD patterns were measured for Li_x(NiFe-PBA) ($0 < x < 0.6$) to clarify structural changes occurring during the quantitative Li^+ insertion/extraction (Figure 4). During Li^+ insertion/extraction, all of the peaks shifted gradually without emergence of an additional peak, suggesting that the Li^+ insertion proceeded *via* a solid solution process. The lattice constant is plotted as a function of x in Figure 6 (closed triangles). Li^+ insertion/extraction of the NiFe-PBA framework resulted in a slight shrinkage of the lattice constant from 10.25 Å ($x = 0$) to 10.199 Å ($x = 0.6$) and a slight expansion of that from 10.199 Å ($x = 0.6$) to 10.24 Å ($x = 0$). This result confirms the reversible lattice shrinkage/expansion during Li^+ insertion/extraction. Furthermore, the lattice constant changed linearly during Li^+ insertion/extraction, which is consistent with Vegard's law commonly observed for binary alloys.[31] Therefore, these results confirm the solid solution state of the entire composition Li_x(NiFe-PBA) ($0 < x < 0.6$).

To clarify the change in the electronic structure, ^{57}Fe Mössbauer spectra were recorded during Li^+ insertion/extraction (Figure 5). The black dots in Figure 4b are experimental data and broken lines are fitted curves. All of the spectra could be fitted successfully using a combination of a low-spin Fe^{3+} doublet and a low-spin Fe^{2+} singlet (Figure 5 and Table 1). Before Li^+ insertion, the spectrum for NiFe-PBA was fitted with a main doublet of Fe^{3+} low-spin and a small singlet of Fe^{2+} low-spin. This result supports the existence of $[Fe^{2+}(CN)_6]$ in as-prepared NiFe-PBA. During Li^+ insertion, Fe^{3+} in Li_x(NiFe-PBA) was continuously reduced to Fe^{2+}. Almost a half of Fe^{3+} was reduced to Fe^{2+} for $Li_{0.3}$(NiFe-PBA), then Fe^{3+} was completely reduced to Fe^{2+} for $Li_{0.6}$(NiFe-PBA). Fe^{2+} was gradually oxidized to Fe^{3+} during Li^+ extraction. In case of $Li_{0.3}$(NiFe-PBA) during Li-ion extraction, 40 % of Fe^{2+} was oxidized to Fe^{3+}, while Fe^{2+} was almost completely oxidized (89.4 %) to Fe^{3+} for Li_0(NiFe-PBA) after Li^+ extraction. These results confirmed that the reversible Fe^{3+}/Fe^{2+} reduction/oxidation occurred during Li^+ insertion/extraction. The Fe^{3+} fraction in Li_x(NiFe-PBA) during Li^+ insertion/extraction changed linearly as a function of x (opened circles in Figure 6). Therefore, the precise and quantitative titration of the Li ion and electron pair was achieved by GITT.

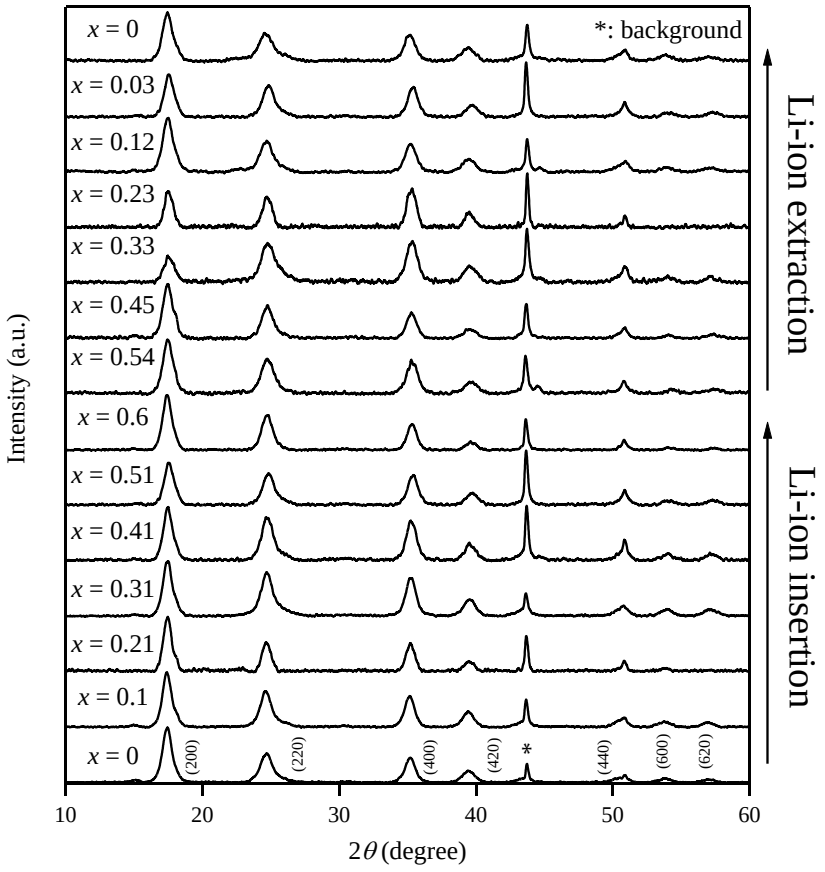

Figure 4. *Ex-situ* XRD patterns for Li_x(NiFe-PBA) during Li^+ insertion/extraction (*: background).

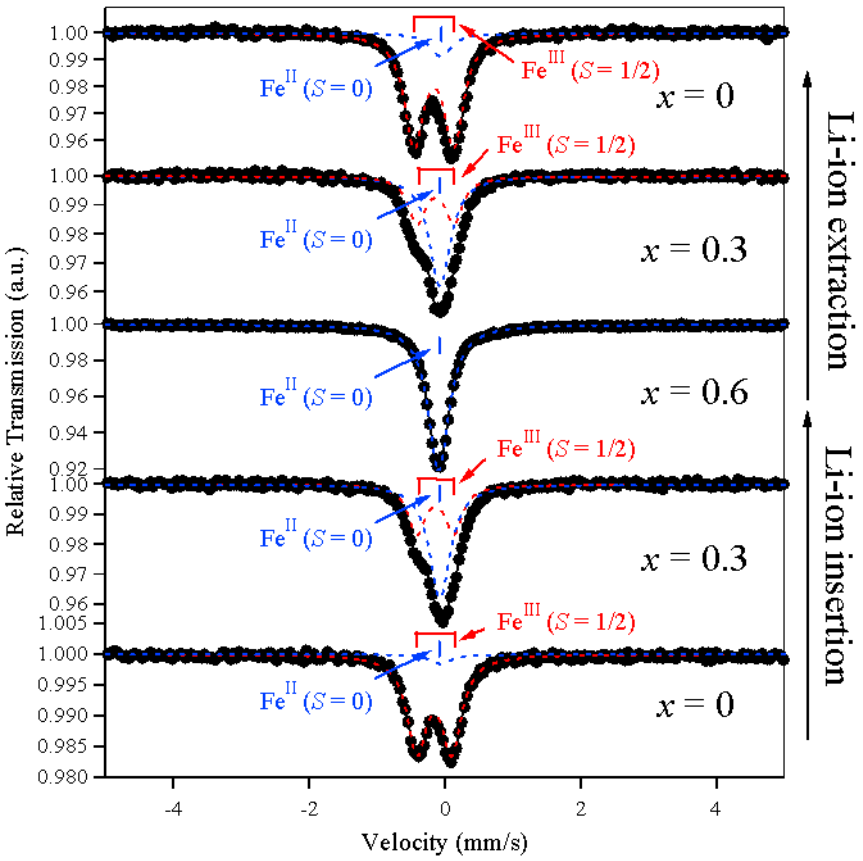

Figure 5. ^{57}Fe Mössbauer spectra for Li_x(NiFe-PBA) during Li^+ insertion/extraction (black dots: experimental data, broken lines: fitted curves).

Table 1. ^{57}Fe Mössbauer parameters of Li_x(NiFe-PBA).

sample	site	IS [mm/s]	QS [mm/s]	% Fe	structure
***x* = 0**	**1**	**-0.164(2)**	**0.512(5)**	**94.7**	**$[Fe^{3+}(CN)_6]^{3-}$**
	2	**-0.06(3)**	**0**	**5.3**	**$[Fe^{2+}(CN)_6]^{4-}$**
***x* = 0.3**	**1**	**-0.149(3)**	**0.545(7)**	**40.3**	**$[Fe^{3+}(CN)_6]^{3-}$**
(insertion)	**2**	**-0.082(2)**	**0**	**59.7**	**$[Fe^{2+}(CN)_6]^{4-}$**
***x* = 0.6**	**1**	**-0.1011(4)**	**0**	**100**	**$[Fe^{2+}(CN)_6]^{4-}$**
***x* = 0.3**	**1**	**-0.170(3)**	**0.558(7)**	**40.0**	**$[Fe^{3+}(CN)_6]^{3-}$**
(extraction)	**2**	**-0.105(2)**	**0**	**60.0**	**$[Fe^{2+}(CN)_6]^{4-}$**
***x* = 0**	**1**	**-0.169(2)**	**0.585(3)**	**89.4**	**$[Fe^{3+}(CN)_6]^{3-}$**
(extraction)	**2**	**-0.066(8)**	**0**	**10.6**	**$[Fe^{2+}(CN)_6]^{4-}$**

In general, when the guest Li^+ are distributed in the host, the free energy of the system can be described by the lattice-gas model.[33] In particular, as long as the nearest neighboring Li^+-Li^+ interaction J_{Li} is assumed to be weak, the system can be treated by the mean field approximation.[30] Based on this approximation, the OCV curve for Li_x(NiFe-PBA) is given as;

$$E(x) = E_0 + \frac{zJ_{Li}}{F}\frac{x}{x_0} - \frac{RT}{F}\ln\left(\frac{x}{x_0-x}\right).$$

Here, E_0 is the formal potential, z is the number of the nearest neighbor Li^+ sites, and x_0 is the maximum of x. The blue line in Figure 3b is the fitted results with E_0 = 3.39 V and J_{Li} = -12 meV/mol. The expression reproduced the experimental OCV, which indicates that the model is appropriate for description of the Li^+ distribution in NiFe-PBA. The small negative J_{Li} suggests weak repulsion between the neighboring Li^+ due to Coulombic interaction.

The above results demonstrated the quantitative Li^+ titration in NiFe-PBA, in which the valence state of Fe was quantitatively controlled between the paramagnetic $[Fe^{3+}(CN)_6]^{3-}$ and diamagnetic $[Fe^{2+}(CN)_6]^{4-}$. Therefore, the magnetic measurements were conducted for Li_x(NiFe-PBA) during Li-ion insertion/extraction to clarify the magnetic properties.

Li_0(NiFe-PBA) had a χT value of 2.01 emu·K·mol^{-1} at room temperature, which is greater than the spin-only value (1.23 emu·K·mol^{-1}). This difference can be ascribed partly to contribution from the orbital angular momentum of low-spin Fe^{3+} ions. Furthermore, although the XRD pattern for NiFe-PBA indicated a single cubic phase without crystalline impurity, the amorphous magnetic impurities, which cannot be detected in the XRD experiments, could also contribute to the large χT value. With decreasing temperature T, χT increased monotonically with a Weiss constant θ of 23.7 K (Figure 7a). This result indicates ferromagnetic interaction between Fe^{3+} and Ni^{2+}. The black open triangles in Figure 8a are the field-cooled magnetization M_{FC} of Li_0(NiFe-PBA) under 10 Oe. The zero-field and remnant magnetizations are showed in Figure 9a. The drastic increase in M_{FC} below 27 K suggests a dM_{FC}/dT plots (black closed triangles in Figure 8a) is 22.4 K, which is similar to the

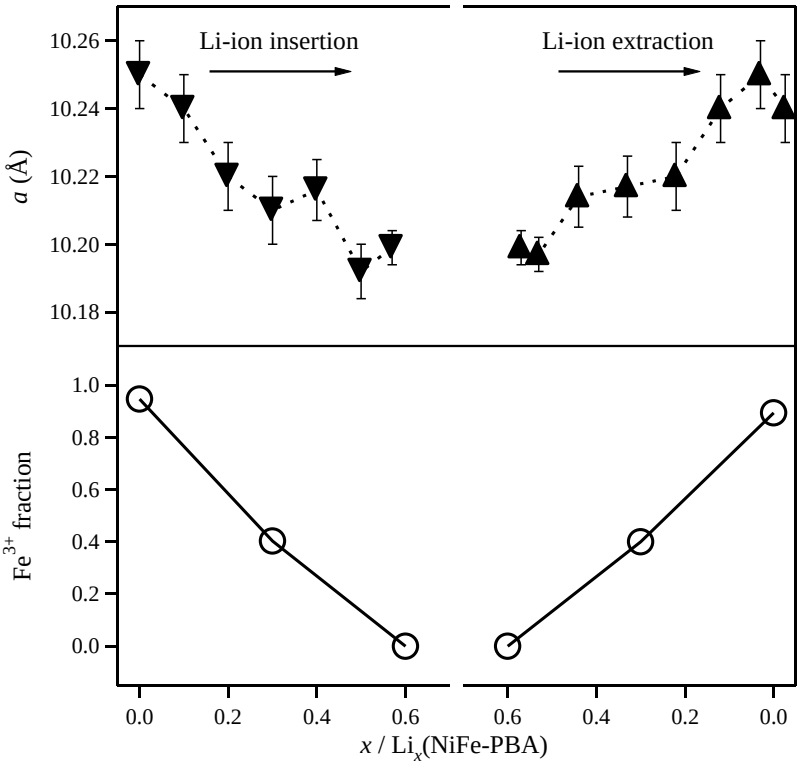

Figure 6. Lattice constant (closed triangles) and Fe^{3+} fraction (opened circles) as a function of x in Li_x(NiFe-PBA).

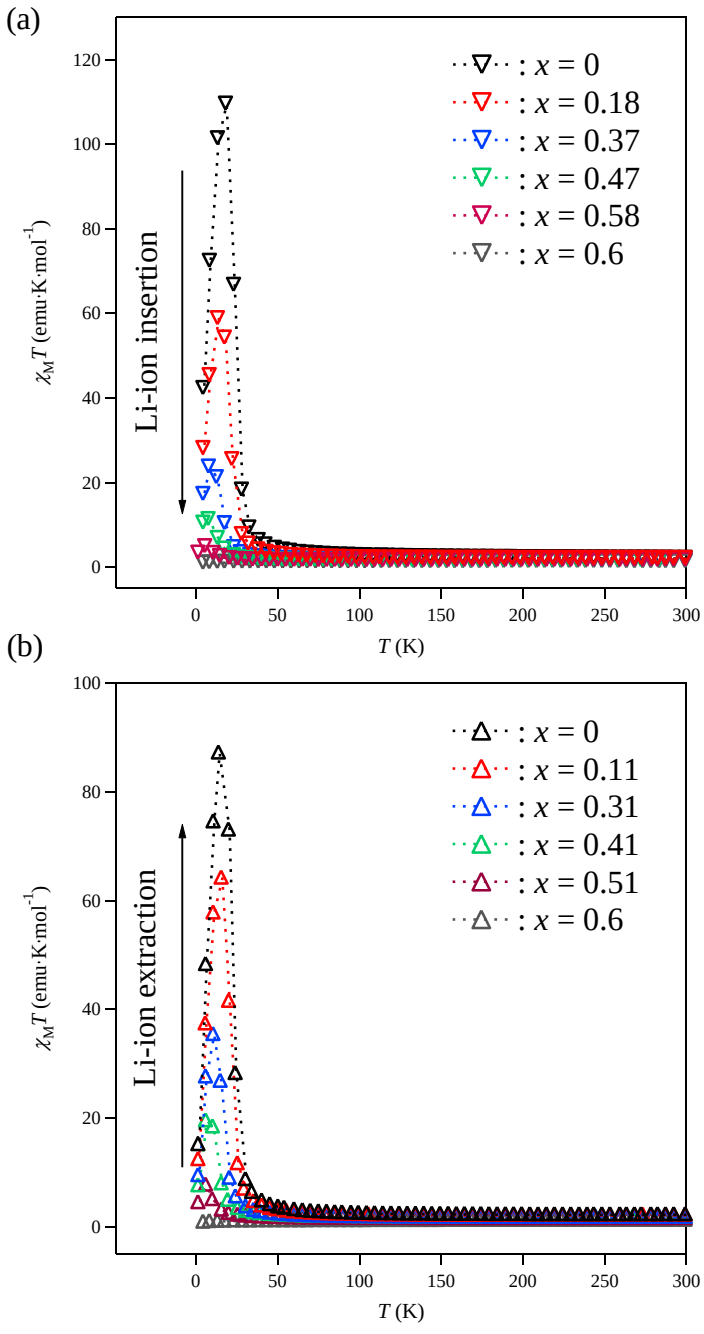

Figure 7. (a) Temperature dependence of $\chi_M T$ for Li_x(NiFe-PBA) during Li^+ insertion. (b) Temperature dependence of $\chi_M T$ for Li_x(NiFe-PBA) during Li^+ extraction.

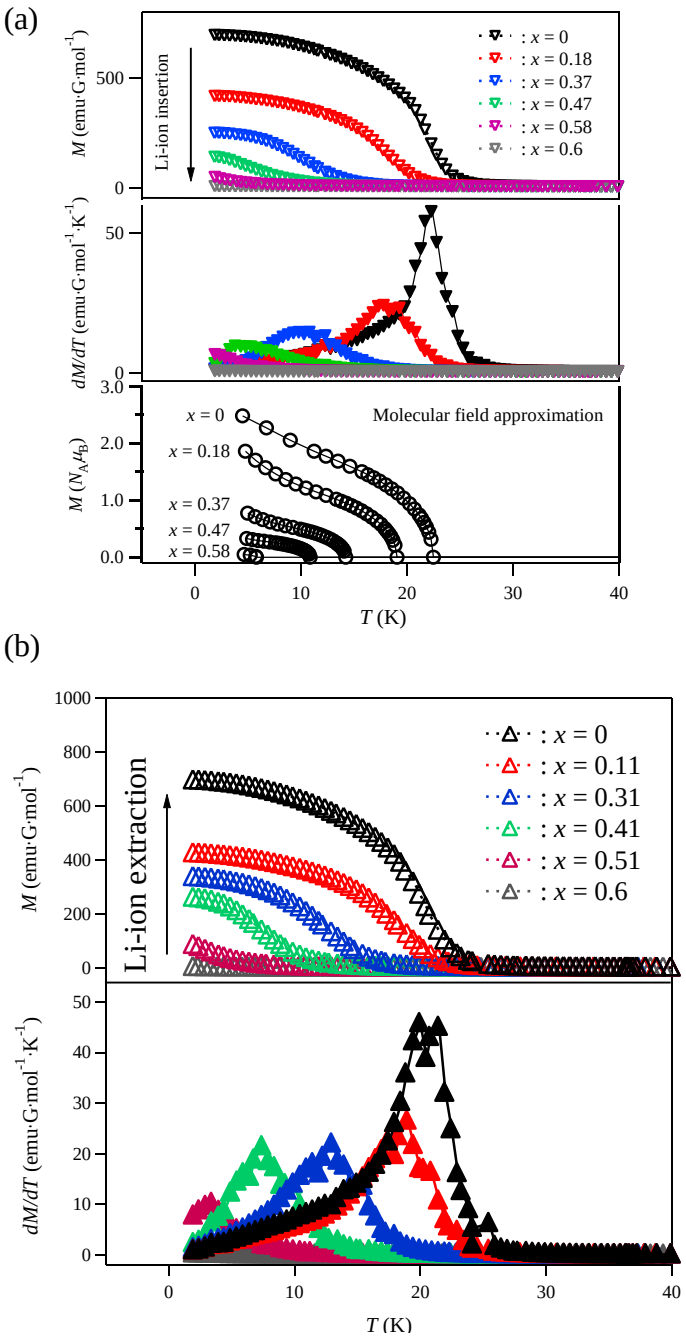

Figure. 8 (a) Field cooled magnetization M_{FC} (opened triangles), dM_{FC}/dT (closed triangles), and calculated spontaneous magnetization (open circles) for Li_x(NiFe-PBA). J_{spin} = 5.9 K was used in the calculation (see text). (b) Field cooled magnetization (M) and dM/dT for Li_x(NiFe-PBA) during Li^+ extraction.

reported value (23.6 K).[28]

Upon insertion of Li^+, χT at room temperature decreased continuously from 2.01 (x = 0) to 1.18 emu·K·mol^{-1} (x = 0.6). The χT value for $Li_{0.6}$(NiFe-PBA) did not show temperature dependence (Figure 7a), suggesting the disappearance of the ferromagnetic interaction between Fe^{3+} and Ni^{2+}. The open triangles in Figure 8a are M_{FC} of Li_x(NiFe-PBA) (x = 0.18, 0.37, 0.47, 0.58 and 0.6) under 10 Oe. The onset temperature exhibiting a drastic increase in M_{FC} was reduced continuously with increasing x. The T_C value estimated from the dM_{FC}/dT plot (closed triangles in Figure 8a) decreased from 22.4 K (x = 0) to 0 K (x = 0.6). In fact, $Li_{0.6}$(NiFe-PBA) showed no clear peak in the dM_{FC}/dT plot. These results suggest that the ferromagnetic transition was completely suppressed by 0.6 Li^+ insertion, because the reduction of paramagnetic Fe^{3+} to diamagnetic Fe^{2+} eliminated the ferromagnetic interaction between the nearest neighboring spins.

In contrast, when Li^+ was extracted from $Li_{0.6}$(NiFe-PBA), χT at room temperature increased continuously from 1.18 (x = 0.6) to 2.24 emu·K·mol^{-1} (x = 0 after Li-ion extraction). The Weiss constant of Li_0(NiFe-PBA) after Li^+ extraction is 20.6 K. This value suggests a recovered ferromagnetic interaction between Fe^{3+} and Ni^{2+} during reversible Li^+ insertion/extraction. The onset temperature exhibiting a drastic increase in M_{FC} increased continuously with decreasing x, and T_C estimated from the dM_{FC}/dT plot increased from 0 K (x = 0.6) to 20.8 K (x = 0 after Li-ion extraction) (Figure 8b). Although T_C for Li_0(NiFe-PBA) after Li^+ extraction was slightly lower than that for NiFe-PBA before Li^+ insertion due to the slight increment of diamagnetic Fe^{2+}, the ferromagnetic transition was nearly recovered after Li^+ extraction.

The M_{FC} *vs.* T plot showed the systematic control of T_C by x. In general, if the electron is distributed randomly on the Fe ions of the NiFe-PBA lattice, the free energy of the magnetic system can again be described by the mean-field approximation (so-called the molecular field approximation for the magnetic system).[34] The Hamiltonian for Li_x(NiFe-PBA) without external field can be described by:

(a)

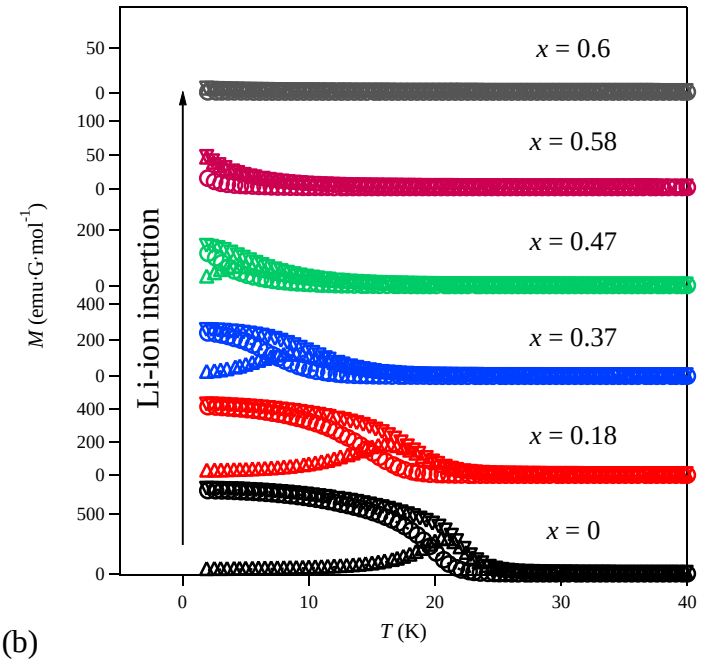

(b)

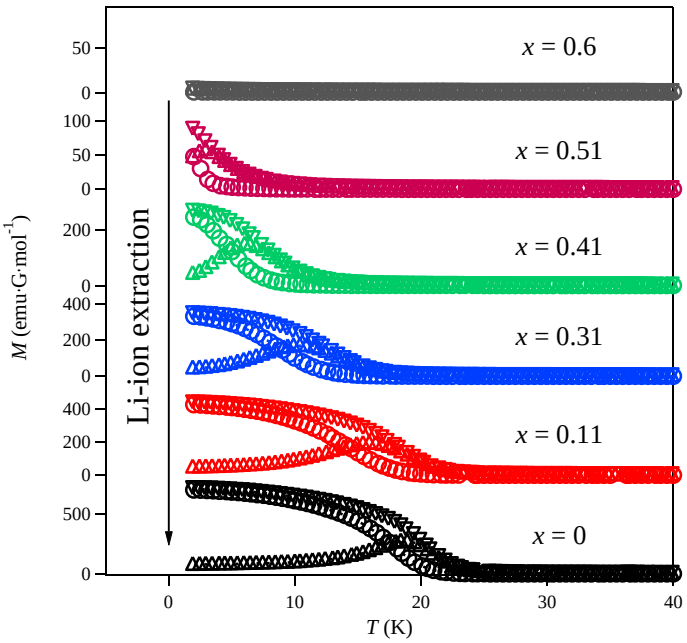

Figure 9. (a) Temperature dependence of zero field cooled (▽), field cooled (△) and remnant magnetization (○) for Li_x(NiFe-PBA) during Li^+ insertion. (b) Temperature dependence of zero field cooled (▽), field cooled (△) and remnant magnetization (○) for Li_x(NiFe-PBA) during Li^+ extraction.

$$H = - 2z_{Fe}J_{spin}\langle S_{Fe}\rangle\sum \boldsymbol{S}_{Ni} - 2z_{Ni}J_{spin}\langle S_{Ni}\rangle\sum \boldsymbol{S}_{Fe} ,$$

where z_i is the number of the nearest neighboring spin i (z_{Fe} = 6(0.6 - x) and z_{Ni} = 6), J_{spin} is the superexchange constant between Fe^{3+} and Ni^{2+}, $\langle S_i \rangle$ is the averaged value of the spin i. This can provide the temperature dependence of the spontaneous magnetization and T_C for various x. The open circles in Figure 8a depict the numerically calculated temperature dependence of the spontaneous magnetization M for various x. Note that J_{spin} was assumed to be constant (5.9 K) regardless of x. The calculated M *vs.* T plots for various x showed that the increase in x reduced both the onset temperature of M and the M value at low temperatures. The calculated plots reproduced the temperature dependence of experimental M_{FC}.

To further validate the molecular-field model, the x-T phase diagram for Li_x(NiFe-PBA) was plotted (Figure 10). The open triangles are T_C estimated from the dM/dT plots for Li_x(NiFe-PBA) during Li-ion insertion (▽)/extraction (△), respectively. The molecular-field approximation provides the x-dependence of T_C for Li_x(NiFe-PBA) as $T_C(x) = \sqrt{1-(x/0.6)}\ T_C(x=0)$, which is shown as a broken blue line in Figure 5b. The estimated T_C values were almost consistent with the theoretical plot, which confirmed the random distribution of the inserted spin.

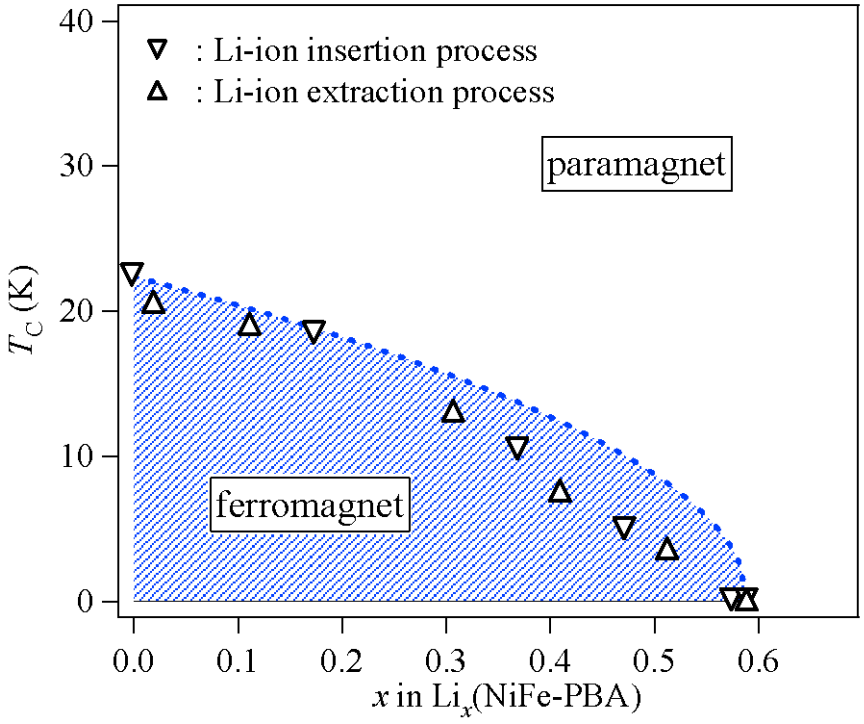

Figure. 10 x-T_C phase diagram of Li_x(NiFe-PBA). Blue dotted line is the theoretical curve based on the mean-field approximation (see text).

5.4. Conclusions

The precise control of ferromagnetism of NiFe-PBA was achieved by electrochemical quantitative Li^+/spin titration. 0.6 Li^+ could insert/extract into NiFe-PBA reversibly ($0 < x < 0.6$). The reversible lattice shrinkage/expansion in NiFe-PBA during Li^+ insertion/extraction suggested the solid solution process for the entire composition. The ^{57}Fe Mössbauer spectra showed the reversible solid state redox of the paramagnetic Fe^{3+}/diamagnetic Fe^{2+} couple. Therefore, when Li^+ inserted quantitatively, T_C of NiFe-PBA decreased gradually, and the ferromagnetic transition is completely suppressed for $x = 0.6$. On the other hand, T_C increased gradually as Li^+ is extracted. Thus, the ferromagnetism of NiFe-PBA was manipulated quantitatively by an advanced electrochemical titration technique. Furthermore, both the inserted Li^+ and spins were distributed randomly in NiFe-PBA, which was confirmed by fitting the experimental results to the corresponding thermodynamic functions based on the mean-field approximation.

References

(5-1) Hwang, H.Y.; Iwasa, Y.; Kawasaki, M.; Keimer, B.; Nagaosa, N.; Tokura, Y. *Nat. Mater.* **2012**, *11*, 103-113.

(5-2) Zhou, H.-C.; Long, J. R.; Yaghi, O. M. *Chem. Rev.* **2012**, *112*, 673-674.

(5-3) Ferlay, S.; Mallah, T.; Ouahes, R.; Veillet, P.; Verdaguer, M. *Nature* **1995**, *378*, 701-703.

(5-4) Kondo, A.; Kajiro, H.; Noguchi, H.; Carlucci, L.; Proserpio. D. M.; Ciami, G.; Kato, K.; Taketa, M.; Seki, H.; Sakamoto, M.; Hattori, Y.; Okino, F.; Maeda, K.; Ohba, T.; Kaneko, K.; Kanoh, H. *J. Am. Chem. Soc*. **2011**, *133*, 10512-10522.

(5-5) Bhar, K.; Khan, S.; Costa, J. S.; Ribas, J.; Roubeau, O.; Mitra, P.; Ghosh, B. K. *Angew. Chem. Int. Ed*. **2012**, *51*, 2142-2145.

(5-6) Renard, J. P.; Verdaguer, M.; Regnault, L. P.; Erkelens, W. A. C.; Rossatmignod, J.; Ribas, J.; Stirling, W. G.; Vettier, C. *J. Appl. Phys*. **1988**, *63*, 3538-3541.

(5-7) Sato, O.; Iyoda, T.; Fujishima, A.; Hashimoto, K. *Science* **1996**, *272*, 704-706.

(5-8) Neville, S. M.; Halder, G. J.; Chapman, K. W.; Duriska, M. B.; Southon, P. D.; Cashion, J. D.; Létard, J.-F.; Moubaraki, B.; Murray, K. S.; Kepert, C. J. *J. Am. Chem. Soc.* **2008**, *130*, 2869-2876.

(5-9) Kida, N.; Hikita, M.; Kashima, I.; Okubo, M.; Itoi, M.; Enomoto, M.; Kato, K.; Takara, M.; Kojima, N. *J. Am. Chem. Soc.* **2009**. *131*, 212-220.

(5-10) Ohkoshi, S.; Imoto, K.; Tsunobuchi, Y.; Takano, S.; Tokoro, H. *Nat. Chem*. **2011**, *3*, 564-569.

(5-11) Agustí, G.; Ohtani, R.; Yoneda, K.; Gaspar, A. B.; Ohba, M.; Sánchez-Royo, J. F.; Muñoz, M. C.; Kitagawa, S.; Real, J. A. *Angew. Chem. Int. Ed*. **2009**, *48*, 8944-8947.

(5-12) Ohtani, R.; Yoneda, K.; Furukawa, S.; Horike, N.; Kitagawa, S.; Gasper, A. B.; Muñoz, M. C.; Real, J. A.; Ohba, M. *J. Am. Chem. Soc.* **2011**. *138*, 8600-8605.

(5-13) Mahfoud, T.; Molnár, G.; Bonhommeau, S.; Cobo, S.; Salmon, L.; Demont, P.; Tokoro, H.; Ohkoshi, S.; Boukheddaden, K.; Bousseksou, A. *J. Am. Chem. Soc.* **2009**, *131*, 15049-15054.

(5-14) Miller, J. S.; Drillon, M.; *Molecules to Materials V Ed.*, Wiley-VCH Verlag GmbH & Co. 2005.

(5-15) Kaye, S. S.; Long, J. R. *J. Am. Chem. Soc.* **2005**, *127*, 6506-6507.

(5-16) Ohkoshi, S.; Nakagawa, K.; Tomono, K.; Imoto, K.; Tsunobuchi, Y.; Tokoro, H. *J. Am. Chem. Soc*. **2010**, *132*, 6620-6621.

(5-17) Matsuda, T.; Kim, J.; Moritomo, Y. *J. Am. Chem. Soc.* **2010**, *132*, 12206-12207.

(5-18) Itaya K.; Ataka, T.; Toshima, S. *J. Am. Chem. Soc.* **1982**, *104*, 4767-4772.

(5-19) Imanishi, N.; Morikawa, T.; Kondo, J.; Takeda, Y.; Yamamoto, O.; Kinugasa, N.; Yamagishi, T. *J. Power Sources* **1999**, *79*, 215-219.

(5-20) Okubo, M.; Asakura, D.; Mizuno, Y.; Kim, J.-D.; Kudo, T.; Honma, I. *J. Phys. Chem. Lett*., **2010**, *1*, 2063-2071.

(5-21) Asakura, D.; Okubo, M.; Mizuno, Y.; Kudo, T.; Zhou, H.; Amemiya, K.; de Groot, F. M. F.; Chen, J.-L.; Wang, W.-C.; Glans, P.-A.; Chang, C.; Guo, J.; Honma, I. *Phys. Rev. B* **2011**, *84*, 045117.

(5-22) Mizuno, Y.; Okubo, M.; Asakura, D.; Saito, T.; Hosono, E.; Saito, Y.; Oh-ishi, K.; Kudo, T.; Zhou, H. *Electrochim. Acta* **2012**, *63*, 139-145.

(5-23) Asakura, D.; Okubo, M.; Mizuno, Y.; Kudo, T.; Zhou, H.; Ikedo, K.; Mizokawa, T.; Okazawa, A.; Kojima, N. *J. Phys. Chem. C* **2012**, *116*, 8364-8369.

(5-24) Okubo, M.; Asakura, D.; Mizuno, Y.; Kudo, T.; Zhou, H.; Okazawa, A.; Kojima, N.; Ikedo, K.; Mizokawa, T.; Honma, I. *Angew. Chem. Int. Ed*. **2011**, *50*, 6269-6274.

(5-25) Sato, O.; Iyoda, T.; Fujishima, A.; Hashimoto, K. *Science* **1996**, *271*, 49-51.

(5-26) Sato, O.; Hayami, S.; Einaga, Y.; Gu, Z.-Z. *Bull. Chem. Soc. Jpn*. **2003**, *76*, 443-470.

(5-27) Sato, O. *J. Solid State Electrochem.* **2007**, *11*, 773-779.

(5-28) Juszczyk, S.; Johansson, C.; Hanson, M.; Ratuszna, A.; Małecki, G. *J. Phys.: Condens. Matter* **1994**, *6*, 5697-5706.

(5-29) Weppner, W.; Huggins, R. A. *J. Electrochem. Soc*. **1977**, *124*, 1569-1578.

(5-30) Bard, A. J.; Faulkner, L. R. *Electrochemical Methods: Fundamentals and Application 2nd Ed.*, John Wiley & Sons, Inc., **2001**.

(5-31) Christian, J. W. *The Theory of Transformations in Metals and Alloys 3rd Ed.*, Elsevier Science Ltd., **2002**.

(5-32) Greenwood, N. N.; Gibb, T.C. *Moessbauer Spectroscopy*, Chapman & Hall, London, **1971**.

(5-33) Bruce, P. G. *Solid State Electrochemistry*, Cambridge University Press, **1995**.

(5-34) Blundell, S. *Magnetism in Condensed Matter*, Oxford University Press, **2001**.

Chapter 6

Electrospinning-Synthesis of Wire-Structured $LiCoO_2$ for Electrode Materials of High Power Li-Ion Batteries

6.1. Introduction

Higher performance Li-ion batteries have attracted much attention for their use in advanced transportation systems, such as hybrid electric vehicles (HEVs) and electric vehicles (EVs). For the higher charge/discharge rate-capability of Li-ion batteries, faster Li^+ transfer in the cathode is essentially required. Using the nanostructured cathode materials is one of the effective ways to achieve the fast Li^+ transfer, because they possess the larger surface area and shorter Li^+ diffusion length. [1-8]

To obtain the nanostructured cathode materials, various techniques such as a post-templating method,[9] sol-gel methods,[10,11] a spray-drying method,[12] a coprecipitation method[13] and hydrothermal methods,[3-6,14-17] have been reported to date. For examples, sol-gel methods enable us to obtain various nano-sized materials from the precursor solutions containing various metal salts. The main advantage of this method is that the chemical composition could be controlled more easily and precisely than the solid-state sintering method due to the homogeneous mixing of the solutes in the liquid-phase. However, when the heat treatment is conducted at high temperature for a long duration, the particle size generally becomes large due to the crystal growth. In contrast, the wire-structure could suppress the crystal growth even under the heating condition at high temperature due to the nonwoven fabric morphology.[6] Thus, the highly crystalline wire-structured electrode materials have been fabricated by the heat treatment of the wire-structured precursors, and succeeded in achieving the higher charge/discharge rate-capability. However, the hydrothermal method used for the synthesis of the wire-structured precursors in the previous studies is not scalable for the mass production from the viewpoint of the practical application. Therefore, another process for the fabrication of the wire-structured electrode matrials has been strongly desired.

In this study, among various techniques for the synthesis of the wire-structured materials, an electrospinning method was used. The electrospinning method has attracted much attention recently, since this method can easily fabricate the wire-structure only by applying the high-voltage to the precursor solution. By using this method, various wire-structured metal carbon composites, and electrode materials like $LiFePO_4$, have been synthesized successfully.[7,19-21] It should be emphasized that the electrospinning method is highly scalable, which could be applied for the mass production process. As the electrode material for Li-ion batteries, $LiCoO_2$ was used in this study. $LiCoO_2$ is one of the commercially used cathode materials with the high energy density and excellent cyclability,[22] thus the fabrication of nanostructured $LiCoO_2$ by the scalable technique like the electrospinning method is of particular importance.

Here, the fabrication of wire-structured $LiCoO_2$ via the electrospinning method was investigated clarified the electrode properties of wire-structured $LiCoO_2$.

6.2. Experimental Methods

Reagents were of commercial grade and used without purification. Wire-structured $LiCoO_2$ was synthesized by the electrospinning method. Typically, $Li(CH_3COO)\cdot 2H_2O$ (0.165 M), $Co(CH_3COO)_2\cdot 4H_2O$ (0.15 M), 1.5 g of poly (vinyl alcohol) (PVA) and 50 mg of polyoxyethylene octyl phenyl ether were dissolved into a mixed solution of 15 ml of H_2O, 1 ml of CH_3COOH and 4 ml of C_2H_5OH. The precursor solution was obtained by aging the solution at 90 ˚C for 1 h. In case of the precursor solution including VGCF, 0.4 g of VGCF was ultrasonically dispersed into the precursor solution by a sono-horn. The resultant precursor solution was poured into a syringe equipped with a metal needle, and 20 kV of direct current electric field was applied between the needle and Al foil target. The as-spun materials were dried in vacuo at 100 ˚C for 1 h, and then the dried as-spun materials were separated from the Al foil. The resultant dried as-spun materials were heat-treated at 800 ˚C for 5 h under air flow.

The powder X-ray diffraction (XRD) measurement was carried out on a Bruker D8 Advance using Cu $K\alpha$ radiation in steps of 0.01˚ over the 2θ range of 5 – 80˚. The unit cell parameters were calculated by the least square fitting with peak top values. The scanning electron microscopy (SEM) and bright field transmission electron microscopy (bright field TEM) were carried out on a Carl Zeiss Supra 35 and JEOL JEM-2010F (200kV accelerating voltage), respectively. The Raman spectra were recorded from NIHON BUNKO Ventuno spectrometer (NSR-1000DT).

For the electrochemical measurements, a three-electrode-type glass cell was used. The electrode material was ground with 45 wt % acetylene black and 5 wt % poly(tetrafluoroethylene) into a paste. Generally speaking, normal electrodes in commercial Li-ion batteries contain only 5 % of conductive materials. However, our scope of this paper was focused on the estimation of the high-rate Li-ion intercalation/extraction in wire-structured $LiCoO_2$. From this viewpoint, 45 % of the conductive material was used for all samples. The high electronic conductivity suppressed some unfavorable problems in the high-rate experiment like an IR drop. Note that the electric double layer capacity of the acetylene black is below 1 mAh/g between the cut-off voltages, thus it can be ignored compared to the intercalation capacity of $LiCoO_2$. For the electrolyte, 1 M $LiClO_4$/ethylene carbonate-diethyl carbonate (EC-DEC, 1:1 V/V %) was used. The charge/discharge measurements were carried out with a galvanostat (SD-8, Hokuto Denko), and the cut-off voltages were 3.0 V and 4.2 V [vs. Li/Li^+].

The electrochemical impedance spectra (EIS) were recorded with a frequency response analyzer (SI 1250, Solatron) at the frequency ranging from 5 mHz to 50 kHz with an amplitude of 10 mV.

6.3. Results and Discussion

The as-spun fibers were prepared by an electrospinning method. The precursor aqueous solution of Li, Co, PVA and polyoxyethylene octyl phenyl ether was electrospun to fabricate the as-spun fiber. Furthermore, the precursor solution with dispersed VGCF was also electrospun to control the diameter of the fiber, because the addition of carbon nanotubes in the precursor solution has been reported to reduce the diameter of the as-spun fibers.[23-26] The SEM images of the as-spun fibers, which were

obtained without/with VGCF, are shown in Figure 1a, b, and Figure 1c, d, respectively. The low magnification images (Figure 1a and 1c) indicate that the nonwoven fabric morphology is successfully formed by electrospinning each precursor solution.

Based on the high magnification images (Figure 1b and 1d), the averaged diameter of the as-spun fibers from the precursor solution with/without VGCF are estimated to be 0.5 μm and 1.2 μm, respectively. Thus, the diameter of the as-spun fiber from the precursor solution with VGCF is thinner than that of the as-spun fiber from the precursor solution without VGCF. This result well agrees with the previous report.[27] In this literature, the origin for the effect of the VGCF addition was ascribed to the electronic conductivity of VGCF. However, it is well known that non-electrolytes in an aqueous solution generally decrease the surface tension of water.[28] Thus, one possible explanation for the effect of the VGCF addition is the reduction of the surface tension by dispersing of VGCF in the precursor solution. Since the reduced surface tension requires the decrease in the diameter of the fiber for the surface equilibrium, the as-spun fiber from the solution with VGCF gave the as-spun fiber with a thinner diameter.

The as-spun fibers were heated at 800 ˚C for 5 h in air. Figure 2 shows XRD patterns of heat-treated samples obtained from the precursor solutions without/with VGCF, respectively. Hereafter, the former is denoted as 1, while the latter is denoted as 2. Both 1 and 2 showed sharp peaks indexed in $LiCoO_2$ without any impurity. However, it is well known that $LiCoO_2$ can be indexed into two space groups depending on the degree of the cation mixing between Co- and Li-ions, namely a high temperature phase (HT-$LiCoO_2$, a layered structure, $R\bar{3}m$) and a low temperature phase (LT-$LiCoO_2$, a spinel structure, $Fd\bar{3}m$). Although the diffraction patterns for two space groups are similar, these structures can be distinguished by comparing the *c/a* ratio. The *c/a* ratio of HT-$LiCoO_2$ and LT-$LiCoO_2$ has been reported to be about 5.00 and 4.90, respectively.[29] The calculated unit cell parameters for the heat-treated samples are $a = 2.8158(5)$ Å, $c = 14.054(4)$ Å for 1 ($c/a = 4.99$), and $a = 2.8162(8)$ Å, $c =$

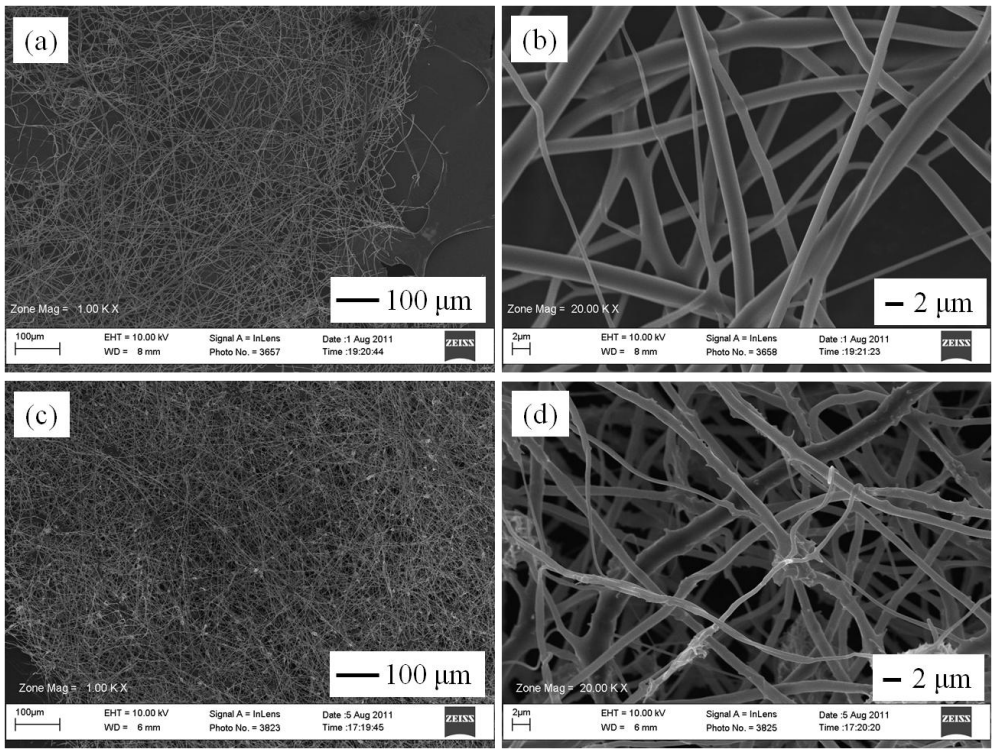

Figure 1. SEM images for the as-spun fibers obtained from the precursor solutions. (a), (b): without VGCF, and (c), (d): with VGCF.

14.070(7) Å for 2 (c/a = 5.00), respectively. These values are consistent with the previously reported values (a = 2.8166 Å, c = 14.052 Å and c/a = 4.99)[30], and the c/a ratio clearly implies that both are a HT-$LiCoO_2$ phase. In addition, there are no peaks indexed as VGCF in the XRD pattern of 2,[7] thus the VGCF would be decomposed completely during heat treatment.

The SEM and bright field TEM images are shown in Figure 3a, c for 1 and Figure 3b, d for 2, respectively. Although both samples show the plate-like shaped particles, the particle size of 1 is much larger than that of 2. The averaged particle size is about 1.5 μm for 1, and 400 nm for 2, respectively. This result suggests that the existence of VGCF in the as-spun fiber suppresses the crystal growth of $LiCoO_2$ particles. From the TG-DTA measurement of the as-spun fibers without VGCF (Figure 4a), the abrupt weight loss occurs at 400 ˚C. This weight loss could be attributed to the thermal decomposition of PVA. On the other hand, as for the as-spun fiber from the solution with VGCF, the weight loss gradually occurred from 400 to 550 ˚C, and the abrupt thermal decomposition of PVA at 400 ˚C was not observed (Figure 4b). The gradual weight loss is attributed to decomposition of PVA and VGCF. It is assumed that the existence of VGCF suppresses the decomposition of PVA. Thus, the residual organic compounds such as carbon by slow decomposition of PVA and VGCF may prevent the crystal growth of $LiCoO_2$ because similar phenomenon is reported in other materials such as ZnO and hydroxyapatite.[31,32]

In order to confirm the degree of the cation mixing in 1 and 2, the Raman spectroscopy was carried out. According to the previous reports, two Raman bands (A_{1g} and E_g modes) were observed for the HT-$LiCoO_2$ phase, while four Raman bands were observed for the LT-$LiCoO_2$ phase.[29,33,34] Figure 5 shows the Raman spectra for 1 and 2. Both showed two intense Raman bands. This result confirms that both are the HT-$LiCoO_2$, as suggested by the XRD result. However, the peak positions of the A_{1g} and E_g modes for 2 show the red-shift compared to those of 1. Furthermore, the full width at half maximum(FWHM) of these two Raman bands for 2 (10.1 cm^{-1} for A_{1g} band and 4.37 cm^{-1} for E_{1g} band) is slightly larger than that for 1 (8.6 cm^{-1} for A_{1g} band and 3.92 cm^{-1} for E_{1g} band). Since the red shift and larger FWHM of the Raman bands for $LiCoO_2$ have been reported to suggest the smaller crystallite

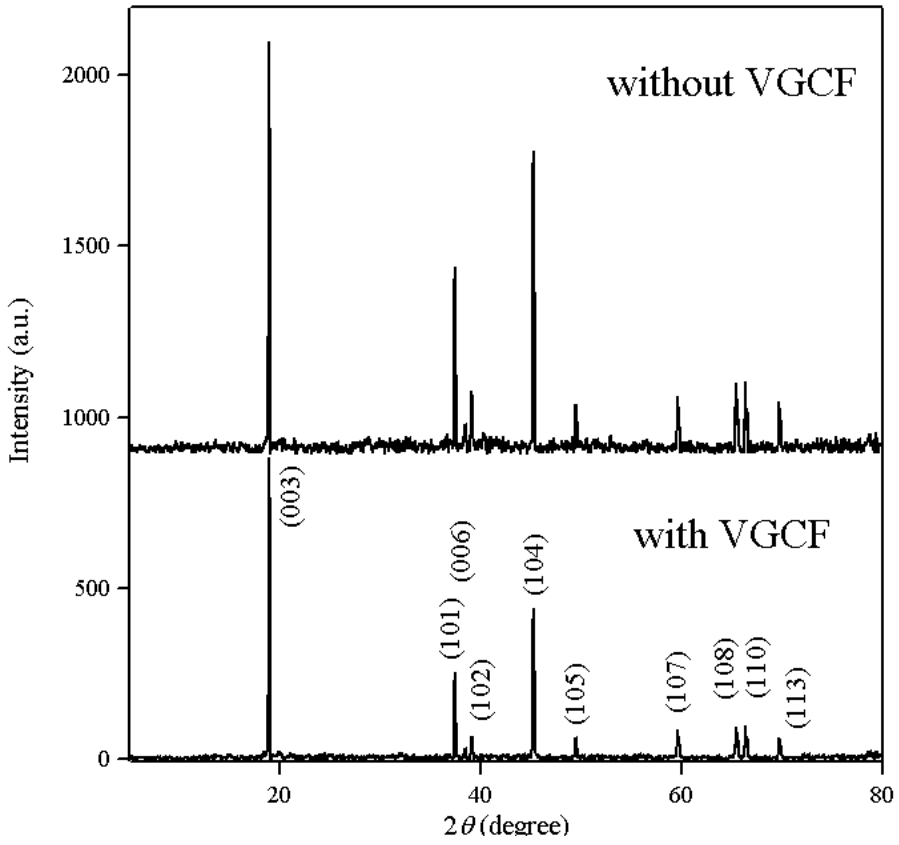

Figure 2. XRD patterns for the heat-treated samples fabricated from the precursor solutions without VGCF (1) and that with VGCF (2).

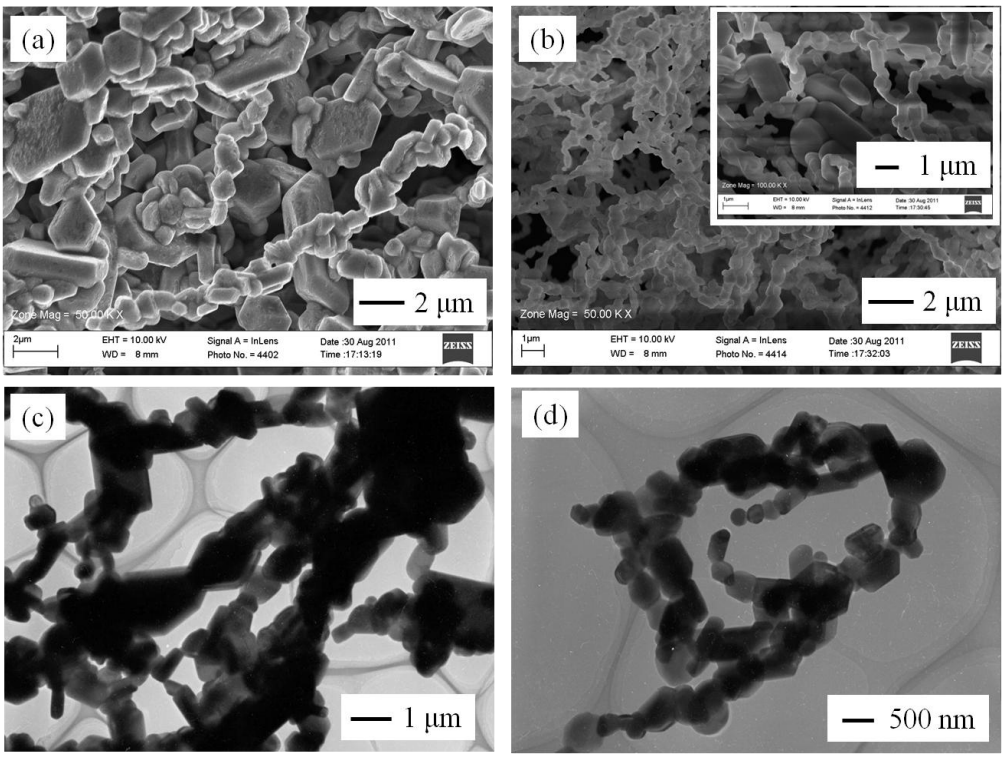

Figure 3. (a) SEM image for 1, (b) SEM image for 2, Inset: high magnification image, (c) bright field TEM image for 1 and (d) TEM image for 2.

size,[3,34] this result suggests that the crystallite size of 2 is smaller than that of 1. The above SEM and bright field TEM results can be easily agreed from Raman spectra.

The electrode performance of 1 and 2 was tested by the charge/discharge experiments at the constant current density of 50 mA/g (0.37 C rate). Figure 6a shows the charge/discharge curves for 1 and 2 at the 1st and 2nd cycles. The attainable capacity at the 1st charge/discharge processes is almost same (~ 140 mAh/g) for 1 and 2, which is consistent with the theoretical capacity for $LiCoO_2$ (137 mAh/g, $0.5 < x < 1$ in Li_xCoO_2). In general, the LT-$LiCoO_2$ phase exhibits a small charge/discharge potential plateau at 3.7 V due to the redox potential of the Co^{3+} in the Li^+ layer.[34,36] However, the charge/discharge plateau for 1 and 2 was observed only at 3.9 V, thus there is no cation mixing between Co^{3+} and Li^+ in both samples.

Figure 6b shows the Coulombic efficiency and cyclabilities for 1 and 2. In case of 1, the Coulomic efficiency at the 1st cycle is 105 %. The irreversible capacity for 1 at the 1st cycle may be ascribed to the existence of some impurities on the large surface of the wire-structure. However, as the cycle number increases, the Coulombic efficiency approaches 100 %, which suggests the reversible Li-ion intercalation/extraction in the wire-structured $LiCoO_2$. The Coulombic efficiency for 2 showed a cycle number dependence similar to that of 1, indicating a small amount of surface impurities and the reversible Li^+ intercalation/extraction in the wire-structured $LiCoO_2$. However, the irreversible capacity for 2 at the 1st cycle (the Coulombic efficiency: 107 %) is slightly larger than that for 1. Presumably, the slow thermal decomposition of PVA and VGCF suggested by the TG-DTA may result in some residual carbons on the surface, which should contribute to the initial irreversible electrochemical reaction.

Concerning the cyclability, the discharge capacity for 1 gradually decreases from 135 to 108 mAh/g after 30 cycles (20 % loss), while the discharge capacity for 2 decreases from 137 to 89 mAh/g after 30 cycles (35 % loss). Since nano-sized $LiCoO_2$ has been reported to show the poor cyclability,[3,37] the poorer cyclability of 2 may relate to the smaller particle size of 2 than that of 1.

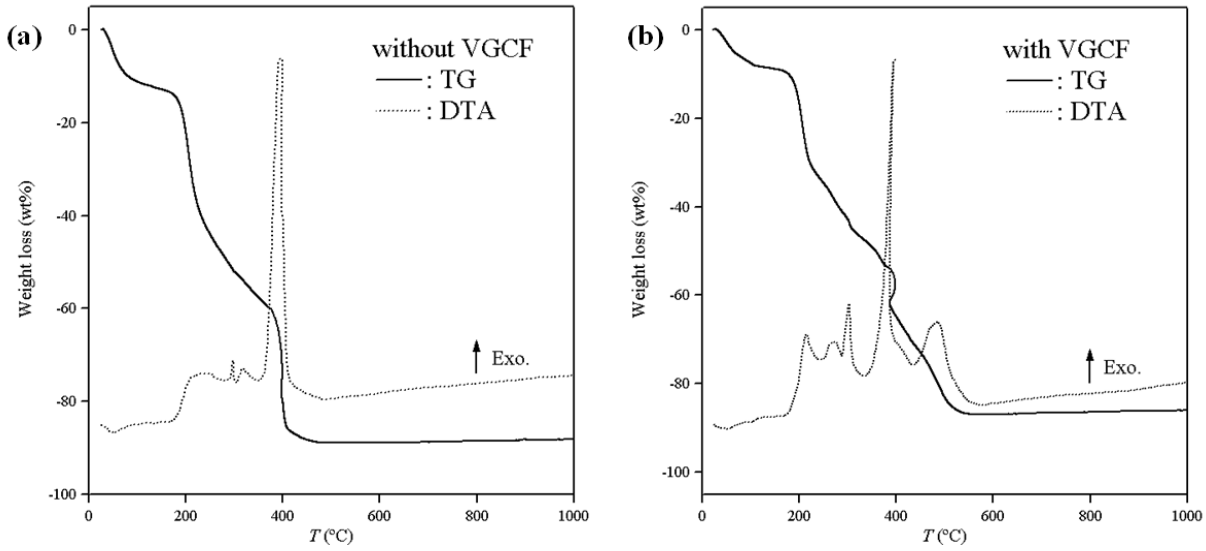

Figure 4. TG-DTA curves of as-spun fibers obtained by the precursor solutions (a) without VGCF and (b) with VGCF. Solid lines: TG and broken lines: DTA.

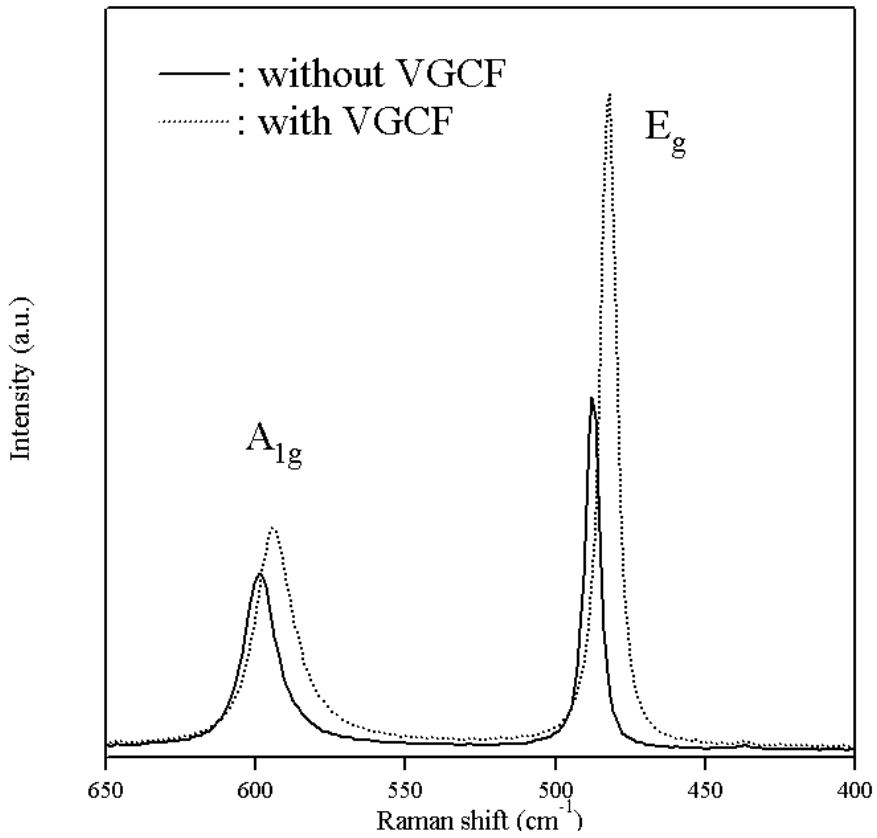

Figure 5. Raman spectra for 1 (solid line) and 2 (broken line).

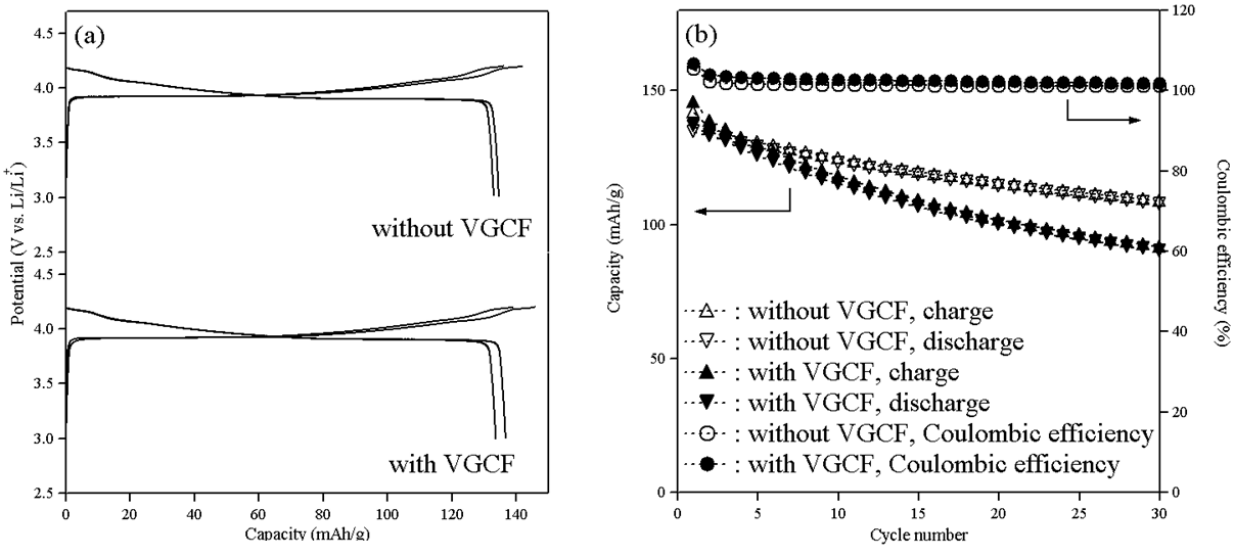

Figure 6. (a) Charge/discharge curves at the 1st and 2nd cycle for 1 and 2, and (b) cyclabilities and Coulombic efficiency for 1 (opened triangles and opened circles, respectively) and 2 (closed triangles and closed circles, respectively).

To clarify the mechanism of the electrochemical reaction in wire-structured $LiCoO_2$, the electrochemical impedance spectroscopy (EIS) was carried out for the three-electrode electrochemical cells before the 1st charge cycle, after 10, 20 and 30 charge/discharge cycles, respectively. The open circles in Figure 7a shows the typical Nyquist plot for the cell of 1 before the 1st cycle. One semicircle corresponding to a RC circuit (the interfacial charge transfer resistance in parallel with the interfacial double layer capacitance) was observed in the frequency range from 40 Hz to 3 kHz, while a linear slope due to the Warburg impedance (the ionic bulk diffusion in $LiCoO_2$) was observed in the lower frequency region.

To evaluate each resistance quantitatively, nonlinear least-squares fitting was carried out. The equivalent circuit for the typical charge/discharge process (inset in Figure 7a) was used to analyze the spectra. The model was established as simple as possible to minimize the number of parameters. In the equivalent circuit, R_s and R_1 are the series resistance and interfacial charge-transfer resistance, respectively. CPE represents the constant phase element (CPE, $Z_{CPE} = \{T_{CPE}(j\omega)^{\alpha}\}^{-1}$, T_{CPE}, α: empirical parameters, ω: angular frequency). The CPE is commonly used to describe the depressed semicircle due to roughness of the electrode surface.[38] In this study, wire-structured $LiCoO_2$ has the porous surface, thus the CPE instead of a capacitor was used for the fitting. Z_w is the Warburg impedance which corresponds to the ionic bulk diffusion in a electrode material with an impermeable boundary condition and distributed relaxation time ($Z_W = \{R_W\coth(iT_W\omega)^{\beta}\}(iT_W\omega)^{-\beta}$, R_W: diffusion resistance, T_W: characteristic diffusion time, β: an empirical parameter).[39] The result of the curve-fitting is also shown as the solid line in Figure 7a, and fits well with the experimental data. The used parameters are R_s = 45.17 Ω, R_1 = 22.72 Ω, T_{CPE} = 54.7 μF, α_{CPE} = 0.954, R_W = 22 mΩ, $T_W = 1.94\times10^{-5}$ s, β = 0.457. This result suggests that the electrochemical system is well represented by the used equivalent circuit. All the EIS spectra were fitted by this equivalent circuit.

Figure 7b shows the charge-transfer resistance (R_1) for 1 and 2 as a function of the cycle number. R_1 for 1 increases from 22.72 Ω to 55.64 Ω after 30 charge/discharge cycles (145 % increase), whereas R_1 for 2 increases from 24.54 Ω to 65.22 Ω after 30 charge/discharge cycles (166 % increase). It should be

emphasized that R_1 for both 1 and 2 drastically increases during the initial 10 cycles. As mentioned above, the Coulombic efficiency at the 1st cycle for both 1 and 2 deviated from 100 % maybe due to the surface impurities.[40] Thus it is presumed that the products of the irreversible electrochemical reaction at the surface may behave as a surface resistive layer to prevent the electrode-electrolyte interfacial Li-ion transfer. In consequence, R_1 increases with increasing the cycle number, and the charge/discharge capacity of 1 fades gradually. Furthermore, since the irreversible capacity of 2 at the 1st cycle is larger than that of 1, the amount of the resistive products at the surface for 2 should be more significant. Therefore, the charge/discharge capacity of 2 fades more rapidly than that of 1.

Finally, the high charge/discharge rate-capability for 1 and 2 was investigated. Figure 8a shows the charge/discharge curves at C/4 (34 mA/g), 1 C (137 mA/g), 5 C (685 mA/g) and 10 C (1.37 A/g) rates, respectively. The discharge capacity for 1 decreases from 127 mAh/g at C/4 rate to 108 mAh/g at 10 C rate (15 % loss), while that for 2 decreases from 129 mAh/g at C/4 rate to 103 mAh/g at 10 C rate (20 % loss). Assuming the bulk Li^+ diffusion in the $LiCoO_2$ is the rate-determining step, the high charge/discharge rate-capability should be achieved by nanosizing.[3,41] However, the rate capability as a function of the current density in Figure 8b clearly shows that the rate capability for 2 is slightly lower than that for 1, although the particle size of 2 is much smaller than that of 1. This result indicates that the Li-ion diffusion in $LiCoO_2$ is not a rate-determining step in this system at least up to 10 C rate. As mentions above, the EIS results suggested that the interfacial charge-transfer resistance increases after the charge/discharge cycles, especially in 2. The large interfacial charge-transfer resistance of 2 may cause the low charge/discharge rate-capability.

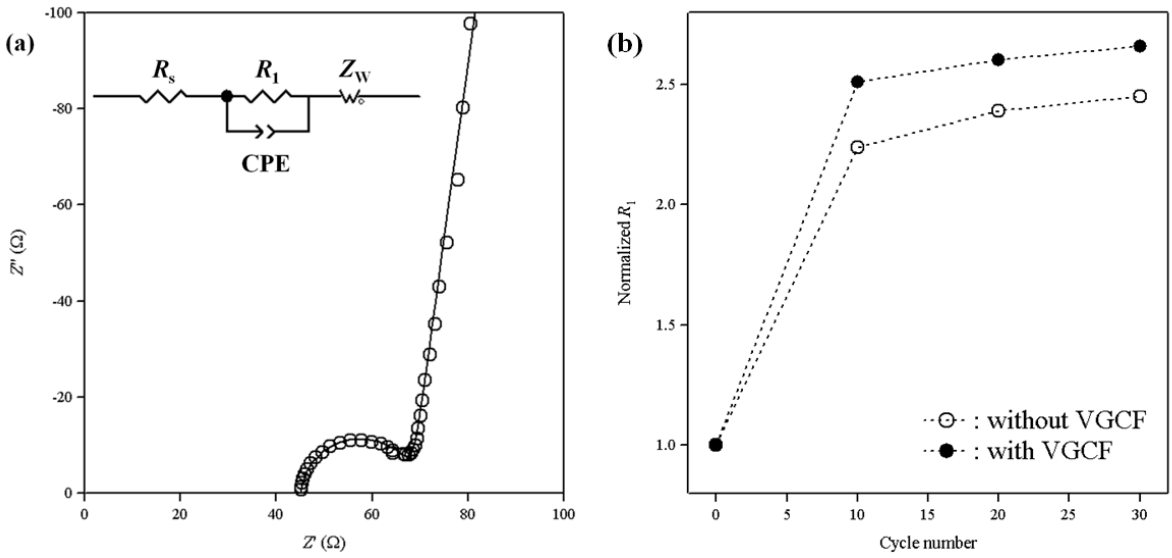

Figure 7. (a) Typical Nyquist plot (open circles) and fitted curve for 1 before the 1st charge/discharge cycle. Inset: equivalent circuit used in the fitting. R_s: series resistance, R_1: charge transfer resistance, CPE: constant phase element, Z_W: Warburg impedance (see text), (b) The normalized fitted value of R_1 for 1 (opened circles) and 2 (closed circles) at various charge/discharge cycles.

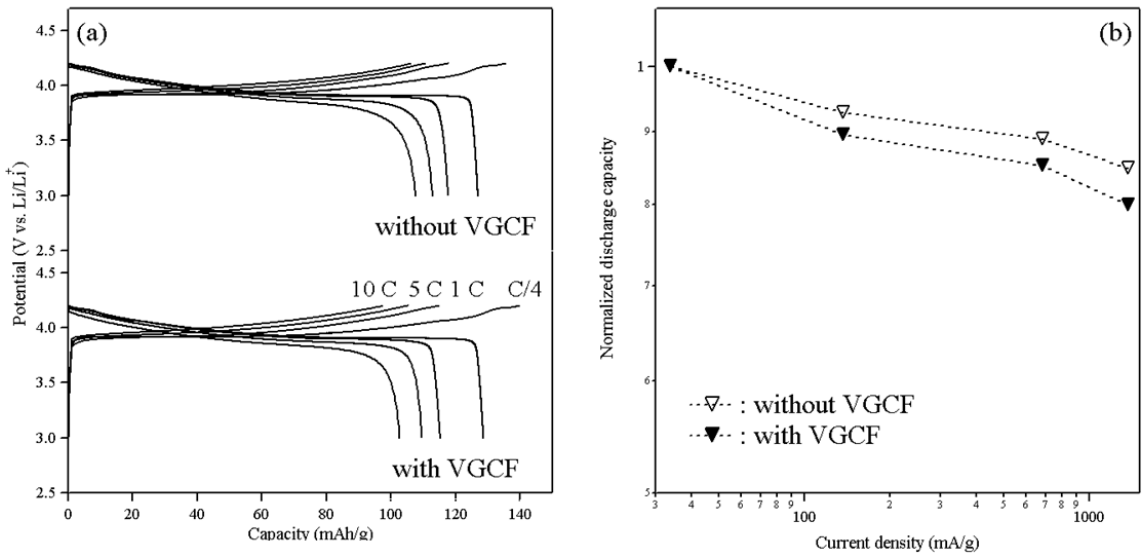

Figure 8. (a) Rate-capabilities for 1 and 2, (b) normalized discharge capacities for 1 (open triangles) and 2 (closed triangles) at various current densities.

6.4. Conclusions

An electrospinning method was employed to fabricate wire-structured $LiCoO_2$. The diameter of the as-spun fiber obtained from the precursor solution with VGCF was thinner than that of the as-spun fiber obtained from the precursor solution without VGCF. Both precursor gave the wire-structured $LiCoO_2$ successfully after the heat treatment, while, the particle size of $LiCoO_2$ obtained from the precursor solution with VGCF is smaller than that of $LiCoO_2$ obtained from the precursor solution without VGCF. Thus, the addition of VGCF in the precursor solution could control the diameter of the wire-structure. The charge/discharge capacity of $LiCoO_2$ obtained from the precursor solution with VGCF faded more rapidly than that of $LiCoO_2$ obtained from the precursor solution without VGCF. This could be explained reasonably by the surface resistive layer produced by the irreversible electrochemical reaction at the initial cycles. The existence of the surface resistive layer could also explain the lower charge/discharge rate-capability of $LiCoO_2$ obtained from the precursor solution with VGCF. Therefore, in order to improve the electrode performance of the wire-structured $LiCoO_2$ electrode, the irreversible capacity at the initial cycles should be suppressed.

References

(6-1) Armand, M.; Tarascon, J. M. *Nature*, **2008**, *451*, 652-657.

(6-2) Wang, Y.; Cao, G. *Adv. Mater*. **2008**, *20*, 2251-2269.

(6-3) Okubo, M.; Hosono, E.; Kim, J.-D.; Enomoto, M.; Kojima, N.; Kudo, T.; Zhou, H.; Honma, I. *J. Am. Chem. Soc*. **2007**, *123*, 7444-7452.

(6-4) Okubo, M.; Kim, J.; Kudo, T.; Zhou H.; Honma, I. *J. Phys Chem. C* **2009**, *113*, 15337-15342.

(6-5) Okubo, M.; Mizuno, Y.; Yamada, H.; Kim, J.-D.; Hosono, E.; Zhou, H.; Kudo, T.; Honma, I. *ACS nano* **2010**, *4*, 741-752.

(6-6) Hosono, E.; Kudo, T.; Honma, I.; Matsuda, H.; Zhou, H. *Nano Lett*. **2009**, *9*, 1045-1051.

(6-7) Hosono, E.; Wang, Y.; Kida, N.; Enomoto, M.; Kojima, N.; Okubo, M.; Matsuda, H.; Saito, Y.; Kudo, T.; Honma, I.; *et al*. *ACS Appl. Mater. Interfaces* **2010**, *1*, 212-218.

(6-8) Hu, Y.-S.; Kienle, L.; Guo, Y. G.; Maier, J. *Adv. Mater*. **2006**, *18*, 1421-1426.

(6-9) Jiao, F.; Shaju, K. M.; Bruce, P. G. *Angew. Chem. Int. Ed*. **2005**, *44*, 6550-6553.

(6-10) Peng, Z. S.; Wan, C. R.; Jiang, C. Y. *J. Power Sources* **1998**, *72*, 215-220.

(6-11) Yoon, W. S.; Kim, K. B. *J. Power Sources* **1999**, *81-82*, 517-523.

(6-12) Li, Y.; Wan, C.; Wu, Y.; Jiang, C.; Zhu, Y. *J. Power Sources* **2000**, *85*, 294-298.

(6-13) Chen, H.; Qiu, X.; Zhu, W.; Hagenmuller, P. *Electrochem. Commun*. **2002**, *4*, 488-491.

(6-14) Larcher, D.; Palacin, M. R.; Amatucci, G. G.; Tarascon, J. M. *J. Electrochem. Soc*. **1997**, *144*, 408-417.

(6-15) Tabuchi, M.; Ado, K.; Kobayashi, H.; Sakaebe, H.; Kageyama, H.; Masquelier, C.; Yoneyama, M.; Hirano, A.; Kanno, R. *J. Mater. Chem*. **1999**, *9*, 199-204.

(6-16) Kobayashi, H.; Shigemura, H.; Tabuchi, M.; Sakaebe, H.; Ado, K.; Kageyama, H.; Hirano, A.; Kanno, R.; Wakita, M.; Morimoto, S.; *et al*. *J. Electrochem. Soc*. **2000**, *147*, 960-969.

(6-17) Burukhin, A.; Brylev, O.; Hany, P.; Churagulov, B. R. *Solid State Ionics* **2002**, *151*, 259-263.

(6-18) Kameoka, J.; Czaplewski, D.; Liu, H.; Craighead, H. G. *J. Mater. Chem*. **2004**, *14*, 1503-1505.

(6-19) Gu, Y.; Chen, D.; Jiao, X. *J. Phys. Chem. B* **2005**, *109*, 17901-17906.

(6-20) Sell, S. A.; Bowlin, G. L. *J. Mater. Chem.* **2008**, *18*, 260-263.

(6-21) Dong, Z.; Kennedy, S. J.; Wu, Y. *J. Power Sources* **2011**, *196*, 4886-4904.

(6-22) Mizushima, K.; Jones, P. C.; Wiseman, P. J.; Goodenough, J. B. *Mat. Res. Bull.* **1980**, *15*, 783-789.

(6-23) Ju, Y. W.; Choi, G. R.; Jung, H. R.; Lee, W. J. *Electrochim. Acta* **2008**, *53*, 5796-5803.

(6-24) Wong, K. K. H.; Allmang, M. Z.; Hutter, J. L.; Hrapovic, S.; Luong, J. H. T.; Wan, W. *Carbon*, **2009**, *47*, 2571-2578.

(6-25) Chen, I. H.; Wang, C. C.; Chen, C. Y.; *J. Phys. Chem. C* **2010**, *114*, 13532-13539.

(6-26) Tan, S. H.; Inai, R.; Kotaki, M.; Ramakrishna, S. *Polymer* **2005**, *46*, 6128-6134.

(6-27) Lamadtra, F. R.; Nanni, F.; Camilli, L.; Matassa, R.; Carbone, M.; Gusmano, G. *Chem. Eng. J.* **2010**, *162*, 430-435.

(6-28) Mullin, J. W. *Crystallization*, 4th ed.; Elsevier Butterworth-Heinemann: Oxford, 2009.

(6-29) Huang, W.; Frech, R.; *Solid State Ionics* **1996**, *86-88*, 395-400.

(6-30) Johnston, W. D.; Heikes, R. R.; Sestrich, D. *J. Phys. Chem. Solids* **1958**, *7*, 1-13.

(6-31) Hwang, K.; Lim, Y. *Surface and Coatings Technology* **1999**, *115*, 172-175.

(6-32) Kang, B.; Hwang, K.; Jeong J. *J. Sol-Gel Sci. Technol*. **2007**, *43*, 145-149.

(6-33) Larcher, D.; Delobel, B.; Laffont, L. D.; Simons, E.; Blach, J. F.; Baudrin, E. *Inorg. Chem*. **2010**, *49*, 10949-10955.

(6-34) Okubo, M.; Hosono, E.; Kudo, T.; Zhou H.; Honma, I.; *J. Phys. Chem. Solids* **2008**, *69*, 2911-2915.

(6-35) Rossen, E.; Reimers, J. N.; Dahn, J.R.; *Solid State Ionics* **1993**, *62*, 53-60.

(6-36) Kang, S. G.; Kang, S. Y.; Ryu, K. S.; Chang, S. H. *Solid State Ionics* **1999**, *120*, 155-161.

(6-37) Okubo, M.; Hosono, E.; Kudo, T.; Zhou, H.; Honma, I. *Solid State Ionics* **2009**, *180*, 612-615.

(6-38) Barsoukov, E.; Macdonald, J.R. *Impedance spectroscopy*; John Wiley & Sons, Inc.: Hoboken, New Jersey, 2005.

(6-39) Ho, C.; Raistrick, I. D.; Huggins, R. A. *J. Electrochem. Soc*. **1980**, *127*, 343-350.

(6-40) Liu, N.; Li, H.; Wang, Z.; Huang, X.; Chen, L. *Electrochem. Solid State Lett*. **2006**, *9*, A328-A331.

(6-41) Jo, M.; Hong, Y. S.; Choo, J.; Cho, J. *J. Electrochem. Soc*. **2009**, *156*, A430-A434.

Chapter 7

Conclusions

Higher power Li-ion batteries have attracted much attention for their use in advanced vehicles and grid-scale energy storage, thus faster Li^+ transfer in the battery is essentially required.

In this research, detailed studies on the interfacial charge transfer with Prussian blue analogs as the model electrodes were conducted, because the Li^+ transfer at the interface between electrode-electrolyte considered affecting strongly on the kinetics of a charge-and-discharge reaction.

In chapter 2, Li^+ and Na^+ transfer at the MnFe-PBA electrode-electrolyte interface was investigated by EIS. EIS suggested that ion transfer at the MnFe-PBA electrode-electrolyte interface involves two processes. One process could be interpreted as the ion transfer between the Outer Helmholtz Plane (OHP) and Inner Helmholtz Plane (IHP) including the solvation/desolvation process, the other could be interpreted as that between the IHP and electrode, including ad-ion diffusion on the electrode surface. The activation energy estimated from the temperature dependence of the charge transfer resistances. The averaged activation energy value for Li^+ transfer between the IHP and electrode in propylene carbonate (PC) electrolyte is slightly larger than that in ethylene carbonate (EC)-diethyl carbonate (DEC) electrolyte, while the averaged value for Li^+ transfer between the OHP and IHP in PC is almost comparable to that in EC-DEC. However, in both charge transfer processes, the averaged value for Li^+ transfer is higher than that for Na^+ transfer. This result indicated that Li^+ on the PBA surface diffuses with higher potential barrier than Na^+. Furthermore, the effect of the interfacial charge transfer resistance was evaluated by the high charge-discharge rate experiments.

In chapter 2, the composite electrode, which contains PBA, acetylene black (AB) as conducting additive, and poly(tetrafluoroethylene) as binder, was used for analysis of interfacial charge transfer. However, there exist many interfaces in the composite electrode except PBA-electrolyte interface, such

as current collector-AB, PBA-AB and PBA-PBA interfaces. Therefore, a thin film electrode of NiFe-PBA was employed for the EIS study in chapter 3, to avoid the complexities caused by various coexisting interfaces in the composite electrode. In chapter 3, the temperature dependent EIS was carried out in both organic and aqueous electrolytes, to clarify the origin for the high power output of the aqueous batteries with PBA. The activation energy for the interfacial charge transfer with the Li^+ and Na^+ aqueous electrolytes was considerably smaller than that with the organic electrolytes. The small activation energy with the aqueous electrolytes should result from the fact that the Coulombic repulsion at the interface is largely suppressed by the screening effect of hydration. Furthermore, the hydration effect enabled the Mg^{2+} intercalation in PBA.

EIS study described in chapter 3 provided the possibility of Mg^{2+} intercalation in PBA. In chapter 4, Mg^{2+} intercalation in CuFe-PBA was investigated with aqueous electrolyte. Charge-discharge measurement and ICP-MS indicated that the CuFe-PBA can intercalate/extract Mg^{2+} reversibly. These results show that PBAs can apply as an electrode material for Mg-ion batteries.

Chapter 5 describes the precise control of magnetism of a NiFe-PBA through use of an electrochemical quantitative Li^+ titration technique, *i.e.*, the galvanostatic intermittent titration technique (GITT). When Li^+ is inserted quantitatively into NiFe-PBA, the ferromagnetic transition temperature T_C gradually decreases, and the ferromagnetic transition is completely suppressed for $Li_{0.6}$(NiFe-PBA). On the other hand, T_C increases continuously as Li^+ is extracted, and the ferromagnetic transition is nearly recovered for Li_0(NiFe-PBA). Furthermore, the plots of T_C as a function of the amount of inserted/extracted Li^+ x are well consistent with the theoretical values calculated by the molecular-field approximation. This result indicated that inserted Li^+ distributed randomly in the lattice of PBA. Furthermore, chapter 5 provided that magnetic measurement is a useful technique for the study on behavior of inserted ion in electrode material.

In addition, in chapter 6, nanostructured $LiCoO_2$ was synthesized by using an electrospinning method for high-power Li-ion battery.

Publication List

Chapter 2

"Impedance spectroscopic study on interfacial ion transfer in cyanide-bridged coordination polymer electrode with organic electrolyte"

Yoshifumi Mizuno, Masashi Okubo, Daisuke Asakura, Tatsuya Saito, Eiji Hosono, Yoshiyasu Saito, Katsuyoshi Oh-ishi, Tetsuichi Kudo, Haoshen Zhou

Electrochim. Acta, **2012**, *63*, 139-145.

Chapter 3

"Hydration Effect on Activation Energy for Electrode-Electrolyte Interfacial Charge Transfer"

Yoshifumi Mizuno, Masashi Okubo, Eiji Hosono, Tetsuichi Kudo, Haoshen Zhou, Katsuyoshi Oh-ishi

J. Phys. Chem. **2013**, *under revision*.

Chapter 4

"Magnesium Ion Intercalation in Cyanide-Coordinated Porous Polymer"

Yoshifumi Mizuno, Masashi Okubo, Tetsuichi Kudo, Haoshen Zhou, Katsuyoshi Oh-ishi

in preparation.

Chapter 5

"Precise Electrochemical Control of Ferromagnetism in a Cyanide-Bridged Bimetallic Coordination Polymer"

Yoshifumi Mizuno, Masashi Okubo, Koichi Kagesawa, Daisuke Asakura, Tetsuichi Kudo,

Haoshen Zhou, Katsuyoshi Oh-ishi, Atsushi Okazawa, Norimichi Kojima

Inorg. Chem., **2012**, *51*, 10311-10316.

Chapter 6

"Electrospinning Synthesis of Wire-Structured $LiCoO_2$ for Electrode Materials of High-Power Li-Ion Batteries"

Yoshifumi Mizuno, Eiji Hosono, Tatsuya Saito, Masashi Okubo, Daisuke Nishio-Hamane, Katsuyoshi Oh-ishi, Tetsuichi Kudo, Haoshen Zhou

J. Phys. Chem. C, **2012,** *116*, 10774-10780.

Acknowledgement

This work was carried out at Department of Applied Chemistry, Faculty of Science and Engineering, Chuo University and Energy Technology Research Institute, National Institute of Advanced Industrial Science and Technology (AIST) during 2010-2013.

I would like to express my deep gratitude to Professor Katsuyoshi Oh-ishi (Department of Applied Chemistry, Faculty of Science and Engineering, Chuo University) for his fruitful discussion and generous care to the research activities in AIST.

I would like to express my deepest gratitude to Dr. Masashi Okubo (Energy Technology Research Institute, AIST) for providing me the prime opportunity to research activities in AIST and his instruction and encouragement in this work.

I would like to thank all the members of Laboratory of Solid State Chemistry and Energy Interface Technology Group for their hearty support and encouragement. In particular, I would like to thank Dr. Haoshen Zhou, Dr. Eiji Hosono, and Dr. Daisuke Asakura, Energy Technology Research Institute, AIST for their fruitful discussion, support, and advice in this work.

Finally, I would like to thanks to my parents, family and friends for their kind considerations.

Yoshifumi Mizuno

Tokyo, Japan

2013